

ABSTRACT

BEHR, ADAM. Effectiveness of Indicators of Barrier Island Highway Vulnerability. (Under the direction of Elizabeth Sciaudone).

Because highways along barrier islands are surrounded on both sides by water, they are highly susceptible to storm impacts such as flooding, overwash, erosion, and island breaching. Simple geomorphological parameters have been used in past research to assess dune vulnerability under the assumption that it is a proxy for the coastal communities' risk of flooding and overwash. However, little work has been done to test the assumption that these geomorphological parameters provide a robust way to directly assess infrastructure vulnerability. The present research evaluates the effectiveness of 14 morphological indicators in predicting highway vulnerability to storm impacts from a data set of seven storms with documented roadway impacts. It was also hypothesized that a weighted linear function of multiple indicators could provide a better representation of vulnerability. The relationship between vulnerability thresholds and the level of risk to different storms is quantified for each of the top indicators and multi-indicator functions to enable definitions of vulnerability that are dependent on storm return periods. Results reveal that the six most skilled individual indicators of highway vulnerability to storm impacts are distance from edge-of-pavement (EOP) to dune toe, volume above mean high water between EOP and ocean shoreline, distance from the EOP to the ocean shoreline, dune crest height above the road, shore orientation relative to the dominant wave direction, and dune toe elevation. Three of these top six indicators – distance from EOP to dune toe, distance from EOP to ocean shoreline, and shore orientation – can be calculated for shorelines projected with erosion rates and used for predicting future infrastructure vulnerability. A function of dune toe elevation and distance from EOP to dune toe was the most skilled combination of indicators discovered, and it was a more skilled predictor of vulnerability than any of the tested indicators

used alone. The results convey the value of geomorphology-based indicators and their potential in larger-scale coastal infrastructure vulnerability assessments.

© Copyright 2021 by Adam Behr

All Rights Reserved

Effectiveness of Indicators of Barrier Island Highway Vulnerability

by
Adam Behr

A thesis submitted to the Graduate Faculty of
North Carolina State University
in partial fulfillment of the
requirements for the degree of
Master of Science

Civil Engineering

Raleigh, North Carolina
2021

APPROVED BY:

Elizabeth Sciaudone
Committee Chair

Casey Dietrich

Emily Berglund

BIOGRAPHY

Adam Behr was born and raised in Alabama. He attended Auburn University for his undergrad where he studied biosystems engineering. His love for classes and homework brought him to pursue graduate studies in coastal engineering. Adam's interests outside of civil and coastal engineering include playing soccer and basketball, reading comic books, and giving his two dogs and cat love.

ACKNOWLEDGMENTS

Coming in to graduate school, I underestimated the amount of thought and effort that a M.Sc. would take. I was fortunate to have an abundance of help and support along the way from my committee, professors, colleagues, and family. The coastal engineering team was full of kind and helpful people, with emphasis on a team mentality. Dr. Sciaudone was the most significant mentor I have had so far in my career. I appreciate that she was always enthusiastic to talk about ideas and work out problems, in addition to extremely valuable career advice and direction. Dr. Dietrich and Dr. Berglund have been incredibly helpful teachers and mentors, as well. Dr. Dietrich's coastal hydrodynamics was my first, and most potent, introduction to coastal engineering knowledge that I will always be thankful for. Dr. Berglund's course might make me an entrepreneur one day, and she was full of insightful comments that helped our journal paper immensely. Finally, thank you to Hannah for being so eager to distract me from the tedium of the many months working from home, for listening to my rambling monologues about coastal engineering stuff, for occasional Bentley Microstation expertise, and, most importantly, for always being supportive.

TABLE OF CONTENTS

| | |
|---|-----------|
| LIST OF TABLES | v |
| LIST OF FIGURES | vi |
| Chapter 1: INTRODUCTION | 1 |
| Chapter 2: BACKGROUND | 4 |
| 2.1 Coastal Vulnerability Studies | 4 |
| 2.2 Coastal Vulnerability Indicators..... | 5 |
| 2.3 Assessments of Risk to Different Storms..... | 7 |
| 2.4 Binary Classification | 9 |
| 2.5 Optimization and Solvers | 12 |
| 2.6 Study Area..... | 13 |
| 2.7 Data | 17 |
| Chapter 3: METHODOLOGY | 20 |
| 3.1 Metrics Used to Evaluate Indicators and Multi-indicator Functions | 20 |
| 3.2 Computation of Indicators..... | 21 |
| 3.3 Documented Storm Impacts | 29 |
| 3.4 Return Period Analysis..... | 30 |
| 3.5 Devised Multi-indicator Functions..... | 31 |
| 3.6 Quantified Relationship Between Vulnerability Thresholds and Storm Risk.... | 34 |
| 3.7 Current and Future Highway Vulnerability Assessments | 36 |
| Chapter 4: RESULTS AND DISCUSSION | 38 |
| 4.1 Distribution of Impacts..... | 38 |
| 4.2 Individual Indicators..... | 40 |
| 4.3 Multi-indicator Functions..... | 43 |
| 4.4 Return Period Analysis..... | 44 |
| 4.5 Vulnerability Threshold and Storm Impact Risk | 46 |
| 4.6 Present [2020] and Future [2030] Vulnerability Assessments | 49 |
| 4.7 Discussion | 54 |
| Chapter 5: CONCLUSIONS AND FUTURE WORK | 60 |
| 5.1 Conclusions | 60 |
| 5.2 Future Work | 60 |
| REFERENCES | 62 |
| APPENDICES | 68 |

LIST OF TABLES

| | | |
|-----------|---|----|
| Table 2.1 | Data sets used to evaluate storm impacts and vulnerability indicator performance..... | 19 |
| Table 3.1 | Confusion matrix of vulnerability classifications | 28 |
| Table 4.1 | Indicators ranked by skill based on PR AUC..... | 42 |
| Table 4.2 | Vulnerability functions ranked by skill..... | 44 |
| Table 4.3 | Statistically significant coefficient of determination for different p-values with n=7 storms | 47 |
| Table 4.4 | Length of road in study area vulnerable to different return period storms at present (2020) according to function of EOP to Dune Toe and Dune Toe Elevation..... | 51 |
| Table 4.5 | Length of road in study area vulnerable to different return period storms in 10 years (2030) according to function of EOP to Dune Toe and Shore Orientation | 51 |

LIST OF FIGURES

| | | |
|------------|---|----|
| Figure 2.1 | Comparison of precision-recall curves for two different binary classification models. Area under precision-recall curve (PR AUC) is greater for model designated by the solid line than that of model designated by the dashed line, which would mean the model is more skilled at making predictions. Called-out points show some of the thresholds that were used to compute the precision and recall pairs at those points | 12 |
| Figure 2.2 | Map showing (a) location along the southeastern coast of the U.S., (b) locations of water level (NOAA 8651370) and wave (Wave Information Study 63224) data employed in this research, and (c) extent of study area along Pea Island, NC. Note that at the scale of this figure the Oregon Inlet Waverider Buoy (NDBC 44095) is approximately co-located with the WIS station shown. | 16 |
| Figure 3.1 | Example of dune crest and dune toe extraction from cross-shore profile with a semi-automated algorithm..... | 23 |
| Figure 3.2 | Schematic of main parameters tested as indicators of highway vulnerability: Island Width (IW), Dune Crest Height Above Road (DCHAR), EOP to Ocean Shore (EOPOS), EOP to Estuary Shore (EOPES), EOP to Dune Toe (EOPDT), Volume Per Length (VPL), Dune Toe Elevation (DTE), Beach Slope (BS), Beach Width (BW), and Shore Orientation (SO). Some indicators, such as Smoothed Dune Crest Height Above the Road and Inverse Beach Slope, are not shown because they are difficult to illustrate and/or there is already an indicator shown on the figure that is very similar. | 27 |
| Figure 3.3 | Wave rose that shows the frequency of storm wave heights in terms of direction and magnitude | 28 |
| Figure 3.4 | Storm impacts to the highway after Hurricane Irene in August, 2011: (a) overwash sand covered road, (b) ocean-side erosion damaged pavement, (c) island breach damaged pavement..... | 30 |
| Figure 3.5 | Mixed integer linear optimization problem setup with the linearized F1- Score (eq 3.2) as the objective function. Constraints forced binary variable values to their appropriate state. The problem setup was used to solve for different combinations of indicators to find the weighting coefficients (i.e. A, B, C) for each. The function threshold was arbitrarily set to 1000, and M was set to 10000 because that was big enough to enforce the big-M constraints without causing excessive computation time. | 34 |
| Figure 4.1 | Distribution of highway impacts along the study area..... | 39 |
| Figure 4.2 | Return period analyses shown by blue dots and black-dotted best-fit line for each parameter: (a) Significant Wave Height, (b) Surge, and (c) Total Water Level. The return periods of the seven storms in the data set are shown by red triangles | 46 |
| Figure 4.3 | Linear relationship between optimal thresholds and storm return periods for each of the top six individual indicators. Storm return period along the x-axis is the average return period of storm surge, significant wave height, and storm duration. The optimal threshold, which can be thought of as the point at which the road becomes vulnerable based on a given indicator, is the threshold where F1-Score was maximized | 48 |

| | | |
|------------|---|----|
| Figure 4.4 | Linear relationship between optimal thresholds and storm return periods for each of the top six multi-indicator functions. Storm return period along the x-axis is the average return period of storm surge, significant wave height, and storm duration. The optimal threshold, which can be thought of as the point at which the road becomes vulnerable based on a given indicator, is the threshold where F1-Score was maximized..... | 49 |
| Figure 4.5 | Map of parts of NC 12 that were predicted vulnerable to storm impacts. Assessment was performed on the present (August 2020) state of the road and topography using a weighted linear function of EOP to Dune Toe and Dune Toe Elevation. View 1 of 6. Views 2-6 showing the remainder of the study area are presented in Appendix A..... | 52 |
| Figure 4.6 | Map of parts of NC 12 that were predicted vulnerable to storm impacts. Assessment was performed on the predicted future (10-year projection / August 2030) state of the road and topography using a weighted linear function of EOP to Dune Toe and Shore Orientation. View 1 of 6. Views 2-6 showing the remainder of the study area are presented in Appendix B..... | 53 |
| Figure 4.7 | Box-and-whisker plot of each indicator's values normalized by their average, which summarizes the spread of values around each indicator's mean. The top and bottom whiskers correspond to the maxima and minima. The tops and bottoms of the boxes correspond to the upper and lower quartiles of the data. The x's are the means, which are all 1 because the data has been normalized by the mean. The line within each box represents the median..... | 58 |
| Figure 4.8 | Statewide vulnerability assessment of North Carolina's most seaward roads based on the EOP to Ocean Shore indicator..... | 59 |
| Figure A.1 | Map of parts of NC 12 that were predicted vulnerable to storm impacts. Assessment was performed on the present (August 2020) state of the road and topography using a weighted linear function of EOP to Dune Toe and Dune Toe Elevation. View 1 of 6. | 69 |
| Figure A.2 | Map of parts of NC 12 that were predicted vulnerable to storm impacts. Assessment was performed on the present (August 2020) state of the road and topography using a weighted linear function of EOP to Dune Toe and Dune Toe Elevation. View 2 of 6. | 70 |
| Figure A.3 | Map of parts of NC 12 that were predicted vulnerable to storm impacts. Assessment was performed on the present (August 2020) state of the road and topography using a weighted linear function of EOP to Dune Toe and Dune Toe Elevation. View 3 of 6. | 71 |
| Figure A.4 | Map of parts of NC 12 that were predicted vulnerable to storm impacts. Assessment was performed on the present (August 2020) state of the road and topography using a weighted linear function of EOP to Dune Toe and Dune Toe Elevation. View 4 of 6. | 72 |
| Figure A.5 | Map of parts of NC 12 that were predicted vulnerable to storm impacts. Assessment was performed on the present (August 2020) state of the road and topography using a weighted linear function of EOP to Dune Toe and Dune Toe Elevation. View 5 of 6. | 73 |
| Figure A.6 | Map of parts of NC 12 that were predicted vulnerable to storm impacts. Assessment was performed on the present (August 2020) state of the road and | |

| | | |
|-------------|---|----|
| | topography using a weighted linear function of EOP to Dune Toe and Dune Toe Elevation. View 6 of 6..... | 74 |
| Figure B.1 | Map of parts of NC 12 that were predicted vulnerable to storm impacts. Assessment was performed on the predicted future (10-year projection / August 2030) state of the road and topography using a weighted linear function of EOP to Dune Toe and Shore Orientation. View 1 of 6..... | 75 |
| Figure B.2 | Map of parts of NC 12 that were predicted vulnerable to storm impacts. Assessment was performed on the predicted future (10-year projection / August 2030) state of the road and topography using a weighted linear function of EOP to Dune Toe and Shore Orientation. View 2 of 6..... | 76 |
| Figure B.3 | Map of parts of NC 12 that were predicted vulnerable to storm impacts. Assessment was performed on the predicted future (10-year projection / August 2030) state of the road and topography using a weighted linear function of EOP to Dune Toe and Shore Orientation. View 3 of 6..... | 77 |
| Figure B.4 | Map of parts of NC 12 that were predicted vulnerable to storm impacts. Assessment was performed on the predicted future (10-year projection / August 2030) state of the road and topography using a weighted linear function of EOP to Dune Toe and Shore Orientation. View 4 of 6..... | 78 |
| Figure B.5 | Map of parts of NC 12 that were predicted vulnerable to storm impacts. Assessment was performed on the predicted future (10-year projection / August 2030) state of the road and topography using a weighted linear function of EOP to Dune Toe and Shore Orientation. View 5 of 6..... | 79 |
| Figure B.6 | Map of parts of NC 12 that were predicted vulnerable to storm impacts. Assessment was performed on the predicted future (10-year projection / August 2030) state of the road and topography using a weighted linear function of EOP to Dune Toe and Shore Orientation. View 6 of 6..... | 80 |
| Figure C.1 | Histogram of the EOP to Dune Toe indicator's values normalized by their mean to show the distribution of data | 81 |
| Figure C.2 | Histogram of the Volume Per Length indicator's values normalized by their mean to show the distribution of data | 81 |
| Figure C.3 | Histogram of the EOP to Ocean Shore indicator's values normalized by their mean to show the distribution of data | 82 |
| Figure C.4 | Histogram of the Dune Crest Height Above the Road indicator's values normalized by their mean to show the distribution of data | 82 |
| Figure C.5 | Histogram of the Shore Orientation indicator's values normalized by their mean to show the distribution of data | 83 |
| Figure C.6 | Histogram of the Dune Toe Elevation indicator's values normalized by their mean to show the distribution of data | 83 |
| Figure C.7 | Histogram of the Beach Slope indicator's values normalized by their mean to show the distribution of data | 84 |
| Figure C.8 | Histogram of the Island Width indicator's values normalized by their mean to show the distribution of data | 84 |
| Figure C.9 | Histogram of the Beach Width indicator's values normalized by their mean to show the distribution of data | 85 |
| Figure C.10 | Histogram of the Road Elevation indicator's values normalized by their mean to show the distribution of data | 85 |

Figure C.11 Histogram of the EOP to Estuary Shore indicator's values normalized by their mean to show the distribution of data..... 86

CHAPTER 1: INTRODUCTION

Coastal areas are attractive places to live and work, drawing in a large portion of the human population. Small and Nicholls (2003) estimated that 1.2 billion people live within 80.5 km of a coastline, which Neumann et al. (2015) predicted will grow. Due to their proximity to the ocean, coastal communities are susceptible to a unique combination of processes, such as tides, storm surge, and waves, which impact and damage infrastructure. The regularity and severity of impacts that occur are likely to worsen into the future due to sea level rise (SLR) (Mimura, 2013; Enríquez et al., 2019) and increasing occurrences of extreme weather events (USGCRP, 2018; EASAC, 2013). Barrier islands face these hazards, in addition to island breaching. Island breaching occurs when elevated soundside water levels and oceanside wave erosion cut new inlets through the island (Safak, Warner, and List, 2016).

Storm impacts to a barrier island's highway can be problematic in both the short and long-term. For instance, impacts can cause road closures during extreme weather events when people may need to evacuate, and parallel or weir flow can erode the base of a road, increasing the vulnerability of pavement systems (Douglass and Krolak, 2008). Engineers and stakeholders use coastal vulnerability assessments to identify the components of infrastructure that are most at risk to being impacted during storms, which helps them strategically plan projects. Assessments often include predictions about future vulnerability, as well. Methods to assess the vulnerability of infrastructure can include modeling of processes that inundate infrastructure (Li, Lin, and Burks-Copes, 2013; Kafalenos et al., 2008); empirical parameterization of different erosion regimes (Stockdon, Plant, and Sallenger, 2009); computation of vulnerability indices using a combination of geomorphology and process-based variables (Francis et al., 2019); and computation of simple, geomorphology-based indicators (Velasquez-Montoya et al., 2021).

Simple indicators of coastal highway vulnerability are valuable because they can be easily computed with updated topography, enabling researchers to monitor spatial and temporal changes in vulnerability. There is limited research on the effectiveness of geomorphology-based vulnerability indicators across a range of storms because robust datasets of pre-storm topography along with documentation of the precise locations of post-storm impacts are scarce. Without data for precise locations of storm impacts to infrastructure, past research (Claudino-Sales, Wang, and Horwitz, 2008; Beuzen et al., 2019; Figlus et al., 2011; Judge, Overton, and Fisher 2003) has largely focused on effectiveness of indicators and controls of erosion from the perspective of dune well-being, under the assumption that dunes are the primary protection for infrastructure behind them. Dune systems have been repeatedly proven to be valuable sources of protection for infrastructure on the landward side of them (van de Graaff, 1986; Carter, 1988; Stauble, Seabergh, and Hales, 1990; Rogers, 2007). However, while failure of a beach and dune system does imply that infrastructure behind the dunes are affected, there are other processes, like infiltration and frictional energy losses (Donnelly, Hanson, and Larson, 2009), that affect the level of infrastructure vulnerability. There is limited research that directly analyzes the relationship between geomorphology and infrastructure vulnerability. An analysis of the geomorphological controls of road impacts ascertained that offshore bathymetry, dune height, and island width were major factors (Houser, 2009). The analysis was only concerned with locations that were physically damaged during two hurricanes, therefore more common impacts that occur to coastal highways like overwash were excluded (Houser, 2009).

The present study's aim is to compare the effectiveness of a wide range of geomorphology-based indicators at assessing coastal highway vulnerability to multiple types of storm impacts, overwash, erosion damage to pavement, and island breaching damage to

pavement, with the frequency of storm impacts at each transect serving as a proxy for observed vulnerability. The present study uses empirically-driven optimization methods to test the hypothesis that incorporation of multiple indicators can improve the ability to assess vulnerability. The present research also aims to quantify the level of vulnerability in terms of storm return period. This research focuses on assessing vulnerability at a small spatial scale for project planning and monitoring purposes with geomorphological parameters; it is assumed that larger-scale process variables like wave climate and tidal range did not vary over the study area.

CHAPTER 2: BACKGROUND

2.1 Coastal Vulnerability Studies

Assessments of coastal infrastructure vulnerability help engineers and stakeholders manage risks and strategically plan future projects by locating the stretches of coastline most susceptible to storm impacts. The goals of coastal vulnerability studies can vary depending on the spatial scale and scope of the project. Studies that explore vulnerability at regional or larger scales (i.e. Stockdon, Plant, and Sallenger, 2009; Francis et al., 2019; Kafalenos et al., 2008) can inform coastal managers and focus attention on the most vulnerable areas of a broader region. Smaller scale studies may seek to identify the stretches of coastline most suitable for a project or assess risk at a very fine resolution (i.e. Overton and Fisher, 2000; Li, Lin, and Burks-Copes, 2013).

Coastal vulnerability studies have traditionally used modeling, mapping techniques, and geomorphology-based indicators to determine their study area's spatial variability in dune or infrastructure vulnerability to storm impacts. Li, Lin, and Burks-Copes (2013) applied hydrodynamic, wave, and sediment-transport models to predict which areas and infrastructure of a naval station would be vulnerable to 50 and 100-year storms under different SLR scenarios. During phase 1 of their study, Kafalenos et al. (2008) modeled storm surge including effects of SLR scenarios and mapped the results to predict vulnerable stretches of road between Galveston, TX and Mobile, AL, USA. The USGS National Assessment of Coastal Change Hazards program (Stockdon, Plant, and Sallenger, 2009) combines the Storm Impact Scale (Sallenger, 2000) with most recent coastal topography data, storm surge model outputs, and predicted wave runup calculated with Stockdon et al.'s (2006) parameterization. The program provides a probabilistic representation of the chances for significant dune erosion and an idea of the spatial variability

(Stockdon, Plant, and Sallenger, 2009). Gornitz et al. (1994) proposed a Coastal Vulnerability Index (CVI) of geological, morphological, and process-based variables, including landform type, coastal slope, relative sea level change, rock type, tidal range, and wave climate. In the CVI, each variable is discretized into classes from one to five depending on the relative risk that variable lends toward erosion or inundation. Adapted versions of the CVI have been applied in studies such as Francis et al. (2019), where vulnerable stretches of highway in Hawaii, USA were identified, and remediations were recommended. Koroglu et al. (2019) applied different studies' versions of the CVI to a common study area and pointed out how inconsistencies in the definition of risk classes for each variable can lead to significant differences in the resultant calculated CVI. The North Carolina Department of Transportation's (NCDOT) Coastal Monitoring Program (CMP) uses simple geomorphology-based indicators like island width, dune crest height above the road, and distance from edge-of-pavement (EOP) to ocean shore to assess the vulnerability of a barrier island highway off the coast of North Carolina, USA on a cross-shore transect basis (Velasquez-Montoya et al., 2021). The study additionally predicts future vulnerability at a decadal time scale by using a linear regression of shoreline positions, from which EOP to ocean shore can be calculated (Velasquez-Montoya et al., 2021).

2.2 Coastal Vulnerability Indicators

Simple indicators of coastal vulnerability have been assessed in past research predominantly by their ability to predict dune and/or beach impacts. Claudino-Sales, Wang, and Horwitz (2008) looked at which dunes survived or failed after two hurricanes, which affected a Florida, USA barrier island, to determine the controlling morphological parameters. They found that island width, height and width of the dune fields, vegetation type, distance from the dunes to the ocean, and dune field continuity explained the most variation in dune survival versus failure.

Beuzen et al. (2019) sought to determine the major geomorphological controls of dune and beach berm erosion using a dataset of 1700 cross-shore profiles with pre- and post-storm Lidar data. Beuzen et al. (2019) found that erosion of both beach berms and dunes increased as exposure to the incident waves increased; berm erosion was controlled by the pre-storm volume of the berm, such that berms with high pre-storm volumes led to high erosion; and dune erosion was equally linked to the width of the berm and the dune toe elevation, such that wide berms and elevated dune toes resulted in low erosion. Figlus et al. (2011) experimented with different dune configurations under wave flume conditions to determine which geometry most effectively limited overwash and found that a berm with dune configuration had less dune volume loss, compared to wide dune and sloping beach and dune configurations. Judge, Overton, and Fisher (2003) developed a quantitative criterion to classify failed dunes based on a 50% reduction in dune volume from pre to post-storm profiles. They then tested empirical models of expected dune erosion by Hallermeier and Rhodes (1988) (Median Erosion) and Kriebel et al. (1996) (Erosion Potential) as indicators of dune vulnerability by comparing predicted erosion to pre-storm profile dune volume. They also assessed the Storm Impact Scale (Sallenger, 2000), which takes into account total water level conditions, including mean water level, setup, runup, and dune geometry to predict the degree of morphological changes, and described two new dune vulnerability indicators, dune cross-sectional centroid and mass moment of inertia. They found the mass moment of inertia compared to water level with setup had the most success at predicting dune failure versus survival (Judge, Overton, and Fisher, 2003). Houser (2009) analyzed the spatial variations in road damage after two hurricanes, Ivan and Dennis, to determine which geomorphological variables had an influence. Relative width of the island, elevation, offshore slope, and distance from the road to the shore were considered, and results

indicated that island elevation was the primary factor related to road damage, whereas distance from the road to ocean had little to no association with damage in their analysis.

2.3 Assessments of Risk to Different Storms

Ideally, vulnerability assessments are able to give an indication of how often a storm that is predicted to impact the vulnerable areas will occur. Vulnerability analyses that map modeled water levels or extent of sediment deposition with infrastructure (i.e. Li, Lin, and Burks-Copes, 2013; Kafalenos et al., 2008) explicitly connect predicted vulnerability to storm return period via storm inputs that force the models. For example, Li, Lin, and Burks-Copes (2013) forced their hydrodynamic and sediment transport models with parameters that are characteristic of 10-, 50-, and 100-year storms to determine the vulnerability to each. The present research's focus, however, was on simple, geomorphologic indicators that can be rapidly computed, and these do not always have such a direct association with storm return period. For an indicator to be used to classify or predict vulnerability, an indicator requires a threshold to be selected that represents the cutoff between vulnerable and not vulnerable transects. Generally, multiple assumptions need to be made to manifest some association between the threshold for an indicator and the return period of storm to which it indicates vulnerability. Past research has shown that the relationship between their vulnerability threshold value and storm return period is discernible for some geomorphological indicators like dune volume per length, dune crest height, distance from EOP to ocean shore and dune toe elevation. Methods from past research to make these connections between vulnerability indicators and storm return period include use of process based numerical model simulations (Overton and Fisher, 2005; Overton and Fisher, 2007) and use of simpler parametric and process based equations (Judge, Overton, and Fisher, 2003; Plomaritis, Ferreira, and Costas, 2018).

Judge, Overton, and Fisher (2003) showed how the Storm Impact Scale (Sallenger, 2000) could be used to predict dune vulnerability depending on the total water level relative to dune crest and dune toe elevations. Total water level is a storm parameter that can be identified for a given return period storm in a locale; thus, reasonable dune crest and dune toe elevation thresholds for vulnerability for a given return period of total water level could be derived. The researchers also showed how two erosion potential indices - Hallermeier and Rhodes (1988) Median Erosion that is parameterized by the open coast flood elevation only and Kriebel et al. (1996) Erosion Potential that is parameterized by storm surge, wave height, and storm duration – can be used as dune vulnerability indicators. Reasonable dune volume (cross sectional area) thresholds could be derived from these erosion estimates calculated for any desired return period. Overton and Fisher (2005) used a (process-based morphodynamics model (SBeach) of representative transects from their study area in the NC Outer Banks forced with historical tropical storm hydrographs to predict erosion. Dune erosion was estimated for a suite of storms that affected the study area over 86 years (Scheffner et al., 1999), which allowed the researchers to calculate return periods of dune volume loss. With inclusion of the assumption from Judge, Overton, and Fisher (2003) about 50% dune volume loss equating to dune failure, conclusions could be drawn about dune volume thresholds for vulnerability relative to various return period storms. Later, Overton and Fisher (2007) assumed geometry of dunes based on USACE design standards and applied SBeach modeling along with an Empirical Simulation Technique (Scheffner et al., 1999) to determine the dune height necessary to limit the risk of dune failure in 4 years to less than 50%. The purpose of the Overton and Fisher (2007) study was to compare options for improvements to the NC 12 corridor, but the lessons learned about dune height as a vulnerability criteria were applied to the NCDOT CMP's assessments (Velasquez-Montoya et

al., 2021). Plomaritis, Ferreira, and Costas (2018) applied equations that model the depth and velocity of dune overwash given the water level including surge, dune crest elevation, and runup elevation to perform a regional assessment of overwash hazard. They used the equations to calculate the horizontal extent of overwash along their barrier island study area for a 50-year return period storm's water levels. Following the rationale of Plomaritis, Ferreira, and Costas (2018), with assumptions about the tidal phase and representative dune geometry, reasonable EOP to ocean shore thresholds for vulnerability to different return period storms could be determined.

2.4 Binary Classification

Binary classification involves predicting the classes of items with two possible outcomes or types. Binary classification metrics are calculated using a confusion matrix of the different outcomes and the proportions of correct and incorrect predictions. Correct positive class predictions are “true positives”, and incorrect positive class predictions are “false positives”. Similarly, correct negative class predictions are “true negatives”, and incorrect negative class predictions are “false negatives”. “Positive” refers to the thing of concern that is being classified, or predicted. For example, if a binary classification model's goal is to filter out spam emails from users' inboxes, emails predicted by the model to be spam would be in the positive class. The “negative” class in this example would consist of emails not predicted to be spam.

Many binary classification model metrics can be calculated using different combinations of the total numbers of these true positives, true negatives, false positives, and false negatives. Accuracy (eq. 2.1) is a well-known metric that represents the percentage of true predictions out of everything. Accuracy is a suitable metric for balanced class problems, where the two classes occur at approximately the same frequency. However, if the problem is imbalanced, such that

one class occurs much more frequently than the other, accuracy can be skewed by a model that is biased towards the dominant class (Provost, Fawcett, and Kohavi, 1998). This issue is intensified if the dominant class is the negative class, but accurately predicting the positive class is vital. Other metrics used to evaluate binary classification models include precision, recall, F-score, area under the receiver-operating-characteristic curve (ROC AUC), and area under the precision-recall curve. Precision (eq. 2.2) calculates the percentage of the positive class that were correctly predicted out of all items predicted to be in the positive class, i.e. the percentage of transects modeled as vulnerable that were observed to be vulnerable out of all transects classified as vulnerable. Recall (eq. 2.3) computes the percentage of true positives out of all of the items in the positive class, i.e. the percentage of transects classified as vulnerable that were observed to be vulnerable out of all transects that were observed to be vulnerable. Precision and recall are opposed measurements, with the maximum of one being the minimum of the other. If precision and recall are given an equal weight, the harmonic mean of a model's precision and recall is called the F1-Score (eq. 2.4). The F1-Score, therefore, takes into account both metrics. Because the F1-Score is a harmonic mean, or the inverse of the mean of the reciprocals, it rapidly diminishes when either one of the metrics composing it is small.

Accuracy, precision, recall, and F1-Score all are threshold-sensitive because they change depending on the threshold that is used in the classification model. Being threshold-sensitive is a drawback when the goal in assessing a binary classification model is to give an overall determination of skill. The area under precision-recall curve (PR AUC) and area under receiver-operating-characteristics curve (ROC AUC) are metrics that are both independent of threshold value and appropriate for imbalanced class problems (Davis and Goadrich, 2006). The ROC curve illustrates the inverse relationship between the rates of correctly predicting the positive

class and incorrectly predicting the negative class, and the PR curve illustrates the tradeoff between precision and recall at different thresholds (Davis and Goadrich, 2006). Example PR curves are shown in Figure 2.1 for two different models, one with a high PR AUC, indicating the model is highly skilled at predicting the positive class, and one with a low PR AUC. The PR curve is constructed from precision and recall values that are calculated iteratively for different threshold values. Figure 2.1 points out a subset of the thresholds that were used to calculate some of the precision-recall pairs for both of the example models. Davis and Goadrich (2006) argued that, for imbalanced class problems, the PR AUC can be a more appropriate and robust metric than AOC AUC.

Binary classification model metrics are relative measurements, and there are no defined bounds for “good” or “bad” models. However, the metrics do allow for comparison among models or binary indicators applied to a mutual problem.

$$Accuracy = \frac{TP+TN}{TP+TN+FP+FN} \quad (2.1)$$

$$Precision = \frac{TP}{TP+FP} \quad (2.2)$$

$$Recall = \frac{TP}{TP+FN} \quad (2.3)$$

$$F - 1 \text{ Score} = \frac{2*Precision*Recall}{Precision+Recall} \quad (2.4)$$

Where

TP = Number of true positives, TN = Number of true negatives, FP = Number of false positives, and FN = Number of false negatives.

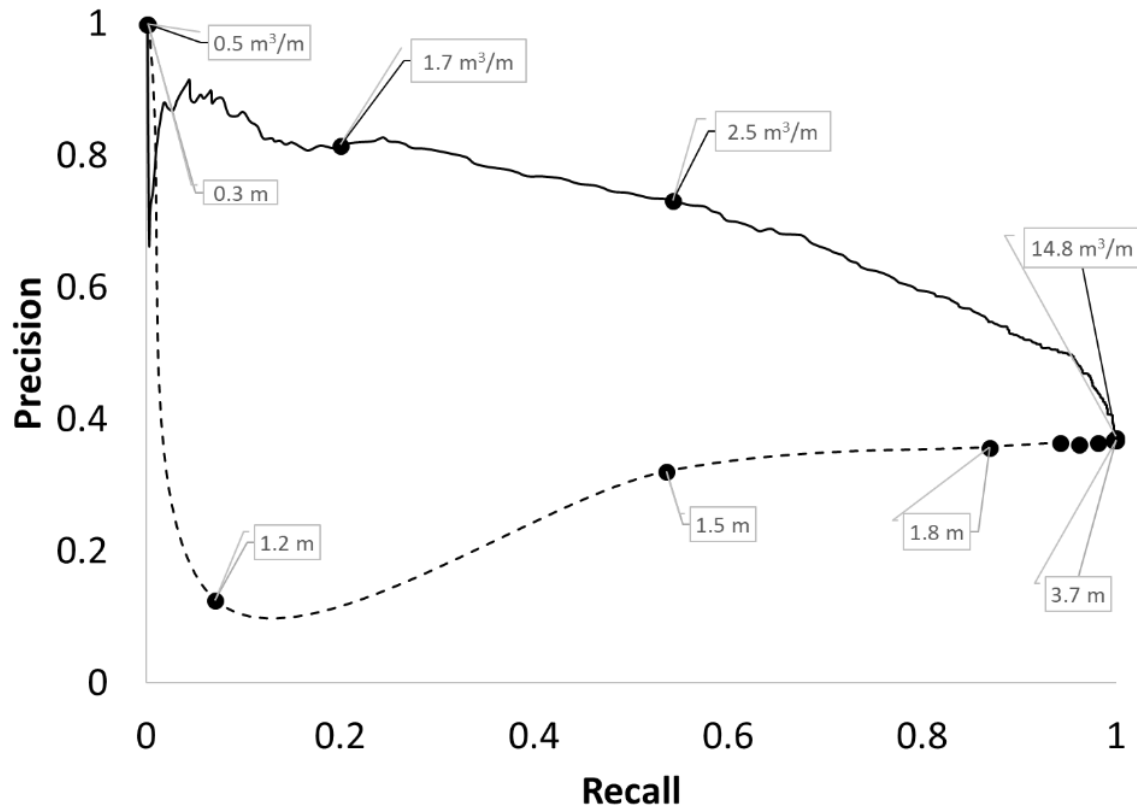


Figure 2.1 Comparison of precision-recall curves for two different binary classification model example. Area under precision-recall curve (PR AUC) is greater for model designated by the solid line than that of model designated by the dashed line, which would mean the model is more skilled at making predictions. PR AUC is an integrated measure of the skill at all possible threshold values. To illustrate this, the called-out points show some of the thresholds that were used to compute the precision and recall pairs at those points.

2.5 Optimization and Solvers

Optimization problems composed of nonlinear models featuring a mixture of different variable types are known as Mixed-Integer Nonlinear Programs (MINLP). These types of problems arise in many real world applications that involve combinations of binary decisions, discrete variables, and continuous variables, along with linear and nonlinear constraints (Belotti et al., 2013). Real world examples of MINLP's include minimization of fuel consumption for a subway system by representing routes with decision variables and speed as a continuous variable (Belotti et al., 2013) and maximization of power generation on a wind farm by representing the

layout of turbines as a grid of decision variables (Kuo et al., 2016). MINLP's can be deterministically solved with techniques like branch-and-bound, heuristics, and cutting planes (Belotti et al., 2013).

MATLAB does not offer a deterministic solver for MINLP's, but it does have a Mixed Integer Linear Programs (MILP's) solver (Mathworks, n.d.). MINLP's can be adapted to suit the MILP solver if nonlinear functions and constraints can be linearized, or, alternatively, MATLAB's Genetic Algorithm (GA) can be used. Holland (1992) explained that genetic algorithms mimic evolution to converge on a global maximum or minimum by taking a population of potential solutions and simulating natural selection and reproduction on the population. An objective, or "fitness function", distinguishes the best and worst solutions for each generation, and the GA imitates natural selection by eliminating the worst solutions, or "chromosomes". The best chromosomes then pair up randomly and parts of each exchange to create new chromosomal "offspring". Parents and offspring, along with some intermediate solutions, are passed to the next generation. The GA ensures the entire solution space is searched by imparting random changes, or "mutations", to a portion of some chromosomes' variables. The process iterates until the fitness function reaches an asymptote.

2.6 Study Area

Barrier islands off the coast of North Carolina are crucial ecosystems, popular tourist destinations, and desirable places to live. The NC Division of Coastal Management (NCDCM) found that Dare County accounts for \$957 million USD per year of the state's travel expenditures, which is approximately 5% of North Carolina's total travel income (NCDCM, 2016). The region attracts a significant amount of research attention due to its dynamic

geography and plethora of biodiversity (Sciaudone et al., 2016; Velasquez Montoya and Overton, 2017; Pfaller et al., 2020; Levine et al., 2017; Halls and Randall 2018, and others).

Hatteras Island—the northern tip locally known as Pea Island—is a barrier island in Dare County that is host to the communities of Rodanthe, Waves, and Salvo, as well as the 5,834 acre Pea Island National Wildlife Refuge (USFWS, 2020). Oregon Inlet to the north separates the island from the northern Outer Banks and the Pamlico Sound lies between the mainland and the island (Figure 2.2). NC 12 is the sole highway that connects Hatteras Island and its communities with the northern Outer Banks and serves as the only evacuation route. This makes reliability of the highway between Oregon Inlet and Rodanthe of critical importance. One of the most common impacts to NC 12 that causes closures is sand and ocean overwash, due to a combination of elevated water levels and runup of waves that can overtop dunes. The Final Environmental Impact Statement for the replacement of the bridge over Oregon Inlet noted the high frequency of highway maintenance activities required along Pea Island to move sand off the road (NCDOT, 2008). Another common impact to the road is flooding, which occurs from the bay (sound) side when winds drive up sound water levels. Flooding can make the road hazardous to traverse, sometimes requiring NCDOT to temporarily close the road. Island breaching is the impact which occurs most rarely but that is most severe. Most recently, breaches occurred in two locations on Hatteras Island during hurricane Irene in 2011 (Velasquez-Montoya et al., 2018). At each location where breaching occurred, the road was damaged. More frequent road impacts are anticipated along the study area because of globally increasing storm events (USGCRP, 2018) and predicted SLR between 10.9 and 18.5 cm by 2045 at the nearby Oregon Inlet (NC Coastal Resources Commission Science Panel, 2015).

Since 2010, NCDOT has sponsored a Coastal Monitoring Program in place to assess and predict the vulnerability of the 21.1 km stretch of highway to short- and longer-term hazards (Velasquez-Montoya et al., 2021). A significant part of the CMP involves long-term data collection in the form of bimonthly aerial photogrammetry and quarterly digital elevation models (DEMs). Because of this program, there is an extensive set of imagery and topographic data in this study area, which provides an opportunity to assess the performance of morphological indicators at predicting infrastructure vulnerability. In the present study, the focus is on impacts to highway NC 12, but the methods are applicable to coastal infrastructure in other areas as well.

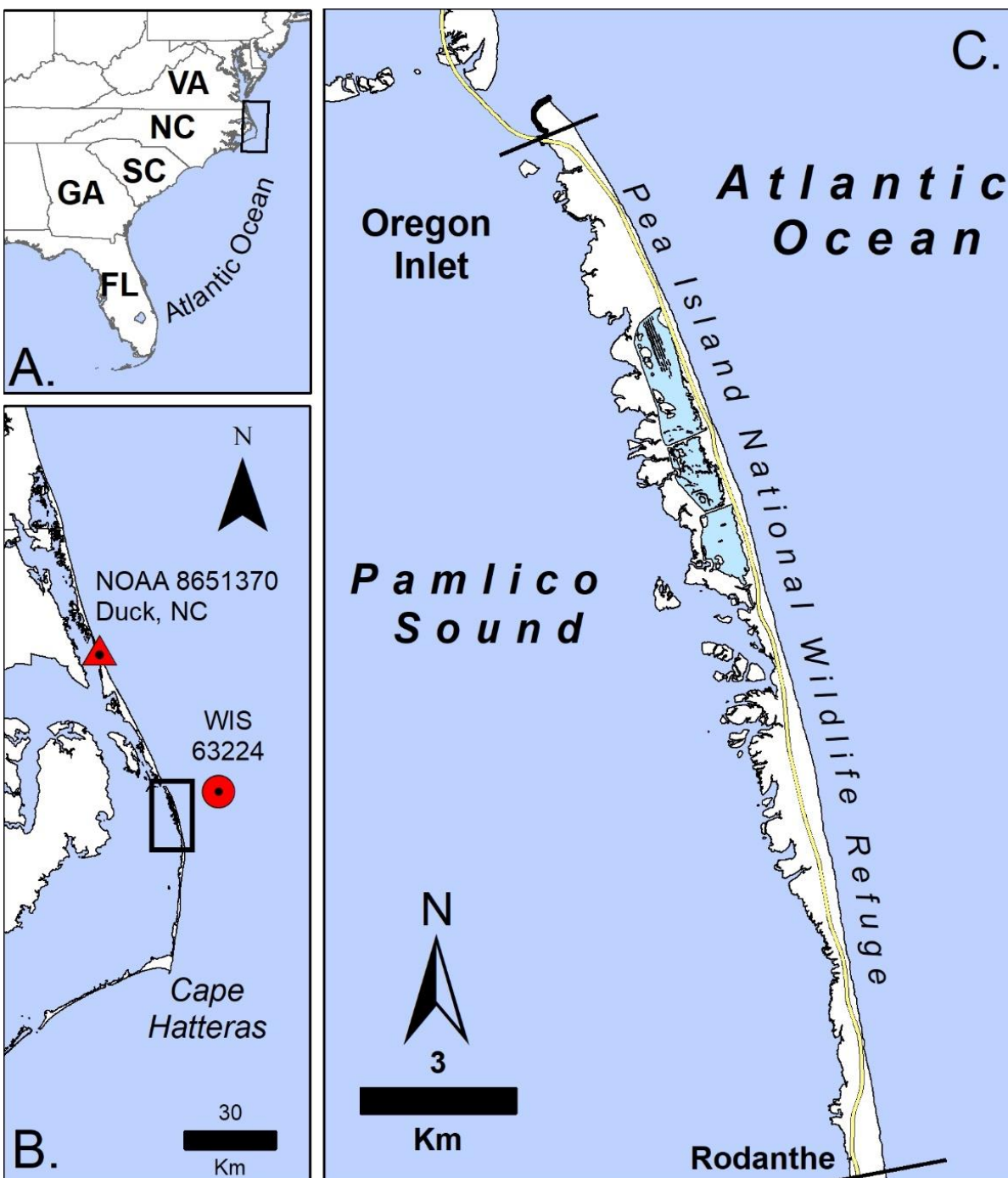


Figure 2.2 Map showing (a) location along the southeastern coast of the U.S., (b) locations of water level (NOAA 8651370) and wave (Wave Information Study 63224) data employed in this research, and (c) extent of study area along Pea Island, NC. Note that at the scale of this figure the Oregon Inlet Waverider Buoy (NDBC 44095) is approximately co-located with the WIS station shown.

2.7 Data

Raster data of 76.2 cm resolution digital elevation models and 15.2 cm resolution aerial imagery were sourced from NCDOT's Coastal Monitoring Program (Velasquez-Montoya et al., 2021). These DEMs were selected based on the time their data was collected relative to storms that affected the study area. The DEMs cover the entire Coastal Monitoring Program's study area, from the old Coast Guard lighthouse on Bodie Island, north of Oregon Inlet, southward to the town of Rodanthe (Figure 2.2). A subset of previously established transects developed for the Coastal Monitoring Program was used in this study. These transects are spaced at 45.7 m and are approximately shore-perpendicular. Figure 2.2 shows the northern and southernmost transects comprising the study area. Post-storm aerial images with 30.5 cm resolution were sourced from the National Oceanic and Atmospheric Administration's (NOAA) Emergency Response Imagery Index (NOAA, 2020).

The coordinate system of the data from NCDOT is NAD 1983 State Plane North Carolina FIPS 3200, and the coordinate system of the NOAA data is WGS84. NAD 1983 State Plane North Carolina was used for the project because the coordinate system is a projected system that encompasses the study area and represents lengths, areas, and shape in the area well. Thus, the NOAA imagery was projected to the NAD 1983 State Plane North Carolina coordinate system to make it compatible with the other data. Table 2.1 details the data sets employed in the present study.

The Duck, NC Field Research Facility and U.S. Army Corps of Engineers Wave Information Studies station 63224 were the closest sources of long-term ocean-side water level and wave data, respectively. Wave and water level data from 1980 to 2018 were collected from Wave Information Studies (WIS) station 63224 and the NOAA water level gauge at Duck, NC

(Station 8651370). The WIS data is a hindcast product produced by the Coastal and Hydraulics Laboratory Engineer Research and Development Center (Tracy and Cialone, 2006).

Additional significant wave height and dominant wave period data were sourced from the NOAA National Data Buoy Center's station 44095 near Oregon Inlet for the year 2019. This station provided an observational time series of wave conditions near the study area going back to 2012 (NOAA, 2018).

Table 2.1 Data sets used to evaluate storm impacts and vulnerability indicator performance.

| Storm | Data Set | Dates | Data Source | Notes |
|------------------------------------|-----------------|------------------|--------------------|--------------|
| Hurricane Irene, 27 August 2011 | DEM | 2 August 2011 | NC DOT | Pre-Storm |
| Hurricane Irene, 27 August 2011 | Aerial Imagery | 2 August 2011 | NC DOT | Pre-Storm |
| Hurricane Irene, 27 August 2011 | Aerial Imagery | 28 August 2011 | NC DOT | Post-Storm |
| Hurricane Sandy, 26 October 2012 | DEM | 11 October 2012 | NC DOT | Pre-Storm |
| Hurricane Sandy, 26 October 2012 | Aerial Imagery | 11 October 2012 | NC DOT | Pre-Storm |
| Hurricane Sandy, 26 October 2012 | Aerial Imagery | 31 October 2012 | NC DOT | Post-Storm |
| Hurricane Arthur, 4 July 2014 | DEM | 12 April 2014 | NC DOT | Pre-Storm |
| Hurricane Arthur, 4 July 2014 | Aerial Imagery | 2 June 2014 | NC DOT | Pre-Storm |
| Hurricane Arthur, 4 July 2014 | Aerial Imagery | 4 July 2014 | NOAA | Post-Storm |
| Nor'easter, 7 February 2016 | DEM | 7 October 2015 | NC DOT | Pre-Storm |
| Nor'easter, 7 February 2016 | Aerial Imagery | 8 December 2015 | NC DOT | Pre-Storm |
| Nor'easter, 7 February 2016 | Aerial Imagery | 8 February 2016 | NC DOT | Post-Storm |
| Hurricane Matthew, 5 October 2016 | DEM | 22 August 2016 | NC DOT | Pre-Storm |
| Hurricane Matthew, 5 October 2016 | Aerial Imagery | 22 August 2016 | NC DOT | Pre-Storm |
| Hurricane Matthew, 5 October 2016 | Aerial Imagery | 10 October 2016 | NOAA | Post-Storm |
| Nor'easter, 2 March 2018 | DEM | 9 February 2018 | NC DOT | Pre-Storm |
| Nor'easter, 2 March 2018 | Aerial Imagery | 9 February 2018 | NC DOT | Pre-Storm |
| Nor'easter, 2 March 2018 | Aerial Imagery | 26 March 2018 | NOAA | Post-Storm |
| Hurricane Dorian, 5 September 2019 | DEM | 29 August 2019 | NC DOT | Pre-Storm |
| Hurricane Dorian, 5 September 2019 | Aerial Imagery | 29 August 2019 | NC DOT | Pre-Storm |
| Hurricane Dorian, 5 September 2019 | Aerial Imagery | 7 September 2019 | NOAA | Post-Storm |

CHAPTER 3: METHODOLOGY

Binary classification metrics were used to assess and compare indicators. Binary classification metrics require the breakdown of correct and incorrect predictions, known as a “confusion matrix”, as input. Fourteen geomorphological parameters were used as indicators to make pre-storm vulnerability predictions, and observed storm impacts to the road were identified by comparing pre and post-storm aerial imagery. These two sets of data allowed for predictions made by each indicator to be categorized based on whether or not they correctly predicted vulnerability. To develop functions of multiple indicators, optimization problems were set up using the same data that were used for the indicator evaluations. Qualities of a couple of solvers were explored, and one was selected that best fit the needs of this research. Finally, the dataset was disaggregated into each individual storm to derive relationships between thresholds for individual indicators and multi-indicator functions and storm severity, and these threshold trends were put into practice along with multi-indicators functions results to map present and future vulnerability of the study area.

3.1 Metrics Used to Evaluate Indicators and Multi-indicator Functions

Predicting highway vulnerability is a binary classification problem: transects are classified as vulnerable, or not. In the present binary classification model, the indicators are used to separate transects along the highway into vulnerable and not-vulnerable classes, depending on the indicator values relative to a specified threshold. It was assumed that indicators are inversely related to vulnerability, such that transects are predicted to be vulnerable if their indicator value is less than their specified threshold.

Binary classification model metrics were used to measure each indicator’s performance, allowing for comparison between the indicators. In this case of highway vulnerability

assessment, if a certain transect was predicted to be vulnerable, that prediction would be a “true positive” if the transect was observed to be vulnerable during a storm, and a “false positive” if the transect was not observed to be vulnerable. The converse is true for transects predicted to not be vulnerable. Transects predicted to be not vulnerable that were not impacted are “true negatives”, and transects predicted to be not vulnerable that were impacted are “false negatives”. The confusion matrix, Table 3.1, summarizes these categories.

For this study, F-1 Score and PR AUC metrics were used to compare the effectiveness of vulnerability indicators because predicting highway vulnerability is an imbalanced class problem, where the more important class (impacted road transect) occurs infrequently. F-1 Score and PR AUC are both compositions of precision and recall scores. Thus, they put the most weight on correctly predicting vulnerability (TP) while also incurring a cost for incorrect classifications (FP, FN).

3.2 Computation of Indicators

Geomorphological features were extracted from DEMs and aerial imagery for the closest available date prior to each storm with documented storm impacts [seven sets]. With extracted coastal landforms, various indicator values were determined on a transect basis across the study area. Ocean and inlet shorelines along the study area were digitized according to the wet-dry line method (Dolan et al., 1980). Aerial imagery was examined at 1:1200 scale to maintain a consistent degree of precision while digitizing the shoreline. Estuarine shorelines were digitized by following the visible edge of the vegetation when possible, or the wet-dry line along sandy areas. Estuarine shorelines were digitized at 1:800 scale because the marsh edges are generally more intricate than the ocean shoreline’s wet-dry line. Dune crests (maximum elevations) were extracted from cross-shore profiles at each transect by an algorithm that selects the highest

elevation point between the road edge of pavement and shoreline, as illustrated in Figure 3.1.

Dune toes were extracted from the cross-shore profiles using an algorithm that picks the point on the profile with the greatest deviation between the terrain and a line from the dune crest to shoreline (Figure 3.1). The dune toe selection procedure was manually screened to ensure that there was a dune at each profile and, if there was a dune, to ensure that the toe was extracted correctly by the algorithm. It was assumed that in places without an identifiable dune there is still some semblance of a beach, with geometries similar to those in the same section of the study area. To account for the fact that there were some data points without a dune, and thus dune toe, and limit the number of points consequently removed from analysis, a 5-point moving average was applied to the dune toe data. Applying the moving average allowed for interpolation of some dune toe locations and elevations at transects without an identified dune. The highway's centerline elevations were interpolated at each transect from the DEM surface.

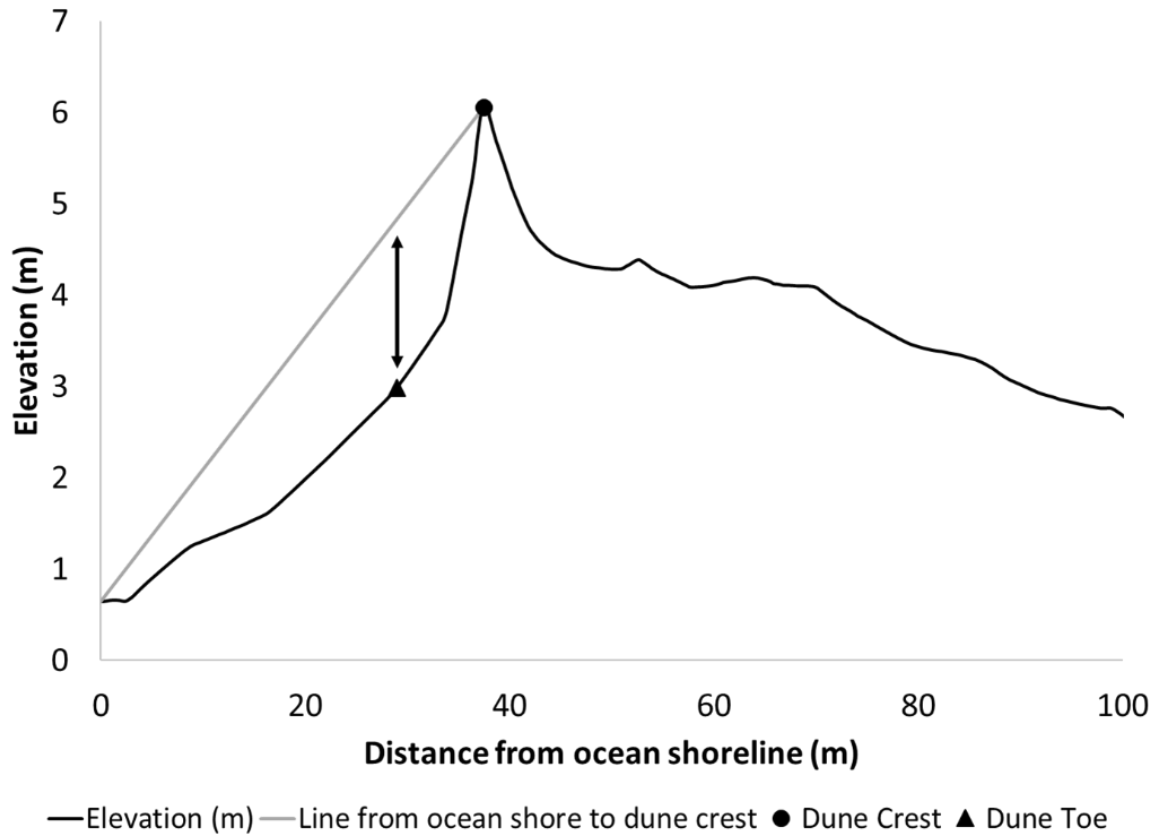


Figure 3.1 Example of dune crest and dune toe extraction from cross-shore profile with a semi-automated algorithm.

With the digitized features, the following indicators were calculated for each date prior to each storm. Figure 3.2 is a schematic of the primary geomorphological parameters tested.

1. Island width from the estuary shoreline to the ocean shoreline (Island Width).

Transects were intersected with the estuary and ocean shorelines to create sets of points. The sets of points were assigned X and Y coordinates according to the North Carolina State Plane Coordinate system. The island width at each transect was calculated as the Euclidean distance between each pair of estuary shoreline and ocean shoreline points.

2. Dune crest elevation relative to NAVD 83 (Dune Crest Elevation). Cross-shore profiles at each transect were interpolated from the DEM and the maximum elevation of each cross-shore profile between the EOP and the ocean shoreline was taken to be the dune crest elevation.
3. Road elevation relative to NAVD 83 (Road Elevation). The road's alignment was intersected with the transects to create road centerline points at each transect. The road elevation was found for each point by interpolating Z-values from the DEM surface.
4. Difference in elevation between the dune crest and the road (Dune Crest Height Above Road). Dune Crest Height Above Road was calculated by subtracting the road elevation from the dune crest elevation at each transect.
5. Three-transect moving averaged Dune Crest Height Above Road (Smoothed Dune Crest Height Above Road). A 3-point moving average operation was applied to the dune crest heights above road along the study area, such that for a given transect, the Smoothed Dune Crest Height Above Road is the average of the Dune Crest Height Above Road for that transect and the two transects adjacent to it. This allows information about the stability of dunes at nearby transects to be considered.
6. Distance from road edge-of-pavement (EOP) to ocean shoreline (EOP to Ocean Shore). The road's edge of pavement alignment was intersected with the set of transects to create EOP points at each transect, and X and Y coordinates were added to these points. EOP to Ocean Shore was calculated at each transect as the Euclidean distance between the EOP and ocean shoreline points.

7. Distance from road EOP to estuarine shoreline (EOP to Estuary Shore). EOP to Estuary Shore was calculated by subtracting the EOP to Ocean Shore from the Island Width at each transect.
8. Volume above mean high water (MHW) between EOP and ocean shoreline (Volume Per Length). Cross-shore transect profiles between the road EOP and the ocean shoreline were interpolated from the DEM surface. The MHW of the study area (1.14 ft NAVD) was subtracted from the profile, and the remaining positive cross sectional area under the curve (or volume per length in the alongshore) was calculated using the trapezoidal rule.
9. Dune toe elevation relative to NAVD (Dune Toe Elevation). Dune toe elevations were extracted from cross-shore transect profiles between the road EOP and the ocean shoreline using an algorithm (Figure 3.1) that selects the profile point of greatest deviation from a line drawn between the ocean shore and dune crest.
10. Distance from the dune toe to the ocean shoreline (Beach Width). Beach Width was calculated at each transect as the Euclidean distance between the dune toe and ocean shoreline.
11. Distance from road EOP to dune toe (EOP to Dune Toe). To calculate EOP to Dune Toe as each transect, the Beach Width (distance from dune toe to ocean shore) was subtracted from the EOP to Ocean Shore.
12. Beach slope found according to the USGS 2 point method (Doran et al., 2015) (Beach Slope). Beach Slope was calculated at each transect by subtracting the MHW elevation (1.14 ft NAVD) from the dune toe elevation and dividing by the

distance from the dune toe to the ocean shore (Beach Width). A filter was applied to the data to remove negative slopes.

13. The reciprocal of beach slope (Inverse Beach Slope). The Inverse Beach Slope ($1/\text{Beach Slope}$) was calculated to test whether beach slope was inversely related to road vulnerability.
14. The angular difference between shore-normal orientation and the weighted mean wave direction (Shore Orientation). To calculate the weighted mean wave direction, similar to the weighted mean wind direction used by Ortiz et al. (2017), the data were filtered to only include significant wave heights greater than 2 m, and wave direction was weighted by the square of significant wave height to better represent the directional distribution of wave energy. Figure 3.3 illustrates the distribution of wave directions and magnitudes during storms, as detected by the Oregon Inlet Waverider Buoy from 2012-2020 and computed using a MATLAB function (Provost, 2021). The orientation of a line normal to the shore at each transect was computed in a multistep process:
 - a. The shoreline was smoothed using the GRASS GIS function ‘v.generalize’ (Chaiken smoothing and Douglass simplification algorithms) to drastically reduce jagged edges that stem from manually digitizing the ocean shoreline.
 - b. The shoreline was converted to a raster with the GRASS function ‘v.to.rast’ using the shore’s direction relative to North as raster cell values.
 - c. To ensure the shore directions were constrained to the 1st and 4th Cartesian quadrants (because the line normal to a shore direction of 270 degrees

from North is equivalent to that of a shore direction of 90 degrees from North) cell-by-cell raster map operations were implemented with ArcMap's 'Raster Calculator'.

- d. The average shore direction of raster cells within 75 ft buffer polygons around each transect was computed with ArcMap's 'Zonal Statistics'.
- e. The average shore direction at each transect was converted to a shore normal orientation by adding or subtracting 90 degrees, depending on the quadrant of the shore orientation.

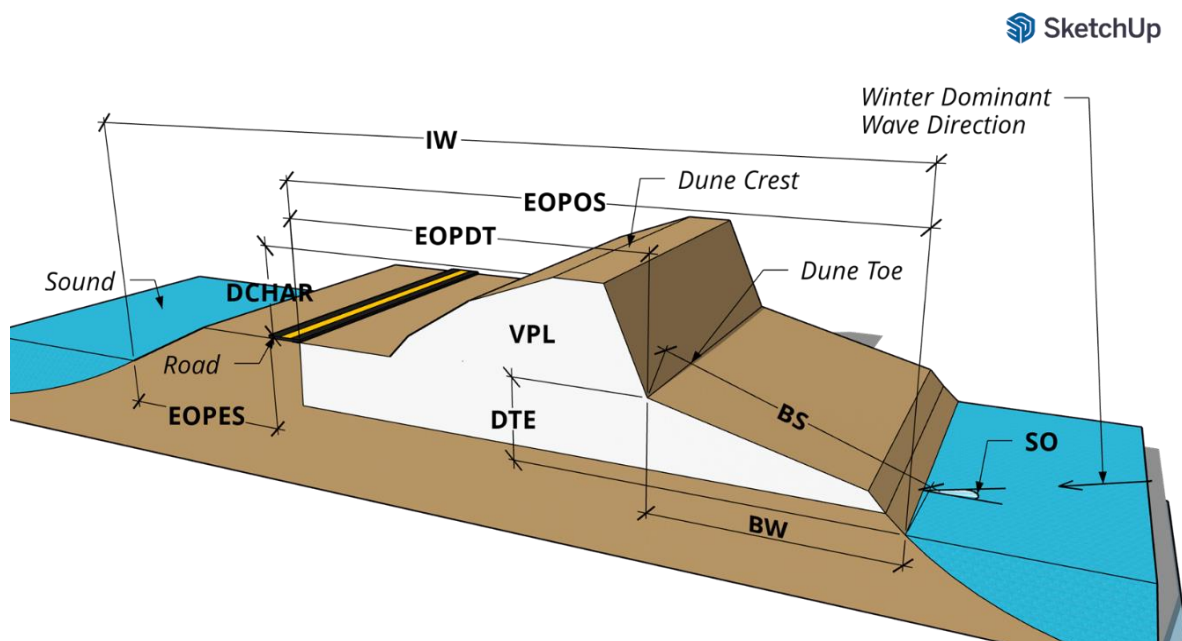


Figure 3.2 Schematic of main parameters tested as indicators of highway vulnerability: Island Width (IW), Dune Crest Height Above Road (DCHAR), EOP to Ocean Shore (EOPOS), EOP to Estuary Shore (EOPES), EOP to Dune Toe (EOPDT), Volume Per Length (VPL), Dune Toe Elevation (DTE), Beach Slope (BS), Beach Width (BW), and Shore Orientation (SO). Some indicators, such as Smoothed Dune Crest Height Above the Road and Inverse Beach Slope, are not shown because they are difficult to illustrate and/or there is already an indicator shown on the figure that is very similar.

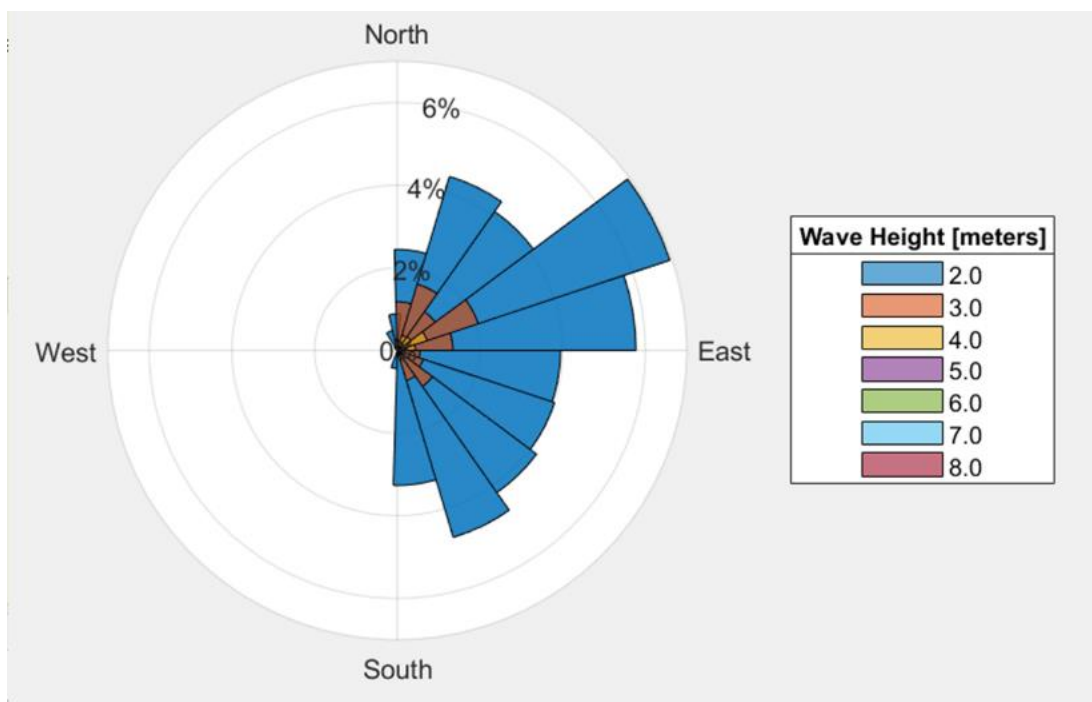


Figure 3.3 Wave rose that shows the frequency of storm wave heights in terms of direction and magnitude.

Applying each indicator, each transect was predicted to be vulnerable, or not vulnerable, to storm impacts at the date prior to each storm. These vulnerability predictions were compared with observed vulnerability to determine whether each prediction was correct or incorrect. An example of the confusion matrix including all of the possible outcomes that result from an indicator evaluation is shown in Table 3.1.

Table 3.1 Confusion matrix of vulnerability classifications

| | Predicted Vulnerable | Predicted Not Vulnerable |
|--------------------------------|-----------------------------|---------------------------------|
| Observed Vulnerable | True Positives | False Negatives |
| Observed Not Vulnerable | False Positives | True Negatives |

F1-Score (eq. 2.4) and PR AUC (Figure 2.1) were used to evaluate indicators because predicting vulnerability is an imbalanced class problem with the positive class (road impacts) occurring to 36% of transects during storms in this dataset. An optimal threshold was found

iteratively for each indicator based on the F1-Score, such that the optimal threshold for each indicator corresponds to the max F1-Score of the indicator. The optimal threshold found in this way was determined from the impacts caused by storms in this dataset. Therefore, the max F1-Score and optimal threshold could differ for an alternative set of storms of different severity.

The PR AUC was considered the most important metric of indicator skill because it is composed of the skill at all thresholds, meaning it is independent of a single threshold value. Being threshold-independent makes the PR AUC a convenient way to compare different indicators. An indicator with a greater PR AUC is better at ranking transects from most vulnerable to least vulnerable, which would make it a more valuable indicator. Additionally, a high PR AUC implies that an indicator's performance is less sensitive to the chosen threshold value. This quality is important because indicator thresholds are set based on the available data. If an indicator's performance is less sensitive to the threshold, it should be better at predicting vulnerability for storms outside of the training dataset, in a validation setting.

3.3 Documented Storm Impacts

Observed highway vulnerability was quantified using the frequency of storm impacts that occurred over the course of seven storms. Storm impacts to the road were digitized by visually comparing pre- and post-storm georeferenced aerial imagery, using ArcGIS. The three types of impacts observed are shown in Figure 3.4, including overwash, ocean-side erosion damaged pavement, and island breach damaged pavement. To avoid considering occurrences of windblown sand on the road as ocean overwash, it was required that the road be at least 50% obscured by sand coverage at a specific transect for it to be considered impacted by ocean overwash.

An example of the road being highly obscured by sand is shown in Figure 3.4(a).

Instances of damage to the pavement due to ocean-side erosion and island breaching, shown in Figure 3.4(b) and Figure 3.4(c), respectively, were also visually identified. Because shadows or water coverage could be misinterpreted as missing or damaged pavement, these types of impacts were verified with NC DOT maintenance engineers to confirm that documented damages did occur during the specific storms.

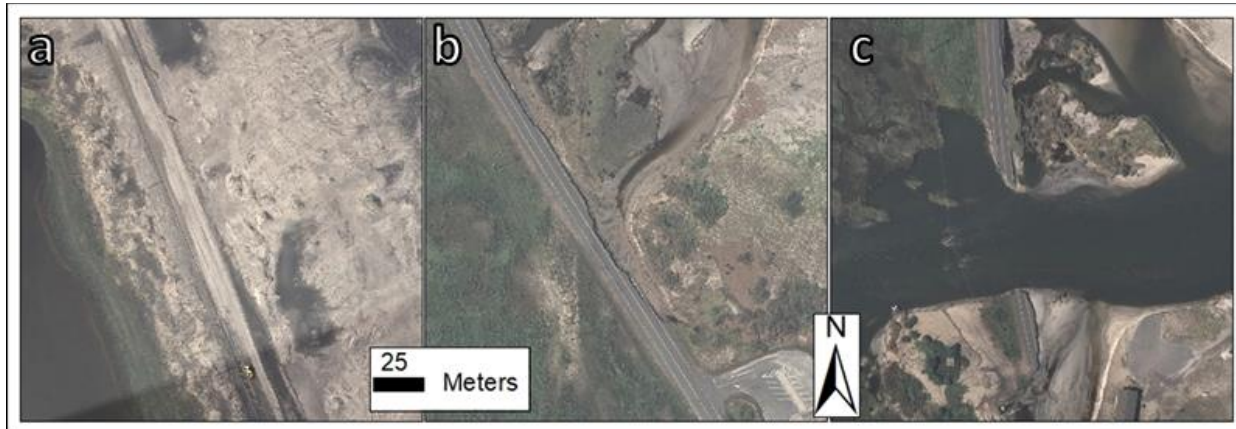


Figure 3.4 Storm impacts to the highway after Hurricane Irene in August, 2011: (a) overflow sand covered road, (b) ocean-side erosion damaged pavement, and (c) island breach damaged pavement.

3.4 Return Period Analysis

To describe the storm climate of the study area and contextualize the storms used to locate impacts and evaluate indicators, return period analyses were performed on three different wave and water level parameters. Storm events were identified from the wave height time series by using a significant wave height of > 2 m for > 8 hours criterion. Then, the maximum significant wave heights, non-tidal residuals (surge), and storm durations were collected from the water level gauge data for each of these storm events. Probability of exceedance and return period were calculated for each storm in the partial duration series using the Gumbel formula,

and a log-linear trend line was fit to the data to identify the relationship between each parameter and its respective return period, as described in the U.S. Army Corps of Engineers (USACE) Coastal Engineering Manual (USACE, 2008).

The log-linear relationships between return period and the three selected storm parameters were used to calculate the return period of each of the seven storms in this research's dataset. Hurricane Dorian occurred in 2019, which was not encompassed by WIS hindcast data (1980-2018); therefore, the maximum significant wave height for this hurricane was taken from the Oregon Inlet Waverider Buoy. The significant wave height was shoaled from 18.4 m to 15.0 m depth using linear wave theory to make the buoy data compatible with the return period analysis that was performed using WIS data (15.0 m depth).

3.5 Devised Multi-indicator Functions

It was hypothesized that a function of multiple indicators could more accurately predict vulnerability than any one indicator on its own. To incorporate indicators as continuous variables that could each provide unique information about the vulnerability at each transect, a weighted linear function (eq. 3.1) was explored. The indicator values are known geomorphological parameters that are collected at each transect, and the vulnerability function's threshold is set to an arbitrary value without physical meaning. Thus, the only unknown parameters in the vulnerability function are the weighting coefficients. The weighting coefficients are needed because the indicators can vary in units, scale, and relative importance. The weighting coefficients also may change depending on the combination of indicators featured in the function.

Optimization problems were set up for assorted combinations of indicators to relate unknown coefficients of assumed vulnerability functions (eq. 3.1) to resultant confusion matrices, with the goal of maximizing the F1-Score.

The optimization problems were solved using a Mixed Integer Linear Programming (MILP) solver because the problems included a combination of binary and continuous variables. The MILP solver requires that the objective function be linear, so F-1 Score was linearized (eq. 3.2). When given enough constraints and time, the MILP solver can converge on a deterministic solution (Mathworks, n.d.). Genetic Algorithm (GA) is an alternative solver for optimization problems featuring a mixture of continuous and binary variables. The GA solver takes an evolutionary approach to iteratively test variables and adjust parameters based on the value of the objective function at each generation. GA allows for a non-linear objective function, such as the full F1-Score (eq. 2.4) (Mathworks, n.d.). In preliminary tests of the solvers, there were not significant differences in the weights determined with the GA solver when compared with results from the MILP solver, despite the MILP solver's linearized objective function (eq. 3.2). The MILP solver was chosen because it results in a more definitive solution than the GA solver, for which the solution is not guaranteed.

Figure 3.5 shows this study's MILP statement including the constraints that force binary variables, like *vuln*, *TP*, *FP*, and *FN*, to their appropriate state. Each of these binary variables is a vector containing the value at each transect, hence the subscripts and summations in Figure 3.5. The *vuln* variable was used as a dummy variable to identify which transects were predicted vulnerable according to the value of the vulnerability function $F(A, B, C)$, whose value is dependent on the weighting variables, *A*, *B*, and *C*, and geomorphology parameters at each transect, *indicator1*, *indicator2*, and *indicator3*. The *vuln* variable was forced to its correct state

with big-M constraints (c_1 and c_2), which incur a fixed cost if some condition is met (Camm, Raturi, and Tsubakitani, 1990). The constraint requires selection of a sufficiently large parameter, M , whose magnitude considerably affects computational demand of the optimization solver; therefore, an efficient, yet effective, M , should be just large enough to enforce the conditional statement (Camm, Raturi, and Tsubakitani, 1990). An M of 10,000 was large enough to enforce this study's MILP constraints without imparting excessive computation time. The other constraints ($c_3, c_4, c_5, c_6, c_7, c_8, c_9, c_{10}, c_{11}, c_{12}$, and c_{13}) ensure that the TP , TN , FP , and FN binary variables, which track whether vulnerability predictions are true or false, are in the correct states. The *impact* parameter is a vector of 1's and 0's representing impacted transects. The *threshold* parameter is arbitrarily set to 1000. The *threshold* specifies that if a transect's function value $F(A, B, C)$ were less than 1000, the transect would be predicted as vulnerable to storm impacts. The threshold is arbitrary when solving optimization problems because the coefficients scale according to the preset threshold, such that the weights' main importance is to establish each indicator's relative contribution to vulnerability.

Optimization problems were solved for many different combinations of indicators and each of these subsequent functions were then evaluated using the binary classification model metrics mentioned previously.

$$F(\text{indicator1}, \text{indicator2}, \text{indicator3}) = A * \text{indicator1} + B * \text{indicator2} + C * \text{indicator3} \quad (3.1)$$

Where:

indicator1, *indicator2*, *indicator3* are indicator values, and A , B , C are coefficients that scale the indicator values such that they contribute to the overall vulnerability function's value.

IF $F(\text{indicator1}, \text{indicator2}, \text{indicator3}) < \text{Threshold}$, THEN transect is vulnerable.

$$\text{Linearized } F - 1 \text{ Score} = 2 * TP - FP - FN \quad (3.2)$$

Where:

TP = Number of true positives, FP = Number of false positives, and FN = Number of false negatives.

$$\begin{aligned}
 & \text{maximize} && 2 * \sum_{i=1}^n TP_i - \sum_{i=1}^n FP_i - \sum_{i=1}^n FN_i \\
 & \text{subject to} && \\
 & && c_1(A, B, C, vuln_i) = F_i(A, B, C) - \text{threshold} - M * (1 - vuln_i) \leq 0 \\
 & && c_2(A, B, C, vuln_i) = \text{threshold} - M * vuln_i - F(A, B, C) \leq 0 \\
 & && c_3(TP_i, vuln_i) = TP_i - vuln_i \leq 0 \\
 & && c_4(FP_i, vuln_i) = FP_i - vuln_i \leq 0 \\
 & && c_5(FN_i) = FN_i - \text{impact}_i \leq 0 \\
 & && c_6(TP_i) = TP_i - \text{impact}_i \leq 0 \\
 & && c_7(TP_i, vuln_i) = \text{impact}_i + vuln_i - TP_i - 1 \leq 0 \\
 & && c_8(TN_i, vuln_i) = 1 - \text{impact}_i - vuln_i - TN_i \leq 0 \\
 & && c_9(TN_i) = \text{impact}_i + TN_i - 1 \leq 0 \\
 & && c_{10}(FP_i) = \text{impact}_i + FP_i - 1 \leq 0 \\
 & && c_{11}(TN_i) = vuln_i + TN_i - 1 \leq 0 \\
 & && c_{12}(FN_i) = vuln_i + FN_i - 1 \leq 0 \\
 & && c_{13}(TP_i, FP_i, TN_i, FN_i) = TP_i + FP_i + TN_i + FN_i = 0 \\
 & \text{where} && \\
 & && A, B, C \in [0, \infty) \\
 & && TP, FP, FN, vuln \in \{0,1\} \\
 & && F_i(A, B, C) = A * \text{indicator}1_i + B * \text{indicator}2_i + C * \text{indicator}3_i \\
 & && \text{impact}_i \in \{0,1\}, \text{threshold} = 1000, M = 10000
 \end{aligned}$$

Figure 3.5 Mixed integer linear optimization problem setup with the linearized F1- Score (eq 3.2) as the objective function. Constraints forced binary variable values to their appropriate state.

The problem setup was used to solve for different combinations of indicators to find the weighting coefficients (i.e. A , B , C) for each. The function *threshold* was arbitrarily set to 1000, and M was set to 10000 because that was big enough to enforce the big-M constraints without causing excessive computation time.

3.6 Quantified Relationship Between Vulnerability Thresholds and Storm Risk

The seven storms of the dataset were aggregated in the aforementioned methods for evaluation of indicators and multi-indicator functions in Sections 3.4 and 3.5. Because the sets of 457 transects for each storm were grouped together into a single set, the optimal threshold and maximum F-1 Score of each indicator and function is an average.

Characteristics, like the maximum significant wave height, maximum surge, and duration, of the seven storms vary substantially, however, which leads to variation in the optimal thresholds. The optimal threshold of a given indicator varies depending on the storm because thresholds have a meaningful connection to physical processes driven by storms. For example, a severe storm may elevate the water level such that the road is vulnerable, or likely to be impacted, in areas with dune crests lower than that water level. The threshold affects the numbers of true positive, false positive, and false negative predictions, so to maximize the F-1 Score, the optimal threshold would be at a point to maximize the number of true positives while minimizing the number of false positives and false negatives. Continuing with this example: for a mild storm, the road may only be impacted at transects with very low dunes. The optimal threshold in this case would be lower to minimize over-prediction of vulnerability, or false positives.

To identify the correlation between storm severity and optimal threshold for each indicator and function, the seven storms were disaggregated and the optimal threshold was found for individual storms. For each indicator, the optimal thresholds were plotted against storm severity. Numerous combinations of storm characteristics, including total water level (sum of mean water level, surge, wave setup, and wave runup) (Stockdon et al., 2006), significant wave height, storm surge, storm duration, and storm power index (function of significant wave height and storm duration) (Dolan and Davis, 1992), were tested to represent storm severity. The average return period of storm surge, significant wave height, and storm duration was used to represent each storm's severity because it was found to be the most correlated with optimal thresholds.

3.7 Current and Future Highway Vulnerability Assessments

Two of the top multi-indicator functions were put into practice to illustrate the application of this study's results. The most skilled multi-indicator function, detailed following in Section 4.3, consists of EOP to Dune Toe and Dune Toe Elevation indicators. This function was used to assess the present day (2020) vulnerability of NC12 in the study area to different storm severities. Using present day geomorphology extracted from an August 2020 aerial image and DEM, EOP to Dune Toe and Dune Toe Elevation were computed on a transect basis following the methods described in Section 3.2. The function was calculated at each transect as the weighted sum of EOP to Dune Toe and Dune Toe Elevation. Weights used for the functions are described later in of Section 4.3. The function value at each transect was compared to thresholds for 1-, 5-, and 10-year return storms to predict which transects are vulnerable to each of these storms. These 1-, 5-, and 10-year vulnerability thresholds were interpolated from the linear trend discussed in Section 4.5.

Assessment of future road vulnerability requires indicators to be accurately projected over time. The goal was to predict vulnerability of NC12 along the study area in 10 years (2030), as an example. Shoreline erosion rates (ft/yr) at each transect were found using linear regression of bimonthly shoreline position data from 8/9/1992 to 8/26/2020, which is from a NCDOT CMP database (Velasquez-Montoya et al., 2021). To predict the EOP to Dune Toe at each transect in 10 years (2030), it was assumed that the Dune Toe shifts at the same rate as the shoreline. Accurately predicting Dune Toe Elevation in 10 years may be difficult because dunes are constantly evolving due to wind transport, ocean processes, and human interactions (Mitasova, Overton, and Harmon, 2005). Additionally, interactions between Dune Toe Elevation and SLR may be complex; extension of the well-established Bruun Rule's concepts (Bruun, 1962) predicts

dune toes to move vertically at the rate of SLR (Davidson-Arnott, 2005), but empirical measurements of the Dutch coast showed toes to move vertically 7-8 times faster than SLR (van Ijzendoorn et al., 2021). Predicting future Dune Toe Elevation was therefore considered beyond the scope of this study, so, instead, the function of EOP to Dune Toe and Shore Orientation was used. It is also assumed in using this function of EOP to Dune Toe and Shore Orientation to predict future vulnerability that other variables, like dune elevations, have negligible effects on vulnerability and/or are steady state. The future shoreline position was projected using linear regression following the methods described by Velasquez-Montoya et al. (2021). It was assumed that the energy-weighted average wave direction is constant over a decadal time-scale. Thus, Shore Orientation in 10 years (2030) was computed from the projected 2030 shoreline following the methods described in Section 3.2. The weighted sum of EOP to Dune Toe and Dune Toe Elevation was then calculated at each transect using the 2030 predictions of these indicators; the weights used in the function are described later in Section 4.3. Thresholds for vulnerability to 1-, 5-, and 10-year storms were interpolated from the linear trend discussed in Section 4.5, the multi-indicator function's value at each transect was compared to these thresholds, and the results were mapped.

CHAPTER 4: RESULTS AND DISCUSSION

This chapter details the results of the present study's analysis. The spatial distribution of the impacts from the entire storm data set is summarized to give the reader an idea of the degree of observed vulnerability across the study area. Single vulnerability indicators are evaluated, followed by functions of multiple indicators. Return period analysis results provide context for the storms in the data set. Statistical analysis of the relationship between storm severity and threshold for each indicator and multi-indicator function enables precise and meaningful vulnerability classifications. Finally, two top vulnerability functions are applied in conjunction with their threshold-return period relationships demonstrate present and future vulnerability assessments of the study area.

4.1 Distribution of Impacts

As shown in Figure 4.1, the number of storm impacts that occurred per transect ranged from zero (no storms caused impacts) to seven (all storms caused impacts). Impacts were most frequently observed in the northern third of the study area and in two smaller regions near the southern portion of the study area. Near the center of the study area, a temporary bridge was constructed shortly after hurricane Irene formed a breach in August of 2011 (Velasquez-Montoya et al., 2018). This temporary bridge was replaced by an interim structure (footprint indicated in Figure 4.1) which opened in November 2017. Impacts to the road in this section were lessened after bridge construction, and afterwards, the few occurrences of impacts were mainly caused by sand washing onto the bridge from the adjacent areas.

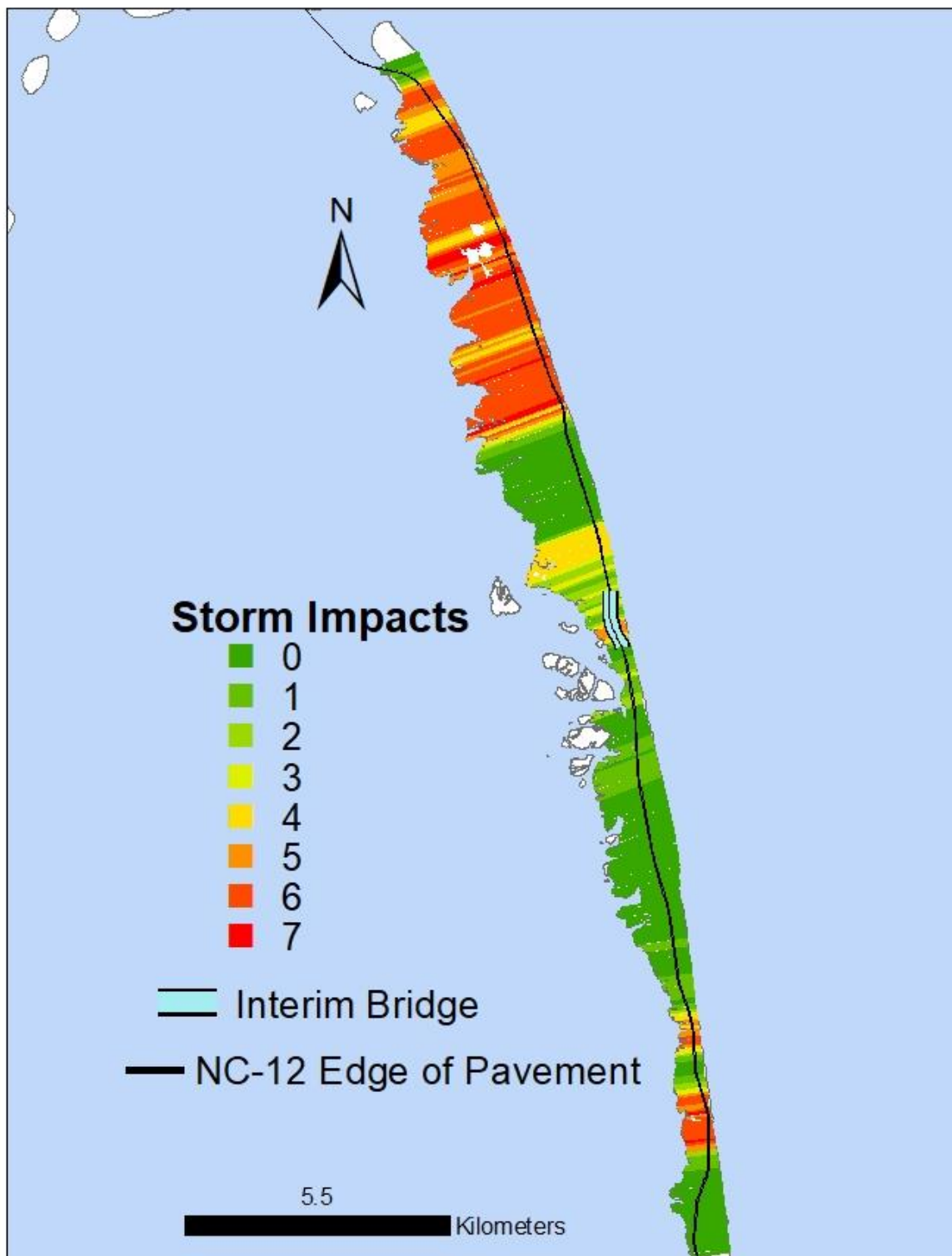


Figure 4.1 Distribution of highway impacts along the study area.

4.2 Individual Indicators

Because a completely random indicator could predict the positive class—road impacts—at the rate that they occur (approximately 36%), and because there is some uncertainty around that mean, indicators were considered unskilled if their average PR AUC was less than 0.47 (top of 95% confidence interval for a random indicator).

Table 4.1 summarizes the evaluation results with each indicator ranked in order of most to least skill based on the PR AUC metric. Several indicators were found to be good predictors of vulnerability. The most skilled indicator was the EOP to Dune Toe based on its PR AUC metric of 0.77, as well as its max F1-Score of 0.79. The threshold optimization results suggest that EOP to Dune Toe most accurately predicted vulnerability with a threshold value of 302 m. Volume Per Length was the second most skilled with a PR AUC of 0.74. The third most skilled indicator, EOP to Ocean Shore, was close behind with a PR AUC of 0.73. Despite its lower PR AUC, the F1-Score of EOP to Ocean Shore was slightly better than that of Volume Per Length. This suggests that EOP to Ocean Shore is more sensitive to the threshold value, but with its optimal threshold, it was marginally better at predicting vulnerability than the Volume Per Length.

Several different representations of the maximum elevation between the road and the ocean shoreline (dune crest) were tested. Dune Crest Height Above the Road was slightly more skilled than Dune Crest Elevation, which suggests that the road elevation has some influence on the level of vulnerability. Specifically, this result suggests to a minor extent that the elevation of the road may be inversely related to the highway's level of vulnerability. Road Elevation had a very low PR AUC of 0.27, which is only 8% greater than the bottom of the 95% confidence interval for a random indicator. Predictors found to have less skill than a random predictor are called naïve because they are more indicative of the negative class, which further suggests that

Road Elevation may be inversely related to road vulnerability. It was found that Smoothed Dune Crest Height Above the Road is a better predictor of vulnerability than Dune Crest Height Above the Road, which is likely because a 3-transect moving average allows for consideration of the state of nearby transects. The vulnerability of the road at a given transect is affected by its cross-shore beach profile, as well as the adjacent transects' profiles. Shore Orientation was the seventh best indicator, with a PR AUC only slightly less than that of Dune Crest Elevation.

Beach slope and inverse beach slope were both tested as indicators, with the presumption that the reciprocal of beach slope would be a skilled indicator and beach slope would be an unskilled, random indicator. This presumption was based on the fact that beach slope is the primary morphological parameter in wave runup and total water level formulations like that of Stockdon et al. (2006). The parameterization of runup shows that for the same given deep water wave height, the runup on a steep beach should be greater than on a flat beach. The greater the runup in an area, the greater the likelihood for dune overwash. The performance evaluations of beach slope and the reciprocal of beach slope contradicted the presumption that steeper beaches should result in greater road vulnerability. The results showed the reciprocal of beach slope to be an unskilled, random indicator of highway vulnerability and beach slope to be slightly skilled, with a PR AUC only 0.02 greater than the upper 95% confidence bound of a random indicator. Dune Toe Elevation was also found to be slightly more skilled than a random indicator.

Of the documented impacts, 97.6% were sand overwash. There were only two occurrences of breaches during the seven storms, which made it difficult to fairly assess the island width indicator. Island width was originally devised as an indicator of the island's vulnerability to breaching and, to a lesser extent, sound side flooding (Velasquez-Montoya et al., 2021), so it was not intended to be predictive of other impacts, like overwash. Because of the

types of impacts caused by the storms in the dataset, the island width indicator performed poorly and appeared to be an unskilled, random indicator. EOP to Estuary Shore was the most unskilled of all and was found to be a naïve indicator with a PR AUC significantly worse than that of a random indicator.

Table 4.1 Indicators ranked by skill based on PR AUC

| Indicator | Threshold for max F-1 score | Max F-1 score | PR AUC |
|---------------------------------------|-----------------------------|---------------|--------|
| EOP to Dune Toe | 92 m | 0.79 | 0.77 |
| Volume Per Length | 3.2 m ³ /m | 0.72 | 0.74 |
| EOP to Ocean Shore | 126.8 m | 0.73 | 0.73 |
| Smoothed Dune Crest Height Above Road | 5.8 m | 0.65 | 0.56 |
| Dune Crest Height Above Road | 5.5 m | 0.63 | 0.55 |
| Dune Crest Elevation | 6.7 m | 0.62 | 0.54 |
| Shore Orientation | 9° | 0.63 | 0.52 |
| Dune Toe Elevation | 2.4 m | 0.60 | 0.49 |
| Beach Slope | 0.09 m/m | 0.58 | 0.49 |
| Island Width | 1.47 km | 0.55 | 0.39 |
| Beach Width | 106.1 m | 0.54 | 0.37 |
| Inverse Beach Slope | 96 m/m | 0.53 | 0.30 |
| Road Elevation | 2.7 m | 0.53 | 0.27 |
| EOP to Estuary Shore | 292.9 m | 0.25 | 0.05 |

4.3 Multi-indicator Functions

The goal in exploring vulnerability functions was to determine if any weighted combinations of indicators were more skilled than the best individual indicator, EOP to Dune Toe. Weighting coefficients for each combination of indicators were determined by maximizing the F1-Score. These coefficients for the top 11 vulnerability functions are shown in Table 4.2. Shown along each row of Table 4.2 is a different combination of indicators tested as a function following the form of Eq. 5. Along each row, where blank spaces appear, the corresponding indicators were not included in that function's development. The functions that utilized unique combinations of multiple indicators resulted in the most favorable outcomes. For instance, the most skilled function, Solution #1 in Table 4.2, included an elevation variable representing the exposure of dunes to ocean processes like wave runup, Dune Toe Elevation, and a variable representing the distance ocean overwash would have to travel to reach the road, EOP to Dune Toe. The second best function included another elevation-based variable, Dune Crest Height, but the variable had a negligible effect on vulnerability predictions. The third best function featured these three aforementioned variables in addition to Shore Orientation, representing the shore's exposure to direct wave attack. EOP to Dune Toe was a variable in all of the top six functions. Dune Crest Height Above Road, Dune Toe Elevation, EOP to Dune Toe, and Shore Orientation indicators appeared in many of the top six functions, suggesting that they are important variables in prediction of road vulnerability.

Table 4.2 Vulnerability functions ranked by skill

| Solution # | Island Width | Dune Crest Ht. Above Rd. | Smoothed Dune Crest Ht. Above Rd. | EOP to Ocean Shore | Volume Per Length | Beach Width | Beach Slope | Inverse Beach Slope | Dune Toe Elevation | EOP to Dune Toe | Shore Orientation | Max F1 score | PR AUC |
|------------|--------------|--------------------------|-----------------------------------|--------------------|-------------------|-------------|-------------|---------------------|--------------------|-----------------|-------------------|--------------|--------|
| 1 | | | | | | | | | 49.8 | 2.1 | | 0.79 | 0.82 |
| 2 | | 4.3 | | | | | | | 48.9 | 2.0 | | 0.79 | 0.82 |
| 3 | | 0.7 | | | | | | | 45.6 | 2.0 | 13.0 | 0.82 | 0.79 |
| 4 | | 10.3 | | | | | | | | 2.3 | 22.8 | 0.77 | 0.78 |
| 5 | | 20.7 | | | | | | | | 2.4 | | 0.78 | 0.78 |
| 6 | | | | | | | | | | 2.7 | 23.1 | 0.77 | 0.78 |
| 7 | | 6.0 | | 1.3 | | | | | 47.3 | | | 0.75 | 0.77 |
| 8 | | 13.6 | | 1.0 | | | | | 47.3 | | 8.5 | 0.74 | 0.76 |
| 9 | | 7.5 | | 1.6 | | | 2917.0 | | | | | 0.75 | 0.76 |
| 10 | | | 32.4 | 1.1 | | | | | | | | 0.74 | 0.75 |
| 11 | | 19.7 | | 1.5 | | | | | | | | 0.75 | 0.75 |

For example, from the first row (Solution # 1) the vulnerability function would be:

$$F = 49.8 * (Dune\ Toe\ Elev.) + 2.1 * (EOP\ to\ Dune\ Toe)$$

4.4 Return Period Analysis

The majority of the storms used in this study were hurricanes because of the availability of NOAA post-storm aerial imagery of these events; however, there were also two winter storms, or “nor’easters”, that were included in the dataset. The nor’easters, which occurred in February 2016 and March 2018, were included because post-storm aerial imagery from NC DOT was available to identify impacts.

The suite of storms used to evaluate the vulnerability indicators fell within a range of return periods for surge, duration, and wave height characteristics, as shown in Figure 4.2.

Significant wave height return periods ranged from 0.9 to 21 years, storm surge return periods ranged from 0.3 and 24 years, and storm duration return periods ranged from 0.1 and 5 years.

Return period analysis is only as good as the extent of storm data supporting it. Long time series of storm data includes a greater swath of potential extreme events and improves the confidence with which probabilities of exceedance and return periods are calculated. Thus, this study used the WIS hindcasts for wave data, which cover 38 years, rather than the observational record of Oregon Inlet Waverider Buoy, which begins in 2012. Despite the longer time series of data, there are still errors introduced because 38 years is a small sample relative to the entire history of storm events in the area. When storm parameters are estimated for return periods that are small relative to the dataset's time span, the errors are minor. Errors become more substantial as the return period of an estimate approaches the extent of the time span, 38 years in this case, and grow further as extrapolations are made beyond this extent.

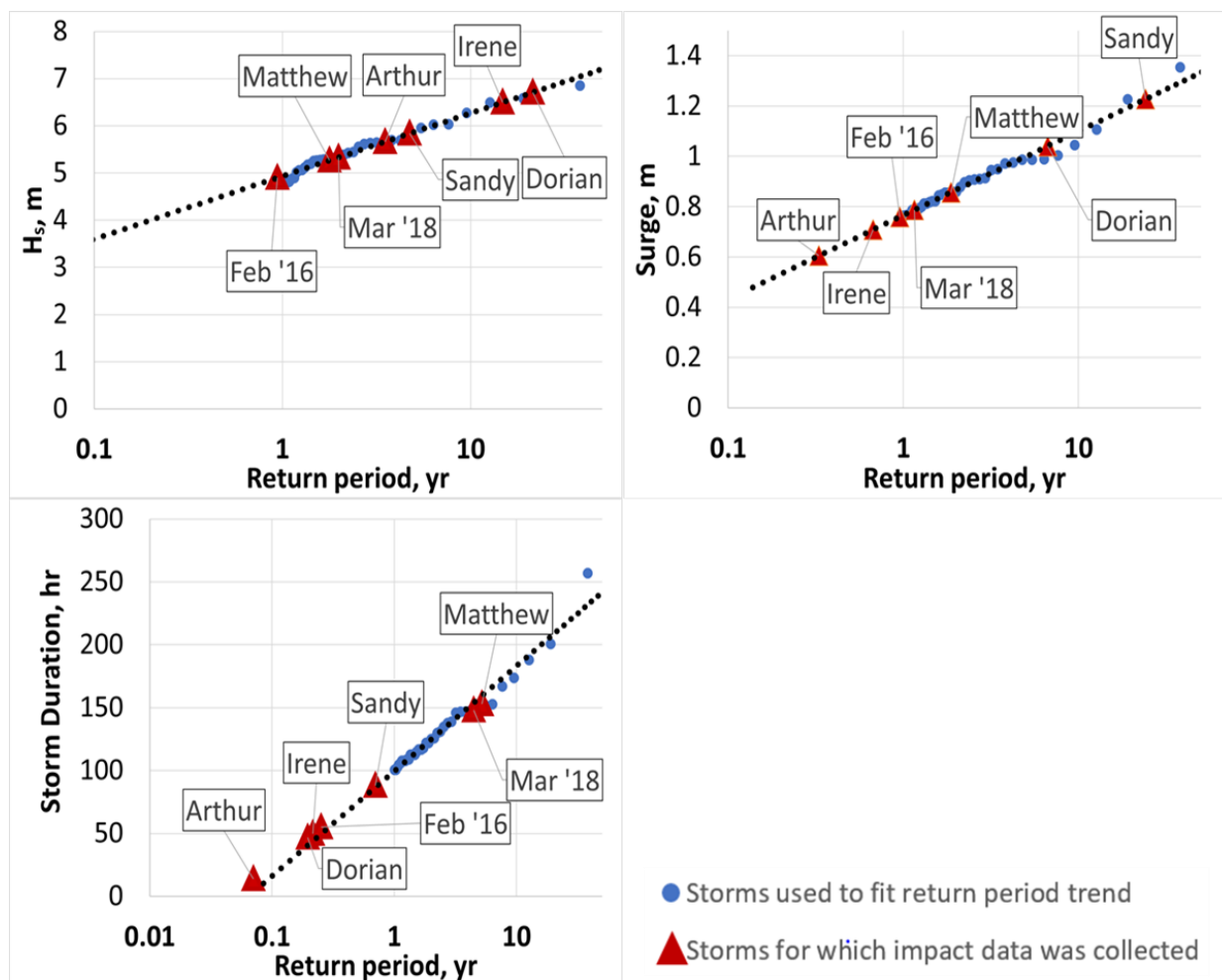


Figure 4.2 Return period analyses shown by blue dots and black-dotted best-fit line for each parameter: (a) Significant Wave Height, (b) Surge, and (c) Total Water Level. The return periods of the seven storms in the data set are shown by red triangles.

4.5 Vulnerability Thresholds and Storm Impact Risk

To determine the storms that the road is vulnerable to using a given indicator and threshold pair, the correlation between optimal thresholds and storm return periods (average of significant wave height, surge, and duration return periods) needs to be sufficiently strong. If a trend is not statistically significant, there is more of a chance that the correlation's existence is an anomaly due to the small sample size. Further, the confidence interval is tighter, i.e. there is less noise, around optimal thresholds interpolated from regression models with high coefficients of

determination (R^2). Interpolation errors, other than those originating from uncertainty in the regression model, could also arise from errors in the return period analysis, as explained in Section 4.4; the errors are minimal for return periods that are small relative to the 38 year data record, however.

Table 4.3 shows the critical R^2 at different levels of significance, which is the probability that the null hypothesis is true and there is no trend. A standard significance level is 0.05. The correlations between optimal thresholds and storms' severities are stronger for the multi-indicator functions than the individual indicators. For the individual indicators, three out of the six correlations between optimal threshold and storm return period shown in Figure 4.3 are significant at the 0.05 level. For the multi-indicator functions, six out of six of the correlations shown in Figure 4.4 are significant at the 0.05 level. The average R^2 of the linear regressions for the top six individual indicators is 24.5% lower than that of the top six multi-indicator functions. The average R^2 for the top six individual indicators and the top six multi-indicator functions are 0.40 and 0.53, respectively.

Table 4.3 Statistically significant coefficient of determination for different p-values with n=7 storms

| Significance level | Critical R^2 |
|---------------------------|----------------------------------|
| 0.1 | 0.34 |
| 0.05 | 0.44 |
| 0.01 | 0.64 |

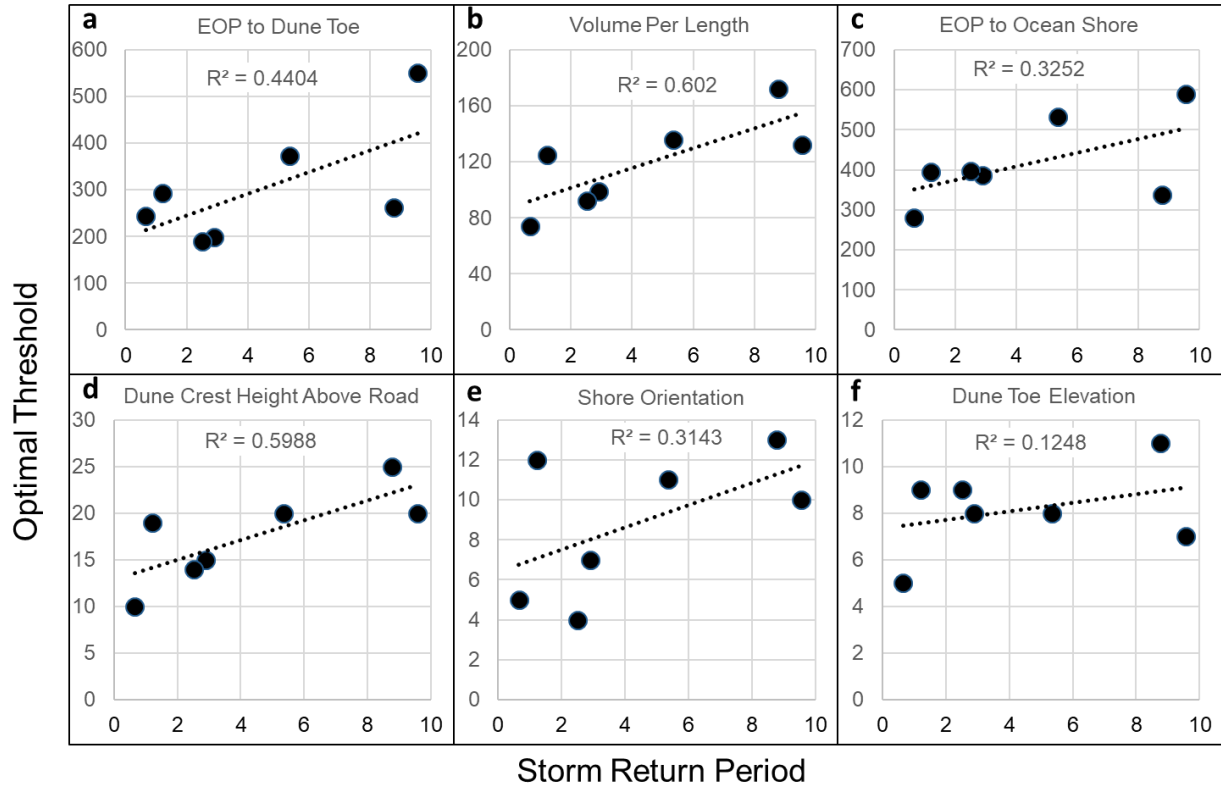


Figure 4.3 Linear relationship between optimal thresholds and storm return periods for each of the top six individual indicators. Storm return period along the x-axis is the average return period of storm surge, significant wave height, and storm duration. The optimal threshold, which can be thought of as the point at which the road becomes vulnerable based on a given indicator, is the threshold where F1-Score was maximized.

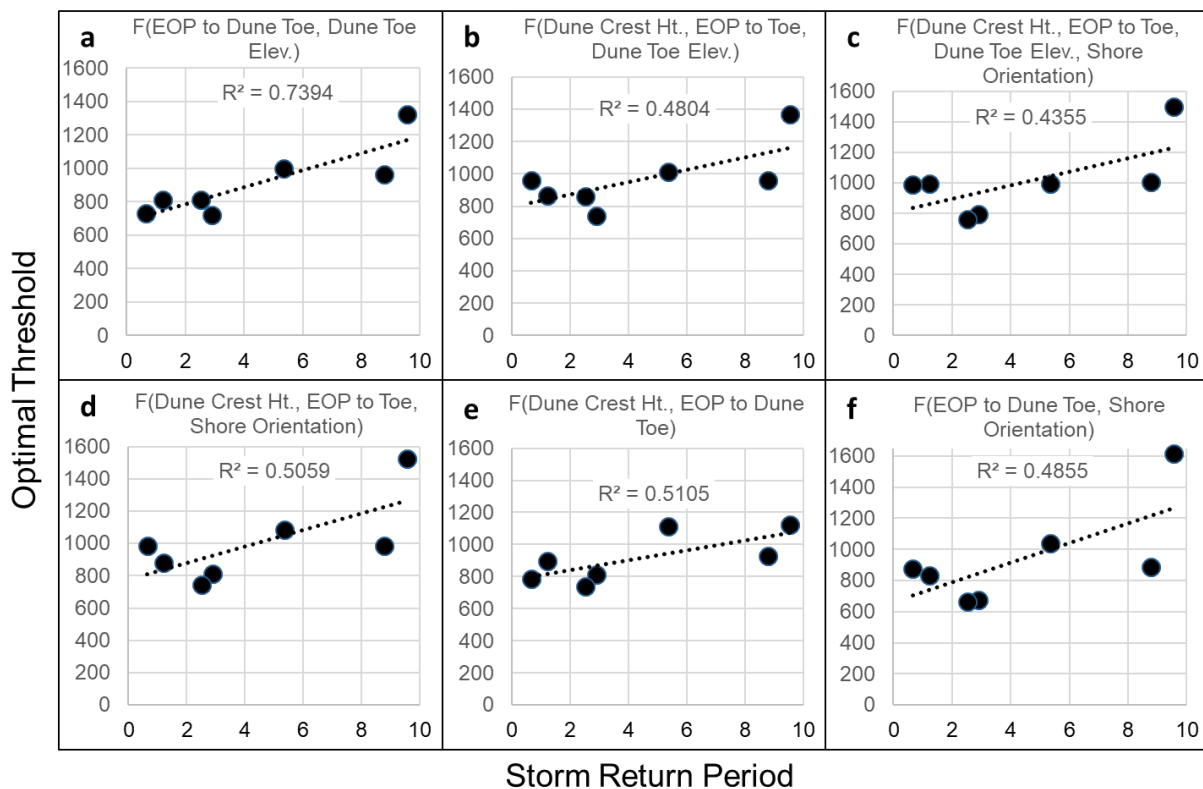


Figure 4.4 Linear relationship between optimal thresholds and storm return periods for each of the top six multi-indicator functions. Storm return period along the x-axis is the average return period of storm surge, significant wave height, and storm duration. The optimal threshold, which can be thought of as the point at which the road becomes vulnerable based on a given indicator, is the threshold where F1-Score was maximized.

4.6 Present [2020] and Future [2030] Vulnerability Assessments

Applying a vulnerability function to assess current vulnerability was as simple as collecting individual indicator data on a transect basis, multiplying the indicator values by weights from Table 4.2, and taking sums of the weighted indicators. Vulnerability predictions based on storm return period were made by selecting thresholds from Figure 4.4. Figure 4.5 delineates the stretches of NC12 in the north end of the study area that are currently (2020) vulnerable to 1-year storms in red, 5-year storms in orange, and 10-year storms in green. Black roadway was not predicted to be vulnerable to any of these storms. Stretches of road vulnerable to 1-year storms are also vulnerable to 5- and 10-year storms because those storms are more

severe. Likewise, stretches of road vulnerable to 5-year storms are also vulnerable to 10-year storms.

The predicted vulnerability of the road in 10 years (2030) is shown in Figure 4.6. The function of EOP to Dune Toe and Dune Toe Elevation was used to predict future vulnerability. The function was negligibly more skilled than the best individual indicator, EOP to Dune Toe, alone. Comparing results from Table 4.1 and Table 4.2, the PR AUC of the function of EOP to Dune Toe and Dune Toe Elevation is only 1.3% better than EOP to Dune Toe. This function was used to predict future vulnerability, rather than the individual indicator, because the function's correlation was significant at the 0.05 level (Figure 4.4(f)), whereas the individual indicator's correlation was not (Figure 4.3(a)). Thus, despite the indicators' skill being similar, predictions made with the function about vulnerability to specified return period storms should be more accurate.

Table 4.4 gives the length of NC12 within the study area that is currently vulnerable to the three return periods of storms. Table 4.5 gives the length of NC12 that is predicted to be vulnerable to each of the three storm classes in 10 years. In both tables, the length of road that is vulnerable increases with severity of storm because more stretches of road are likely to be impacted during an extreme storm. Table 4.5, the 10-year (2030) predictions, shows a greater length of road vulnerable for each storm return period than in Table 4.4, the current (2020) vulnerability assessment. More road is likely to be vulnerable in the future as the majority of the study area's shoreline is eroding and becoming closer to the road. Changes in the shore's orientation does little to modulate the increase in vulnerable roadway that is predicted.

Table 4.4 Length of road in study area vulnerable to different return period storms at present (2020) according to function of EOP to Dune Toe and Dune Toe Elevation

| Present conditions (August 2020) | |
|----------------------------------|-------------------------------|
| Storm return period (yr) | Length of road vulnerable (m) |
| 1 | 5514 |
| 5 | 8248 |
| 10 | 11618 |

Table 4.5 Length of road in study area vulnerable to various return period storms in 10 years (2030) according to function of EOP to Dune Toe and Shore Orientation

| Future conditions (2030) | |
|--------------------------|-------------------------------|
| Storm return period (yr) | Length of road vulnerable (m) |
| 1 | 7806 |
| 5 | 11063 |
| 10 | 13241 |

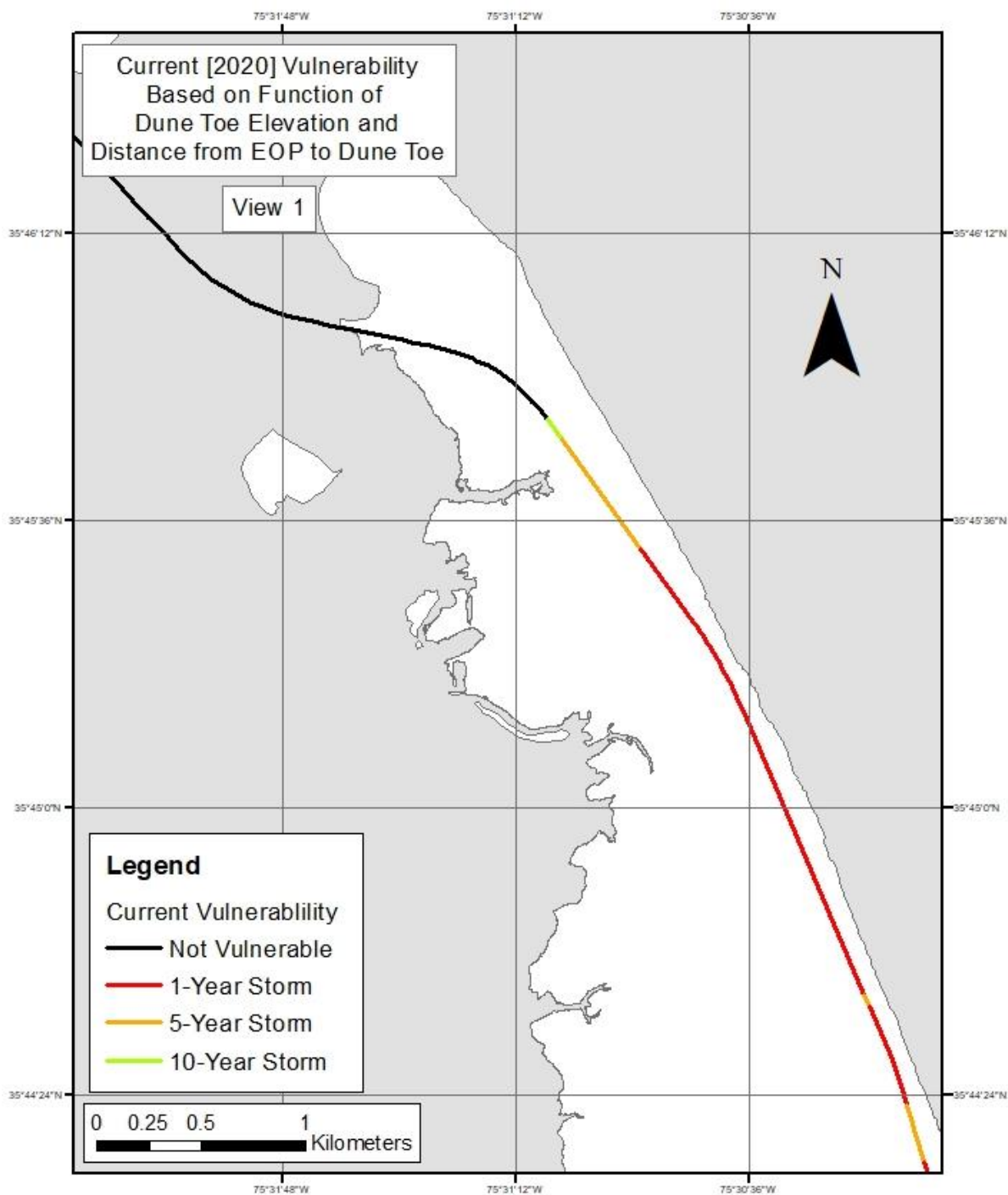


Figure 4.5 Map of parts of NC 12 that were predicted vulnerable to storm impacts. Assessment was performed on the present (August 2020) state of the road and topography using a weighted linear function of EOP to Dune Toe and Dune Toe Elevation. View 1 of 6. Views 2-6 showing the remainder of the study are presented in Appendix A.

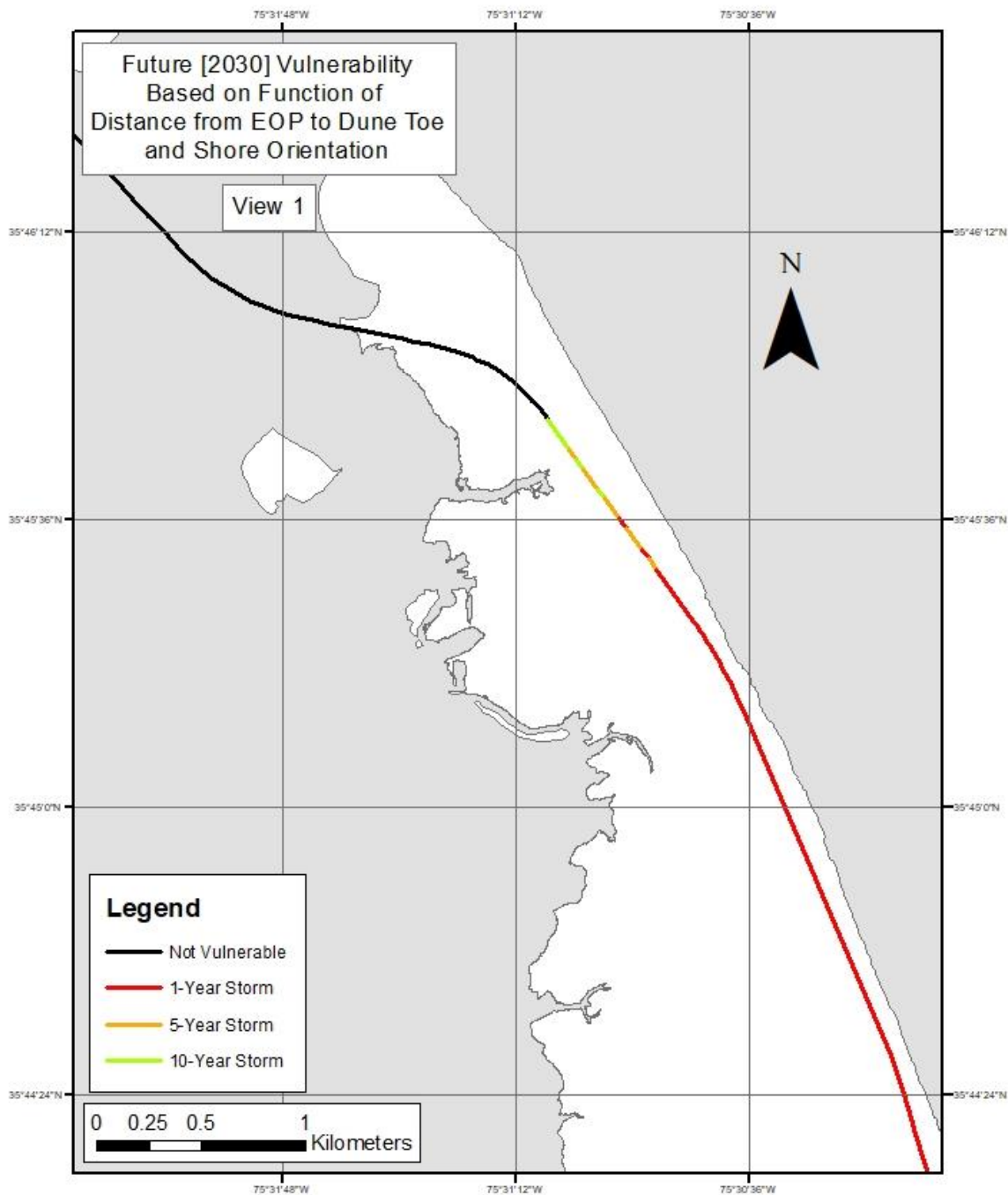


Figure 4.6 Map of parts of NC 12 that were predicted vulnerable to storm impacts. Assessment was performed on the predicted future (10-year projection / August 2030) state of the road and topography using a weighted linear function of EOP to Dune Toe and Shore Orientation. View 1 of 6. Views 2-6 showing the remainder of the study area are presented in Appendix B.

4.7 Discussion

Binary classification model metrics were employed to assess the skill of 14 indicators in predicting coastal highway vulnerability. There are several simple morphological indicators that can predict highway vulnerability to coastal storm impacts; however, some indicators are significantly better at predicting vulnerability than others. EOP to Dune Toe, Volume Per Length, and EOP to Ocean Shore were significantly more skilled at predicting vulnerability than the other indicators tested. Other indicators that were more skilled than a random indicator are Dune Crest Height Above the Road, Moving Averaged Dune Crest Height Above the Road, Beach Slope, Dune Toe Elevation, and Shore Orientation. EOP to Dune Toe, EOP to Ocean Shore, and Shore Orientation proved to be robust indicators, and they are especially powerful because they are easily computed and can be used to predict vulnerability on a decadal timescale.

Shoreline positions with 95% prediction bounds can be projected at a decadal time scale by performing a regression on the time series of shoreline positions (Velasquez-Montoya et al. 2021). Then, the distance from EOP to ocean shoreline indicator can easily be computed at any desired spatial scale and resolution with the predicted ocean shorelines and known highway alignment. Using the same projected shorelines, shoreline orientation could be calculated and used to estimate future vulnerability, as well. The slope of the regression, which is the rate of shoreline erosion, can be used to project the EOP to Dune Toe, if it is assumed that the toe migrates at the same rate as the shoreline.

The ease with which indicators are calculated makes regional-scale coastal highway vulnerability assessments feasible. To illustrate the potential, EOP to Ocean Shore was used to perform a present-day vulnerability assessment across the entire coastline of North Carolina, using publicly-available transects employed by the North Carolina Division of Coastal

Management, NC DOT road shapefiles, and shoreline shapefiles publicly available via the North Carolina Department of Environmental Quality. Figure 4.8 displays the degree of vulnerability to storm impacts based on the value of the EOP to Ocean Shore at each transect. This assessment was done on the most recent shorelines to illustrate the potential application of the concepts presented here, but similar analyses could be performed with other indicators, as well. Additionally, future vulnerability could be assessed at a regional-scale with these indicators if enough data is available to project them.

Island Width, Distance from EOP to Estuary Shore, Beach Width, Inverse Beach Slope, and Road Elevation were found to be unskilled indicators of highway vulnerability to storm impacts. The predominance of overwash impacts in the dataset should be noted when considering the results. Using the present storm datasets, Island Width and Distance from EOP to Estuary Shore appear to be unskilled indicators; but a different framework should be devised to appropriately assess them in future work, since they may be more indicative of island breaching and estuarine-side events than ocean-side events (Velasquez-Montoya et al., 2021). Other limitations that may have affected this study's results were the statistical distributions of indicator values. An indicator's distribution of values is a quality of the study area – the location's morphology as well as the size of the area. Narrowly distributed indicators do not allow for adequate differentiation between transects with at the low end of an indicator's spectrum versus the high end, which can make vulnerability predictions less distinct. Road Elevation on its own was found to be an unskilled indicator; however, consideration of Road Elevation as an indicator may have been limited by the fact that there was minimal spatial or temporal variation in the highway's elevation along the study area. The limited spread of Road Elevation's values can be seen in Figure 4.7, which compares the box-and-whisker plots of

mean-normalized values for each indicator. The data for each indicator has been divided by its mean to allow for comparison among the indicators. Road Elevation values are the least widely distributed of all the indicators, with the values ranging between 38 and 156% of the indicator's mean. In-depth analysis of the distributions of indicators with histograms confirmed that Road Elevation had an especially narrow range of values, as is evident by comparing Figure C.10 with the other histograms in Appendix C. The evaluated performance of other indicators were not restricted by statistical distributions. The next most narrowly distributed indicator was Dune Toe Elevation, but this indicator was found to be significantly skilled. Beach Width was another indicator found in this present study to be unskilled. Beach Width is a relevant control of beach and dune impacts (Claudino-Sales et al., 2008; Beuzen et al., 2019), but when considering the beach's width from the perspective of predicting highway vulnerability, it was found to counter-productive at worst, or irrelevant at best. It may be that gently sloping beaches are quickly inundated due to elevated water levels, and therefore the beach width is rendered an unimportant variable during storms. This also explains why the EOP to Dune Toe indicator was a better vulnerability predictor than EOP to Ocean Shore. EOP to Dune Toe is the distance from EOP to ocean shore, with the beach's width subtracted. The dataset of storm impacts to the road was limited by the availability of post-storm imagery. Storms with post-storm imagery were generally larger and more intense, like hurricanes; however, it is well known that much smaller events can also cause impacts to the most vulnerable portions of NC 12 in the study area, as evident in social media posts by NC DOT as well as closure alerts at the DriveNC.gov website. The optimal threshold and Max F1-Score are dependent on the storms in the dataset. As the overall severity of storms increases, the optimal threshold increases to classify more transects in the study area as vulnerable. Therefore, the optimal threshold determined from an aggregated set

of storms might not be the threshold that is best for a particular application. The information conveyed by the threshold versus storm-return-period relationships is useful for tuning the threshold to meet a specific goal or level of allowable risk.

The optimization results supported the hypothesis that a function of multiple, continuous indicator variables would be more skilled than any single indicator. A weighted linear function of Dune Toe Elevation and EOP to Dune Toe was found to be 6.5% more skilled than the best individual indicator (EOP to Dune Toe), based on PR AUC. There are six other functions (Table 4.2) found to be slightly more skilled than EOP to Dune Toe (Table 4.1), as well. In addition to greater predictive skill, the top six functions also have better correlations between their threshold value and storm return period, which makes them more appropriate for quantifying the severity of storm the road is predicted vulnerable to. Using a multi-indicator function accounts for more factors that affect the road's level of vulnerability, which reduces the uncertainty around threshold values. The appropriate weights needed to scale indicator variables were found by applying mixed integer linear programming to a dataset of observed highway impacts and pre-storm indicator values. Research has pointed out the difficulties and inconsistencies in applying existing multivariable coastal vulnerability indices (Koroglu et al., 2019), so this optimization technique may be a valuable tool for objectively identifying variable weights. Usage of a weighted linear function, rather than an index like the CVI, allows the individual variables to remain continuous, eliminating issues surrounding discretizing variables into suitable classes.

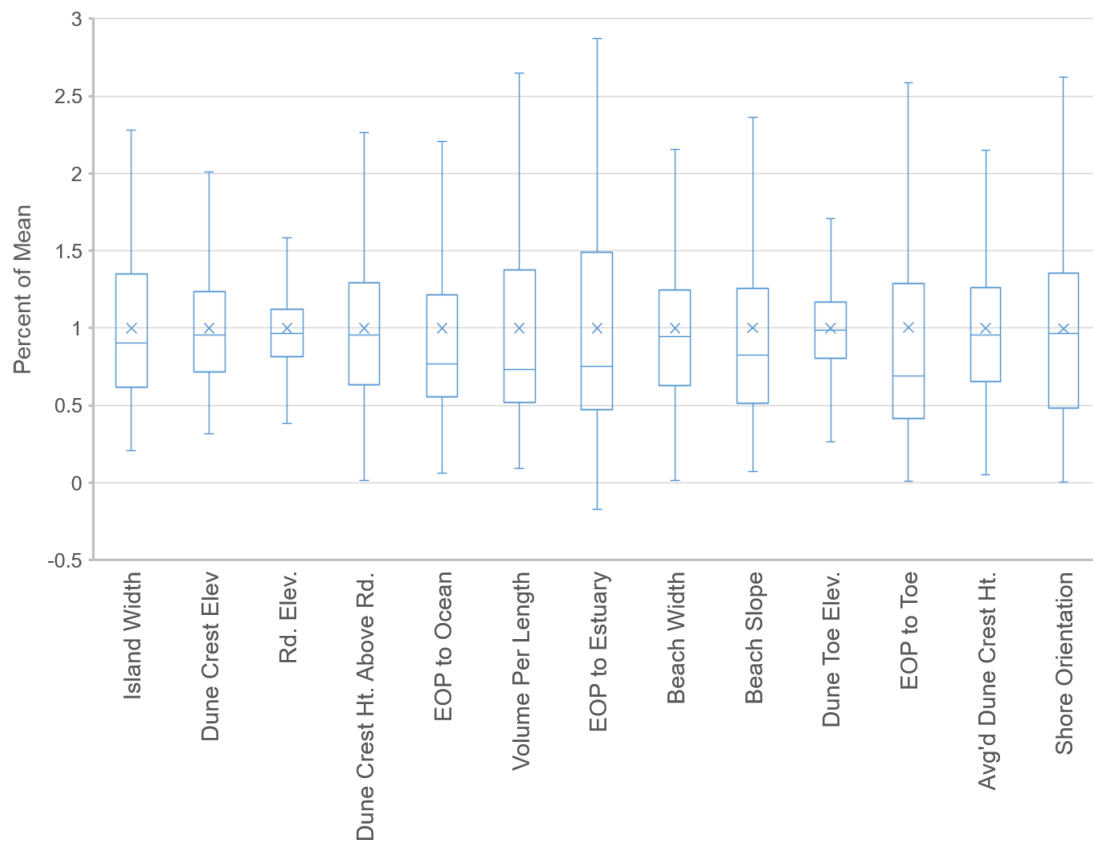


Figure 4.7 Box-and-whisker plot of each indicator's values normalized by their average, which summarizes the spread of values around each indicator's mean. The top and bottom whiskers correspond to the maxima and minima. The tops and bottoms of the boxes correspond to the upper and lower quartiles of the data. The x's are the means, which are all 1 because the data has been normalized by the mean. The line within each box represents the median.

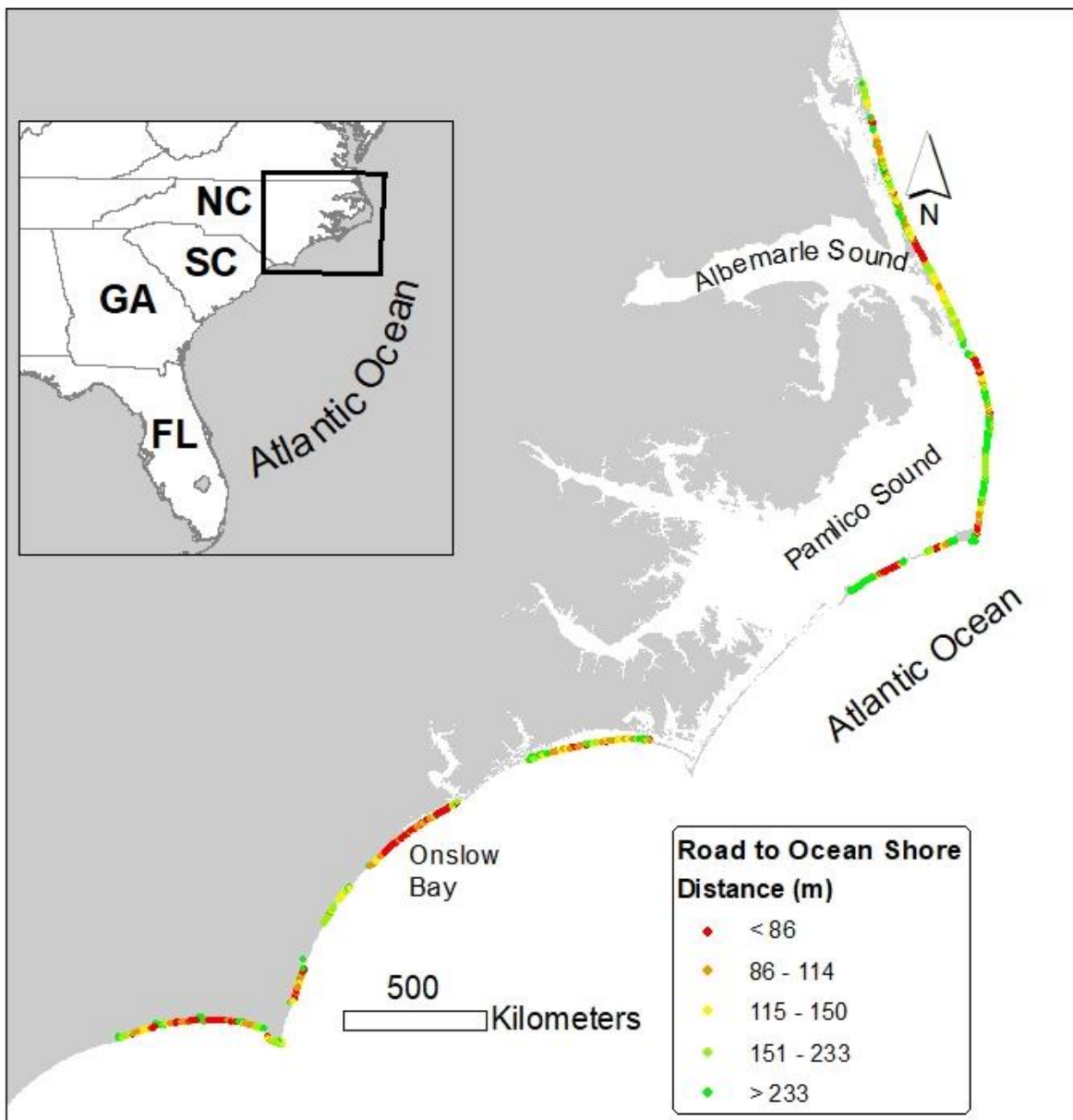


Figure 4.8 Statewide vulnerability assessment of North Carolina's most seaward roads based on the EOP to Ocean Shore indicator

CHAPTER 5: CONCLUSIONS AND FUTURE WORK

5.1 Conclusions

From a dataset of observed storm impacts that occurred to a barrier island highway over seven storms, it was found that EOP to Dune Toe, Volume per Length, EOP to Ocean Shore Distance, Smoothed Dune Crest Height Above the Road, Dune Crest Height Above the Road, Dune Elevation, Shore Orientation, Dune Toe Elevation, and Beach Slope (in order of decreasing skill) were skilled predictors of highway vulnerability to storm impacts. It was found that incorporating multiple geomorphological parameters into a weighted linear function—such as of EOP to Dune Toe and Dune Toe Elevation—improved predictions of vulnerability. This present study provides empirical evidence supporting that these simple, geomorphological variables are good indicators of coastal highway vulnerability, as they can predict a significant amount of the spatial and temporal variation in storm impacts. The present study also supports the hypothesis that a multi-indicator function may more accurately predict vulnerability. Finally, connections are made between return period of storms and thresholds of indicators, which empower vulnerability predictions based on risk to a specified severity-level of storm. Resilience planners can be confident that coastal infrastructure vulnerability studies employing these indicators can effectively identify the most at-risk areas.

5.2 Future Work

Future work could further investigate the effectiveness of indicators and use additional data sets to reproduce the results and confirm that the results are applicable to other coastal areas outside of the current study area, Pea Island, NC. This could be done with other datasets of documented storm impacts to infrastructure, or numerical modeling of hydrodynamics and

morphodynamics could be employed to create a dataset of synthetic storms and corresponding roadway impacts.

Indicators explored in this study and others could be evaluated with an emphasis on predicting areas vulnerable to the damaging storm impacts like pavement erosion and island breaching, since the present study was limited by a dearth of occurrences of erosion damage or island breaching damage.

Other future work could test the validity of methods used in this present study to project indicators, like EOP to Dune Toe, EOP to Ocean Shore, and Shore Orientation, and future work could explore methods to project other indicators, like Dune Crest Height and Dune Toe Elevation, for use in predicting future vulnerability.

REFERENCES

- Belotti, P., Kirches, C., Leyffer, S., Linderoth, J., Luedtke, J., & Mahajan, A. (2013). Mixed-integer nonlinear optimization. *Acta Numerica*, 22, 1–131.
<https://doi.org/10.1017/S0962492913000032>
- Beuzen, T., Harley, M. D., Splinter, K. D., & Turner, I. L. (2019). Controls of Variability in Berm and Dune Storm Erosion. *Journal of Geophysical Research: Earth Surface*, 124(11), 2647–2665. <https://doi.org/10.1029/2019JF005184>
- Bruun, P. (1962). Sea-level rise as a cause of shore erosion. *Journal of the Waterways and Harbors Division*, 88(1), 117–130.
- Camm, J. D., Raturi, A. S., & Tsubakitani, S. (1990). Cutting Big M Down to Size. *Interfaces*, 20(5), 61–66. <https://doi.org/10.1287/inte.20.5.61>
- Carter, R. (1988). *Coastal environments: an introduction to the physical, ecological and cultural systems of coastlines*. Academic Press.
- Claudino-Sales, V., Wang, P., & Horwitz, M. H. (2008). Factors controlling the survival of coastal dunes during multiple hurricane impacts in 2004 and 2005: Santa Rosa barrier island, Florida. *Geomorphology*, 95(3–4), 295–315.
<https://doi.org/10.1016/j.geomorph.2007.06.004>
- Davidson-Arnott, R. G. D. (2005). Conceptual model of the effects of sea level rise on sandy coasts. *Journal of Coastal Research*, 21(6), 1166–1172. <https://doi.org/10.2112/03-0051.1>
- Davis, J., & Goadrich, M. (2006). The Relationship Between Precision-Recall and ROC Curves. *Proceedings of the 23rd International Conference on Machine Learning*.
- Dolan, R., Hayden, B. P., May, P., & May, S. (1980). The reliability of shoreline change measurements from aerial photographs. *Shore and Beach*, 48(4), 22–29.
- Dolan, R., & Davis, R. (1992). An intensity scale for Atlantic Coast northeast storms. *Journal of Coastal Research*, 8(4), 840–853.
- Donnelly, C., Hanson, H., & Larson, M. (2009). A numerical model of coastal overwash. *Proceedings of the Institution of Civil Engineers: Maritime Engineering*, 162(3), 105–114.
<https://doi.org/10.1680/maen.2009.162.3.105>
- Doran, K. S., Long, J. W., & Overbeck, J. R. (2015). *A method for determining average beach slope and beach slope variability for U.S. sandy coastlines*.
<https://doi.org/10.3133/ofr20151053>
- Douglass, S. L., & Krolak, J. (2008). *Highways in the Coastal Environment, Hydraulic Engineering Circular 25, Second Edition (Issue 25)*.

- Enríquez, A. R., Marcos, M., Falqués, A., & Roelvink, D. (2019). Assessing beach and dune erosion and vulnerability under sea level rise: A Case study in the Mediterranean Sea. *Frontiers in Marine Science*, 6(JAN), 1–12. <https://doi.org/10.3389/fmars.2019.00004>
- European Academies Science Advisory Council (EASAC). (2013). *Trends in extreme weather events in Europe: implications for national and European Union adaptation strategies* EASAC.
- Figlus, J., Kobayashi, N., Gralher, C., & Iranzo, V. (2011). Wave overtopping and overwash of dunes. *Journal of Waterway, Port, Coastal and Ocean Engineering*, 137(1), 26–33. [https://doi.org/10.1061/\(ASCE\)WW.1943-5460.0000060](https://doi.org/10.1061/(ASCE)WW.1943-5460.0000060)
- Francis, O., Brandes, H., Zhang, G., Ma, D., Yang, L., Doygun, O., Togia, H., Rossi, C., & Costanzo, G. (2019). *Statewide Coastal Highway Program Report. Prepared for the State of Hawaii Department of Transportation.*
- Gornitz, V. M., Daniels, R. C., White, T. W., & Birdwell, K. R. (1994). The Development of a Coastal Risk Assessment Database: Vulnerability to Sea-Level Rise in the U.S. Southeast. *Journal of Coastal Research*, ArticleType: research-article / Issue Title: Special Issue No. 12. COASTAL HAZARDS: PERCEPTION, SUSCEPTIBILITY AND MITIGATION / Full publication date: 1994 / Copyright © 1994 Coastal Education & Research Foundation, Inc., 327–338. <http://www.jstor.org/stable/25735608>
- Hallermeier, R. J., & Rhodes, P. E. (1988). *Generic treatment of dune erosion for 100-year event.* 1197–1211. <https://doi.org/10.9753/icce.v21.89>
- Halls, J. N., & Randall, A. L. (2018). Nesting patterns of loggerhead sea turtles (*Caretta caretta*): Development of a multiple regression model tested in North Carolina, USA. *ISPRS International Journal of Geo-Information*, 7(9). <https://doi.org/10.3390/ijgi7090348>
- Houser, C. (2009). Geomorphological controls on road damage during hurricanes ivan and dennis. *Journal of Coastal Research*, 25(3), 558–568. <https://doi.org/10.2112/07-0923.1>
- Holland, J. H. (1992). Genetic Algorithms. *Scientific American*, 267(1), 66–73.
- Judge, E. K., Overton, M. F., & Fisher, J. S. (2003). Vulnerability indicators for coastal dunes. *Journal of Waterway, Port, Coastal and Ocean Engineering*, 129(6), 270–278. [https://doi.org/10.1061/\(ASCE\)0733-950X\(2003\)129:6\(270\)](https://doi.org/10.1061/(ASCE)0733-950X(2003)129:6(270))
- Kafalenos, R., Leonard, K., Beagan, D., Burkett, V., Keim, B., Meyers, A., Hunt, D., & Hyman, R. (2008). What are the Implications of Climate Change and Variability for Gulf Coast Transportation? In *Impacts of Climate Change and Variability on Transportation Systems and Infrastructure: Gulf Coast Study, Phase I.*

- Koroglu, A., Ranasinghe, R., Jiménez, J. A., & Dastgheib, A. (2019). Comparison of Coastal Vulnerability Index applications for Barcelona Province. *Ocean and Coastal Management*, 178(August), 104799. <https://doi.org/10.1016/j.ocecoaman.2019.05.001>
- Kriebel, D., Dalrymple, R., Pratt, A., & Sakovich, V. (1996). Shoreline risk index for northeasterners. *Proceedings of the 1996 Conference on Natural Disaster Reduction*, 251–252.
- Kuo, J. Y. J., Romero, D. A., Beck, J. C., & Amon, C. H. (2016). Wind farm layout optimization on complex terrains – Integrating a CFD wake model with mixed-integer programming. *Applied Energy*, 178, 404–414. <https://doi.org/10.1016/j.apenergy.2016.06.085>
- Levine, J. F., Apperson, C. S., Levin, M., Kelly, T. R., Kakumanu, M. L., Ponnusamy, L., Sutton, H., Salger, S. A., Caldwell, J. M., & Szempruch, A. J. (2017). Stable Transmission of *Borrelia burgdorferi* Sensu Stricto on the Outer Banks of North Carolina. *Zoonoses and Public Health*, 64(5), 337–354. <https://doi.org/10.1111/zph.12302>
- Li, H., Lin, L., & Burks-Copes, K. A. (2013). Modeling of coastal inundation, storm surge, and relative sea-level rise at Naval Station Norfolk, Norfolk, Virginia, U.S.A. *Journal of Coastal Research*, 29(1), 18–30. <https://doi.org/10.2112/JCOASTRES-D-12-00056.1>
- Mathworks. (n.d.). Integer Programming. <https://www.mathworks.com/discovery/integer-programming.html>
- Mathworks. (n.d.). Genetic Algorithm. <https://www.mathworks.com/discovery/genetic-algorithm.html>.
- Mimura, N. (2013). Sea-level rise caused by climate change and its implications for society. *Proceedings of the Japan Academy Series B: Physical and Biological Sciences*, 89(7), 281–301. <https://doi.org/10.2183/pjab.89.281>
- Mitasova, H., Overton, M., & Harmon, R. S. (2005). Geospatial analysis of a coastal sand dune field evolution: Jockey’s Ridge, North Carolina. *Geomorphology*, 72(1–4), 204–221. <https://doi.org/10.1016/j.geomorph.2005.06.001>
- NC Coastal Resources Commission Science Panel. (2015). *NC Sea Level Rise Assessment Report*. [https://files.nc.gov/ncdeq/Coastal Management/documents/PDF/Science Panel/2015 NC SLR Assessment-FINAL REPORT Jan 28 2016.pdf](https://files.nc.gov/ncdeq/Coastal%20Management/documents/PDF/Science%20Panel/2015%20NC%20SLR%20Assessment-FINAL%20REPORT%20Jan%2028%202016.pdf)
- NC Division of Coastal Management (NCDCM). (2016). *Beach Nourishment - A Report to the North Carolina General Assembly Joint Legislative Oversight Committee on Agriculture, Natural and Economic Resources*.
- NC Department of Transportation (NCDOT). (2008). *Final Environmental Impact Statement and Section 4(f) Evaluation* (Vol. 1). <http://data.wsdot.wa.gov/publications/viaduct/AWVFEIS-Chapters.pdf>

- Neumann, B., Vafeidis, A. T., Zimmermann, J., & Nicholls, R. J. (2015). Future Coastal Population Growth and Exposure to Sea-Level Rise and Coastal Flooding - A Global Assessment. *PLoS ONE*. <https://doi.org/10.1371/journal.pone.0118571>
- National Oceanic and Atmospheric Administration (NOAA). (2018). *NDBC About Us*. ndbc.noaa.gov/ndbc.shtml
- National Oceanic and Atmospheric Administration (NOAA). (2020). *Emergency Response Imagery*. <https://storms.ngs.noaa.gov>
- Ortiz, A. C., Roy, S., & Edmonds, D. A. (2017). Land loss by pond expansion on the Mississippi River Delta Plain. *Geophysical Research Letters*, *44*(8), 3635–3642. <https://doi.org/10.1002/2017GL073079>
- Overton, M. F., & Fisher, J. S. (2007). *Proposed NC12 Improvements NCDOT TIP Project Number R-3116D Rodanthe Hotspot - Interim Solution. Shoreline Change and Stabilization Analysis*. May, 15.
- Overton, M., & Fisher, J. (2005). *NC Coastal Highway Vulnerability [Prepared for NCDOT]*.
- Overton, M., & Fisher, J. (2000). *NC12 Vulnerability Analysis [Prepared for NCDOT]*.
- Pfaller, J. B., Pajuelo, M., Vander Zanden, H. B., Andrews, K. M., Dodd, M. G., Godfrey, M. H., Griffin, D. B., Ondich, B. L., Pate, S. M., Williams, K. L., Shamblin, B. M., Nairn, C. J., Bolten, A. B., & Bjorndal, K. A. (2020). Identifying patterns in foraging-area origins in breeding aggregations of migratory species: Loggerhead turtles in the Northwest Atlantic. *PLoS ONE*, *15*(4), 1–22. <https://doi.org/10.1371/journal.pone.0231325>
- Plomaritis, T. A., Ferreira, Ó., & Costas, S. (2018). Regional assessment of storm related overwash and breaching hazards on coastal barriers. *Coastal Engineering*, *134*(February 2017), 124–133. <https://doi.org/10.1016/j.coastaleng.2017.09.003>
- Provost, F., Fawcett, T., & Kohavi, R. (1998). The Case Against Accuracy Estimation for Comparing Induction Algorithms. *Proceedings of the Fifteenth International Conference on Machine Learning*.
- Provost, L. (2021). Wave Rose Function (<https://www.mathworks.com/matlabcentral/fileexchange/67023-wave-rose-function>), MATLAB Central File Exchange. Retrieved July 22, 2021.
- Rogers, S. (2007). Beach nourishment for hurricane protection: North Carolina project performance in Hurricanes Dennis and Floyd. *Shore and Beach*, *75*(1), 37.
- Safak, I., Warner, J., & List, J. (2016). Barrier island breach evolution: Alongshore transport and bay-ocean pressure gradient interactions. *Journal of Geophysical Research: Oceans*, *121*(8), 1–14. <https://doi.org/10.1002/2016J>

- Sallenger, A. H. (2000). Storm impact scale for barrier islands. *Journal of Coastal Research*, 16(3), 890–895.
- Scheffner, N., Clausner, J., Militello, A., Borgman, L., Edge, B., & Grace, P. (1999). *Use and Application of the Empirical Simulation Technique: User's Guide*. CHL-99-21, 194.
- Sciaudone, E. J., Velasquez-Montoya, L., Smyre, E. A., & Overton, M. F. (2016). Spatial and Temporal Variability in Dune Field: Pea Island, North Carolina. *Shore & Beach*, 84(2), 49–58.
- Small, C., & Nicholls, R. J. (2003). A global analysis of human settlement in coastal zones. *Journal of Coastal Research*, 19(3), 584–599.
- Stauble, D., Seabergh, W., & Hales, L. (1990). Erosion characteristics of Hurricane Hugo on the beaches of South Carolina. *Shore and Beach*, 58(4), 23–3662.
- Stockdon, H. F., Holman, R. A., Howd, P. A., & Sallenger, A. H. (2006). Empirical parameterization of setup, swash, and runup. *Coastal Engineering*.
<https://doi.org/10.1016/j.coastaleng.2005.12.005>
- Stockdon, H. F., Plant, N. G., & Sallenger, A. H. (2009). National assessment of hurricane-induced coastal change vulnerability. *Shore & Beach*, 77(3), 15–20.
- Tracy, B. A., & Cialone, A. (2006). *Comparison of Gulf of Mexico Wave Information Studies (WIS) 2-G Hindcast with 3-G Hindcasting*.
- US Army Corps of Engineers (USACE). (2008). *Coastal Engineering Manual, 1110-2-1100, Part II* (Vol. 1100, Issues 1110-2–1100, Part II, Change 4 2015).
- US Fish and Wildlife Service (USFWS). (2020). *About pea island national wildlife refuge*.
https://www.fws.gov/refuge/Pea_Island/about.html
- US Global Change Research Program (USGCRP). (2018). *Impacts, Risks, and Adaptation in the United States: Vol. II*. <https://doi.org/10.7930/NCA4.2018.CH21>
- van de Graaff, J. (1986). Probabilistic design of dunes; an example from the Netherlands. *Coastal Engineering*, 9(5), 479–500.
- van Ijzendoorn, C. O., de Vries, S., Hallin, C., & Hesp, P. A. (2021). Sea level rise outpaced by vertical dune toe translation on prograding coasts. *Scientific Reports*, 11(1), 1–8.
<https://doi.org/10.1038/s41598-021-92150-x>
- Velasquez-Montoya, L., Sciaudone, E. J., Mitasova, H., & Overton, M. F. (2018). Observation and modeling of the evolution of an ephemeral storm-induced inlet: Pea Island Breach, North Carolina, USA. *Continental Shelf Research*, 156(February), 55–69.
<https://doi.org/10.1016/j.csr.2018.02.002>

- Velasquez-Montoya, L., & Overton, M. F. (2017). Impacts of seasonal forcings on the hydrodynamics of Oregon Inlet, NC. *Coastal Dynamics*, 055, 1240–1250.
- Velasquez-Montoya, L., Sciaudone, E. J., Smyre, E., & Overton, M. F. (2021). Vulnerability indicators for coastal roadways based on barrier island morphology and shoreline change predictions. *Natural Hazards Review*, 22(2006), 1–16.
[https://doi.org/10.1061/\(ASCE\)NH.1527-6996.0000441](https://doi.org/10.1061/(ASCE)NH.1527-6996.0000441)

APPENDICES

Appendix A: Present [2020] Vulnerability Assessment

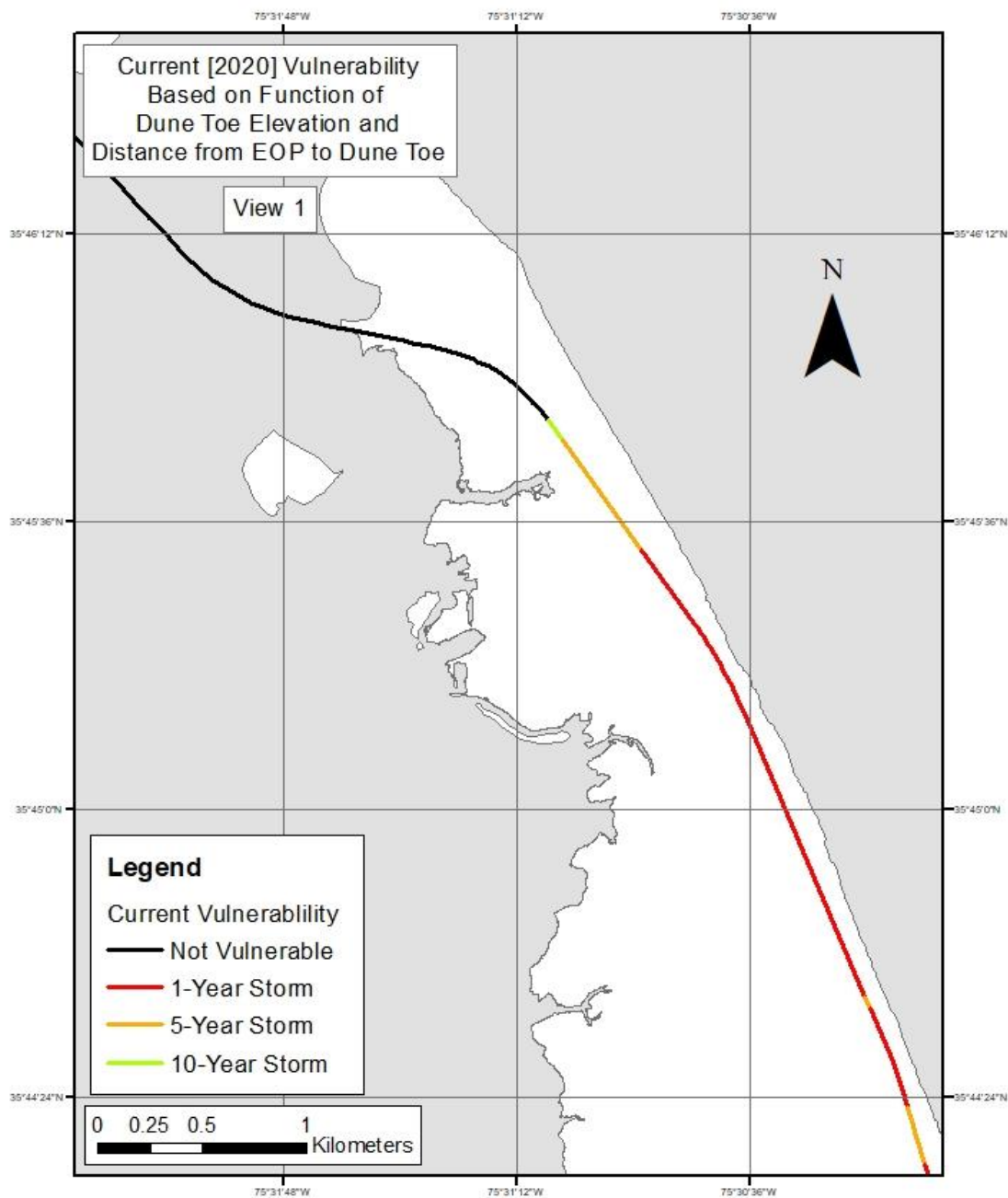


Figure A.1 Map of parts of NC 12 that were predicted vulnerable to storm impacts. Assessment was performed on the present (August 2020) state of the road and topography using a weighted linear function of EOP to Dune Toe and Dune Toe Elevation. View 1 of 6.

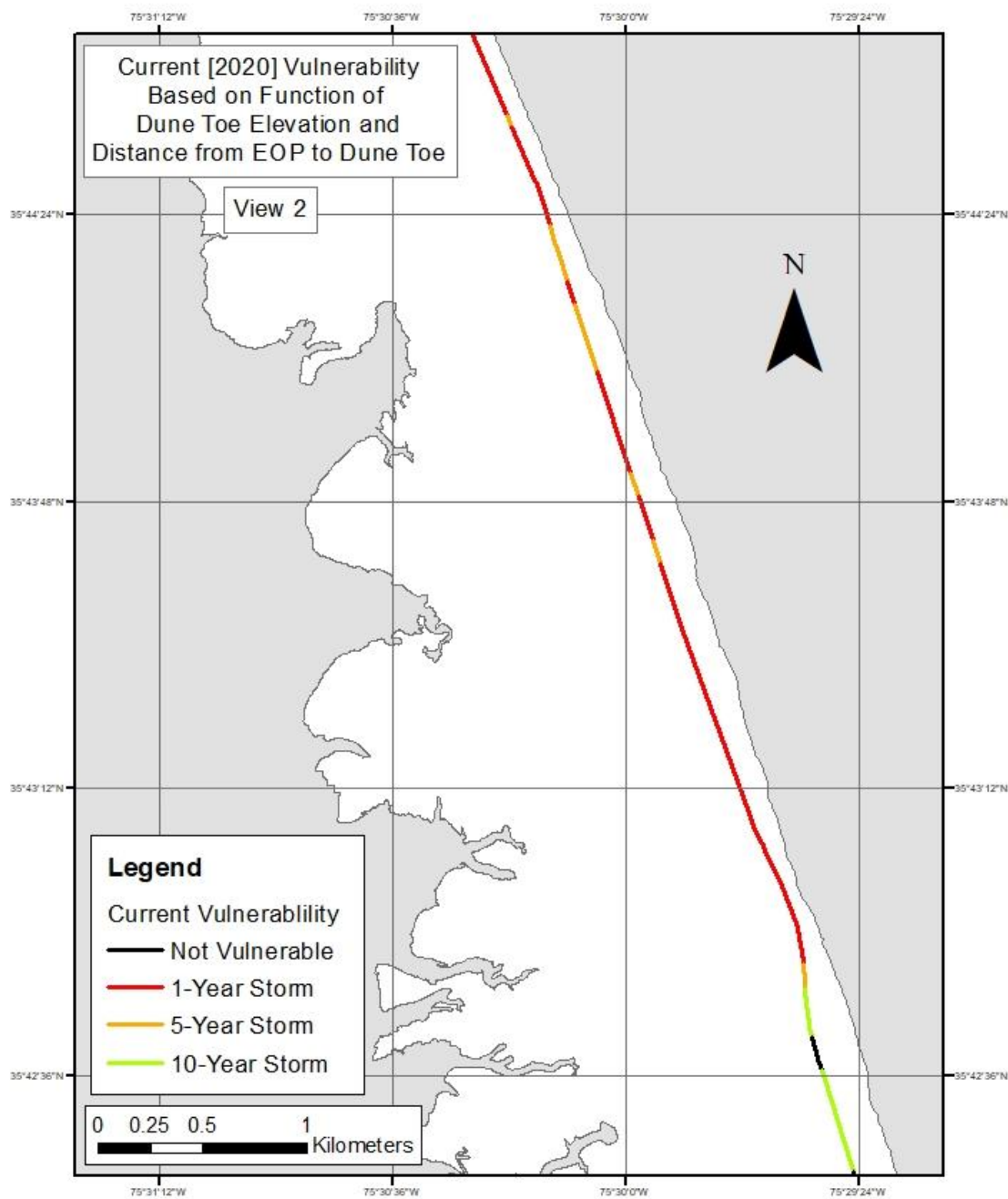


Figure A.2 Map of parts of NC 12 that were predicted vulnerable to storm impacts. Assessment was performed on the present (August 2020) state of the road and topography using a weighted linear function of EOP to Dune Toe and Dune Toe Elevation. View 2 of 6.

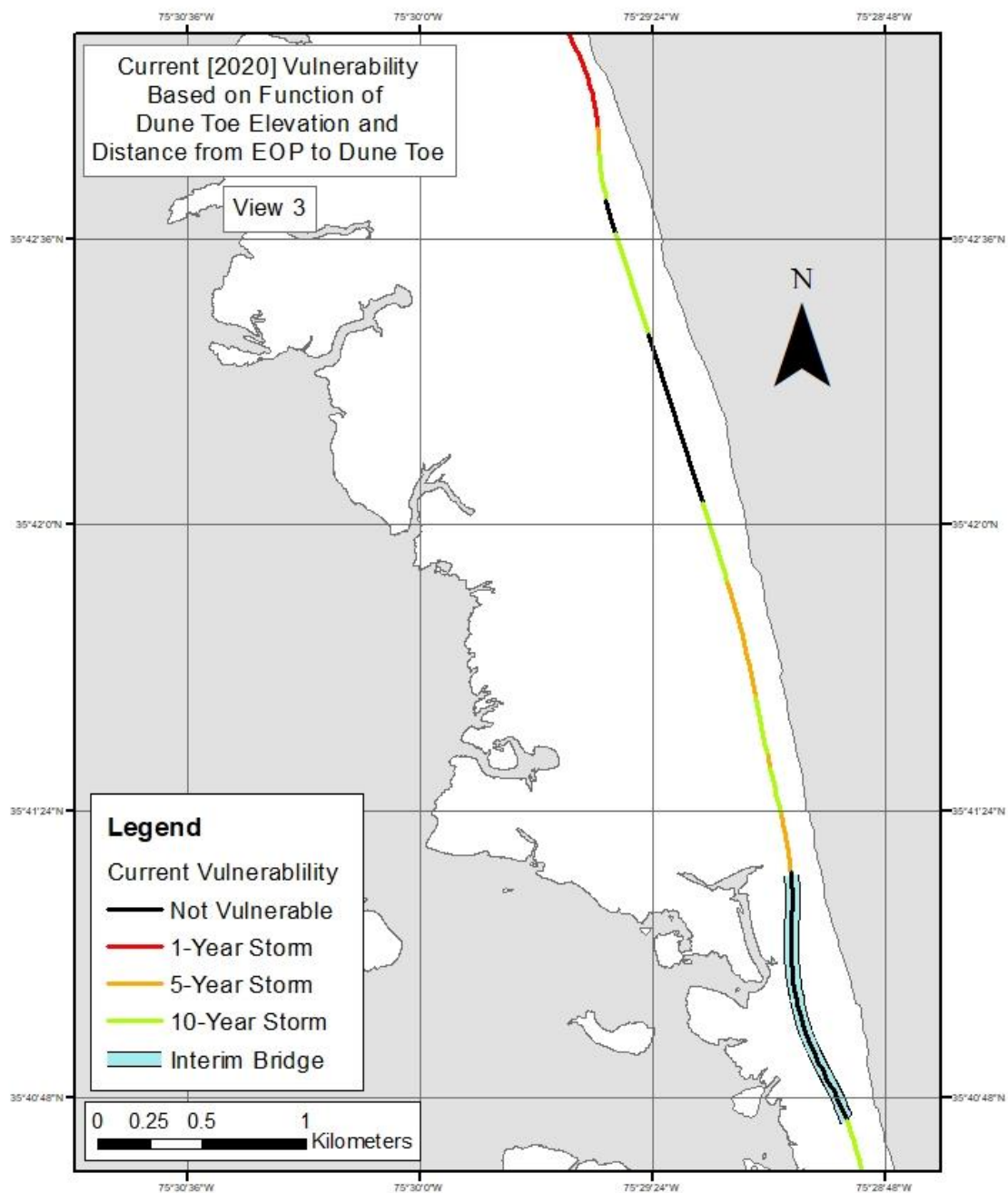


Figure A.3 Map of parts of NC 12 that were predicted vulnerable to storm impacts. Assessment was performed on the present (August 2020) state of the road and topography using a weighted linear function of EOP to Dune Toe and Dune Toe Elevation. View 3 of 6.

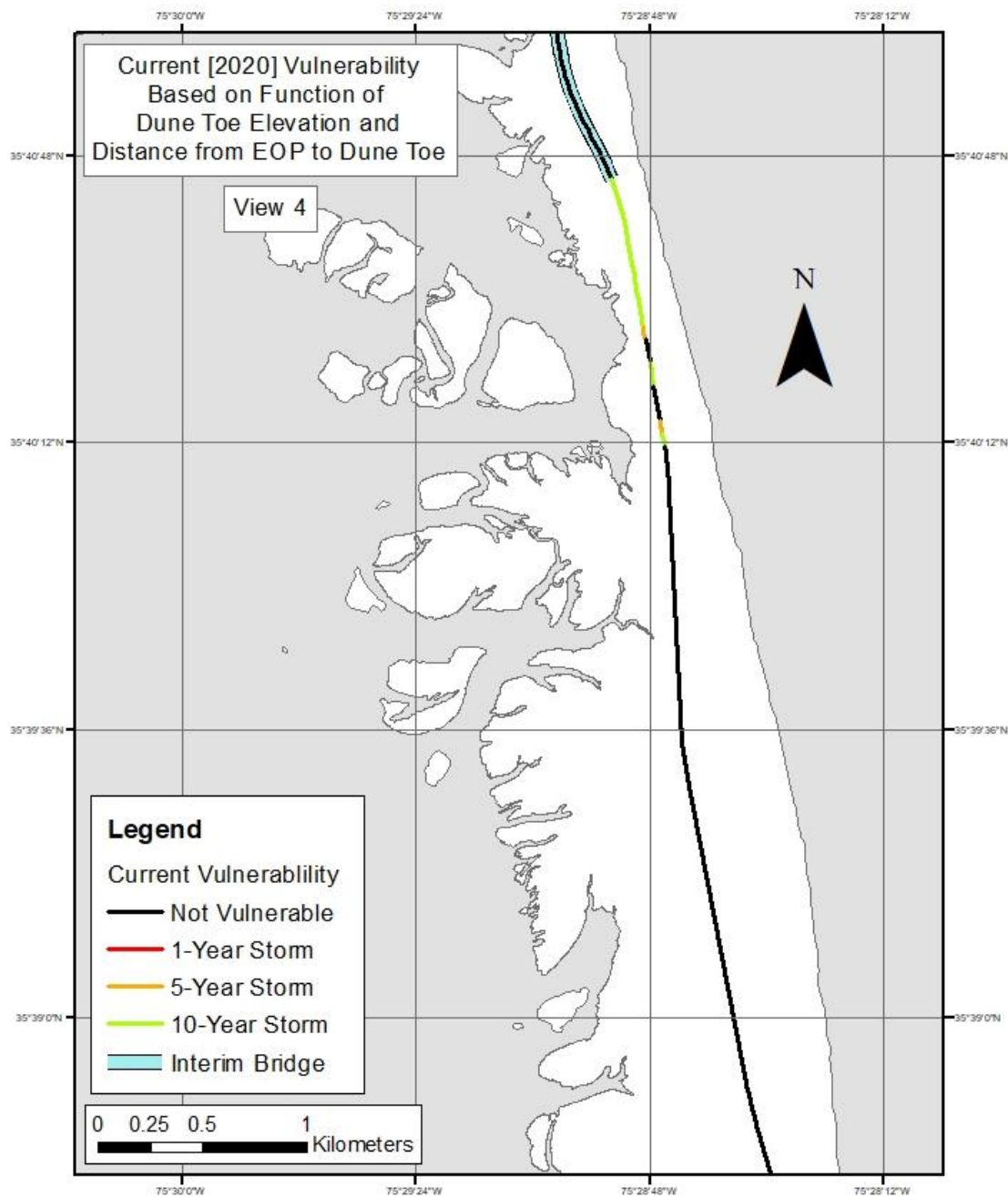


Figure A.4 Map of parts of NC 12 that were predicted vulnerable to storm impacts. Assessment was performed on the present (August 2020) state of the road and topography using a weighted linear function of EOP to Dune Toe and Dune Toe Elevation. View 4 of 6.

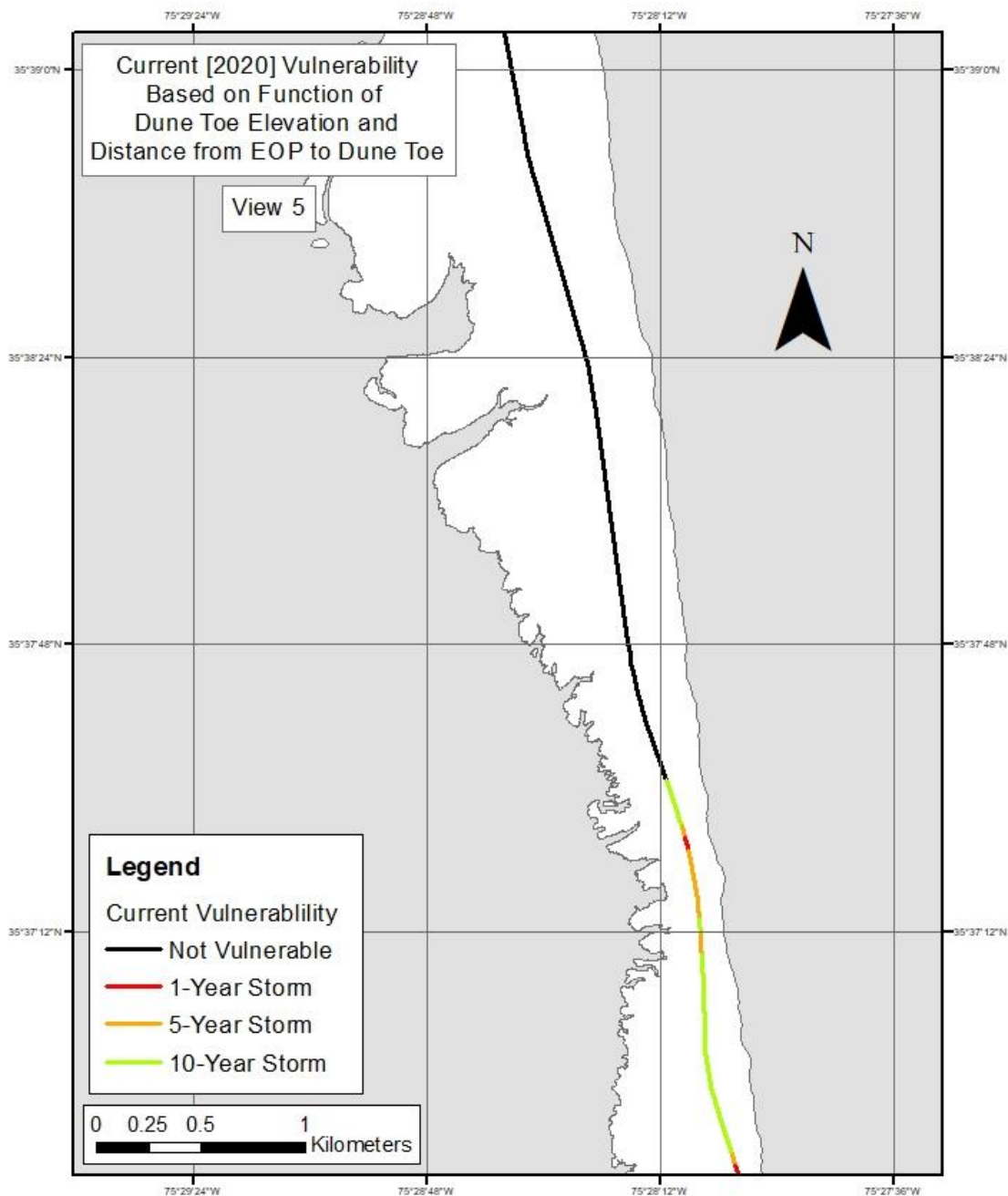


Figure A.5 Map of parts of NC 12 that were predicted vulnerable to storm impacts. Assessment was performed on the present (August 2020) state of the road and topography using a weighted linear function of EOP to Dune Toe and Dune Toe Elevation. View 5 of 6.

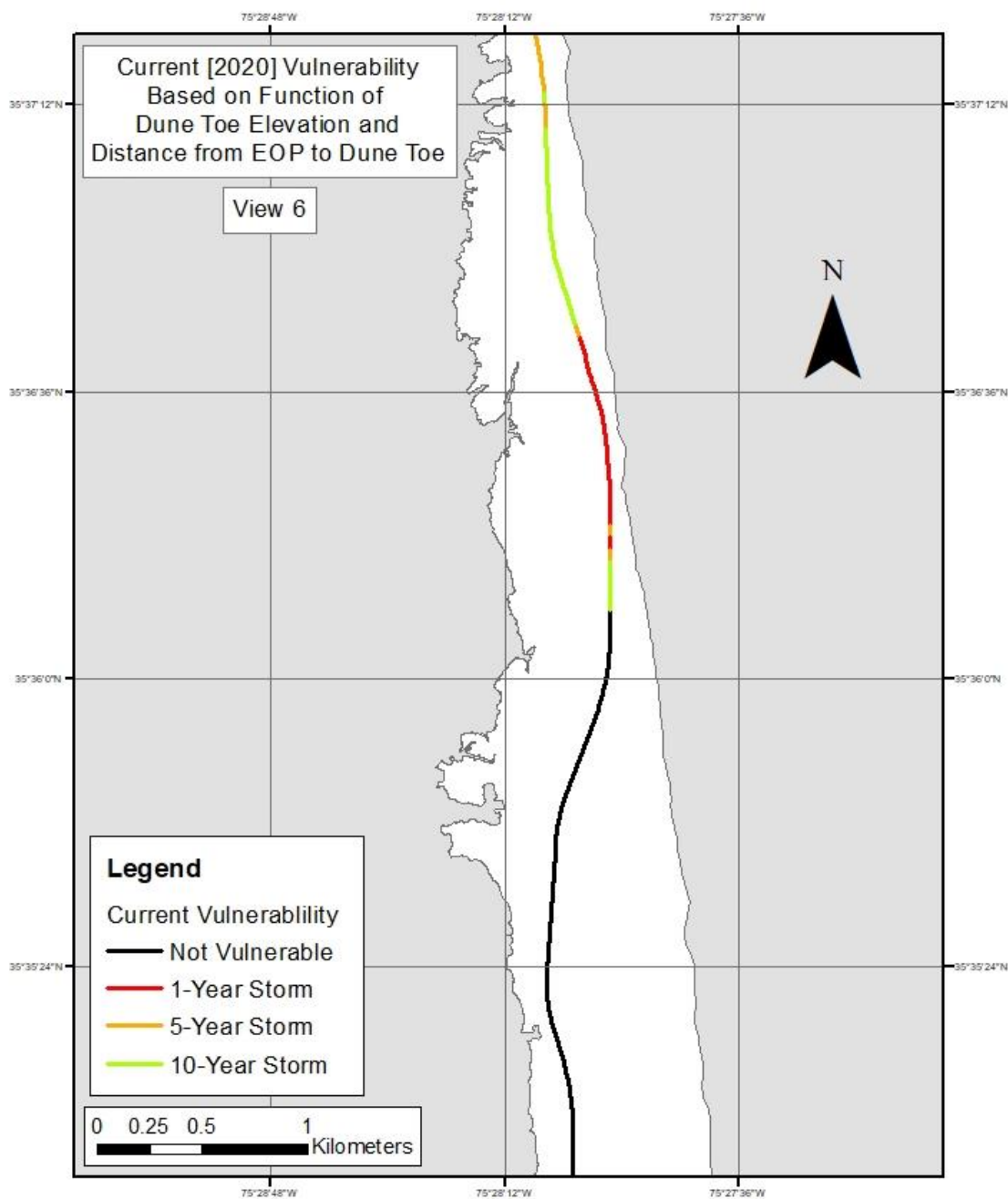


Figure A.6 Map of parts of NC 12 that were predicted vulnerable to storm impacts. Assessment was performed on the present (August 2020) state of the road and topography using a weighted linear function of EOP to Dune Toe and Dune Toe Elevation. View 6 of 6.

Appendix B: Future (10 year projection / 2030) Vulnerability Assessment

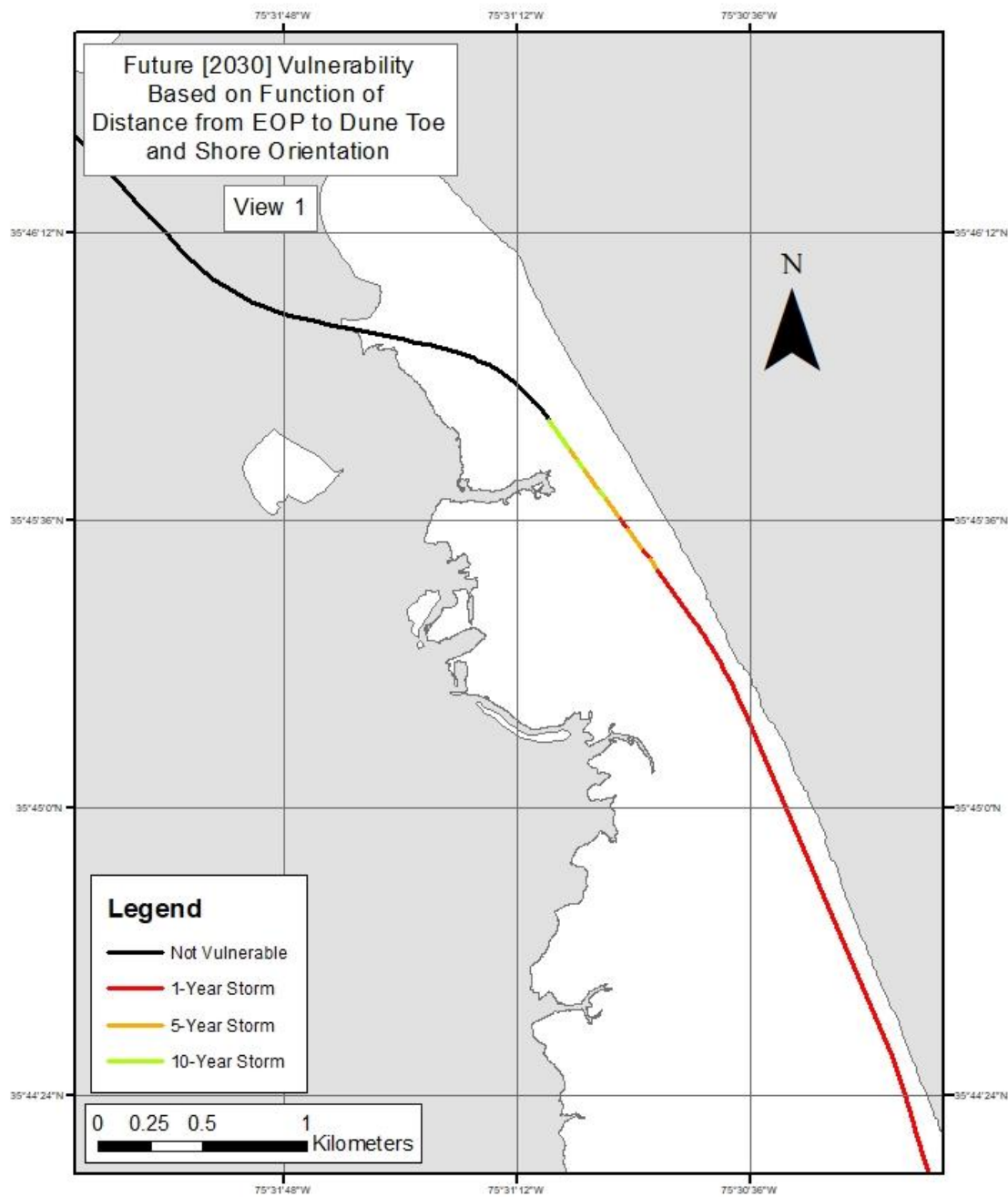


Figure B.1 Map of parts of NC 12 that were predicted vulnerable to storm impacts. Assessment was performed on the predicted future (10-year projection / August 2030) state of the road and topography using a weighted linear function of EOP to Dune Toe and Shore Orientation.

View 1 of 6.

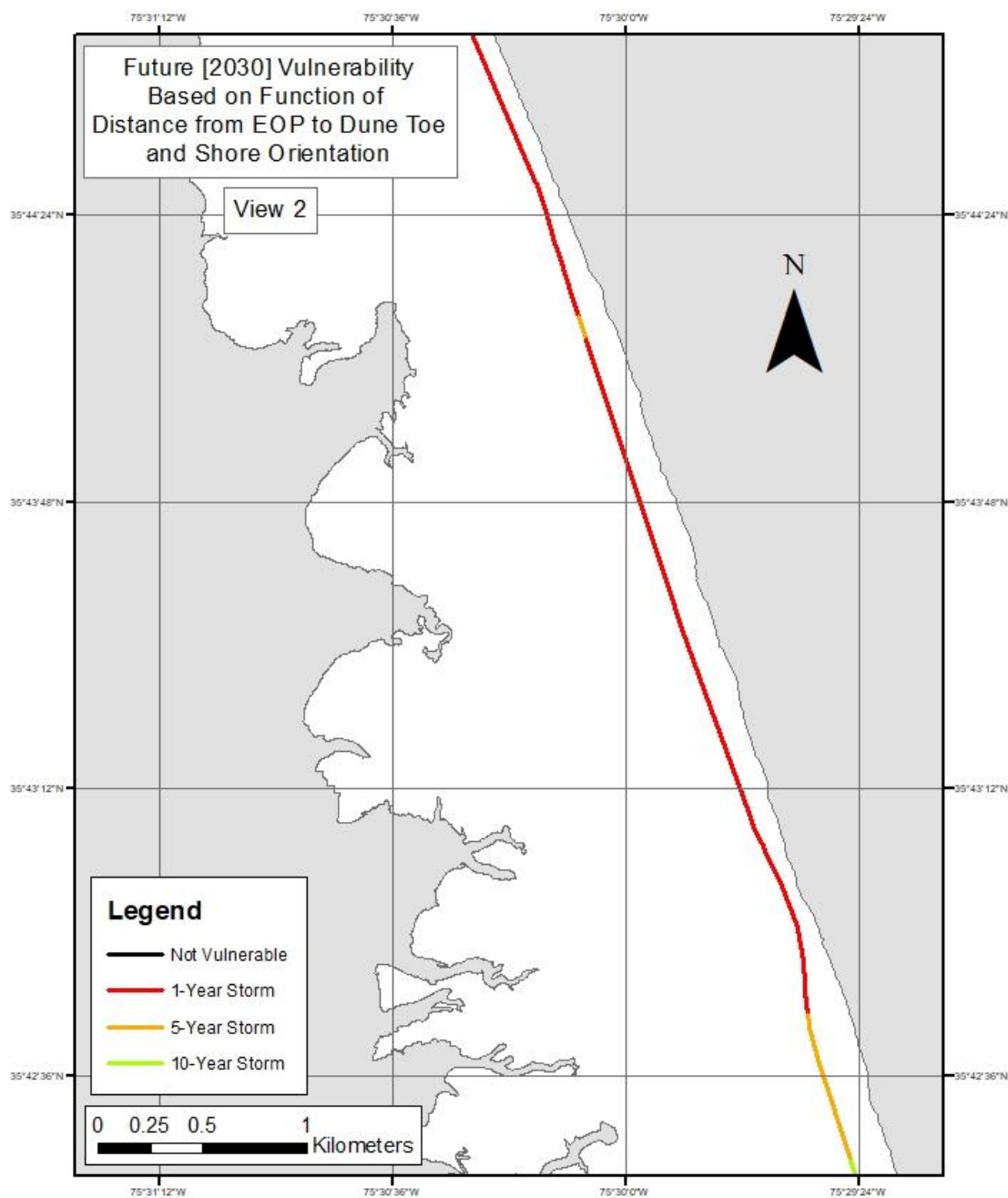


Figure B.2 Map of parts of NC 12 that were predicted vulnerable to storm impacts. Assessment was performed on the predicted future (10-year projection / August 2030) state of the road and topography using a weighted linear function of EOP to Dune Toe and Shore Orientation.

View 2 of 6.

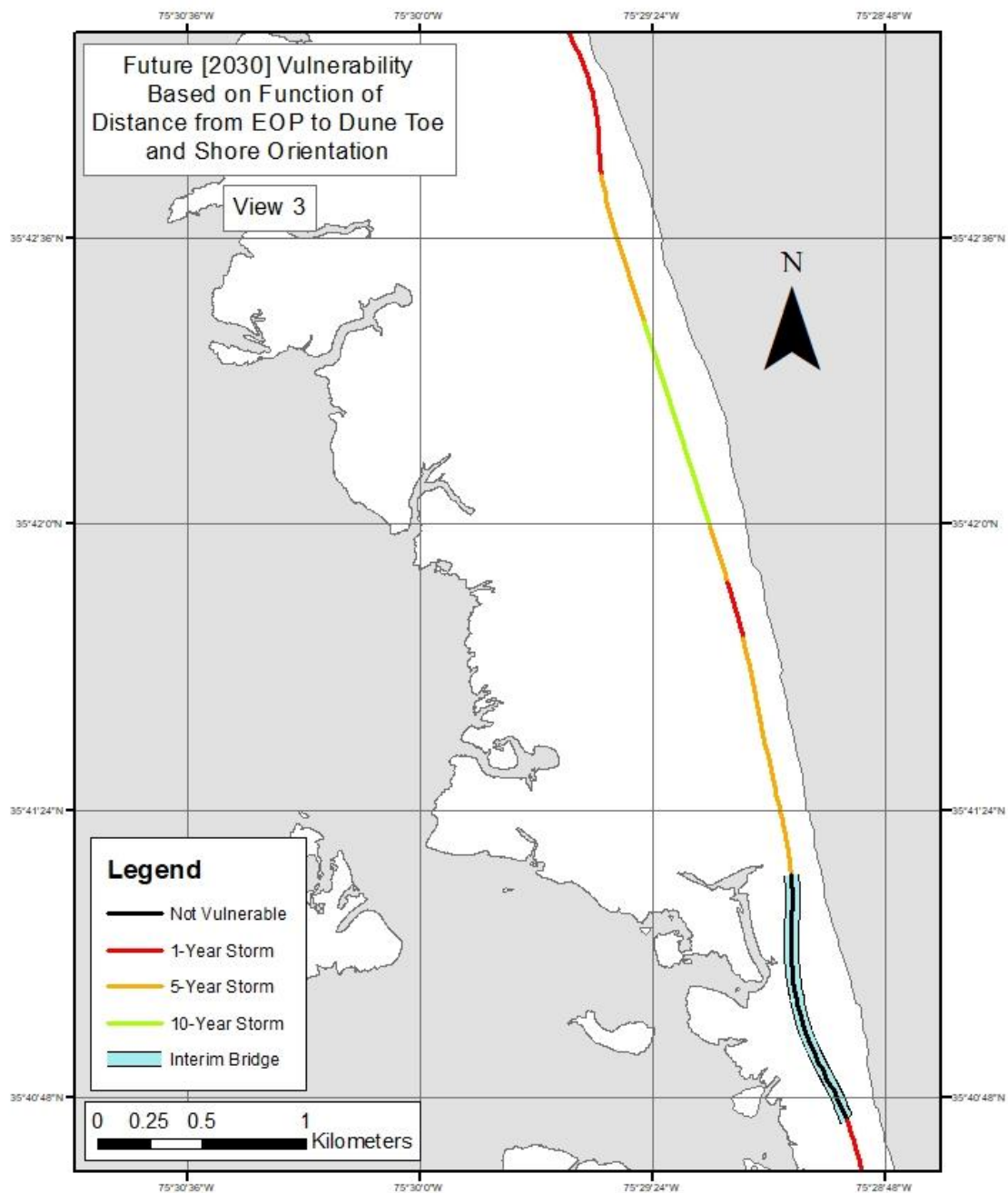


Figure B.3 Map of parts of NC 12 that were predicted vulnerable to storm impacts. Assessment was performed on the predicted future (10-year projection / August 2030) state of the road and topography using a weighted linear function of EOP to Dune Toe and Shore Orientation.

View 3 of 6.

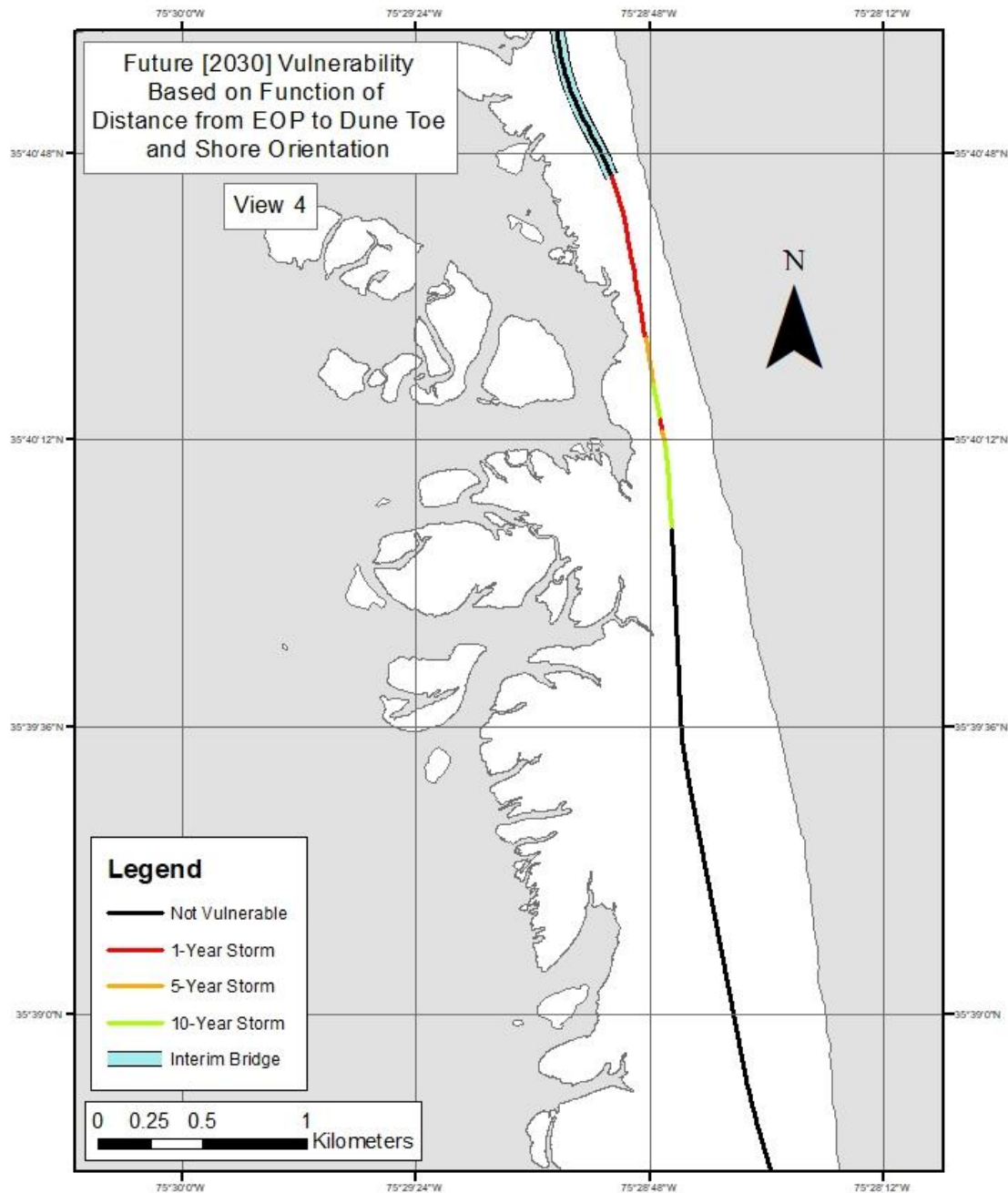


Figure B.4 Map of parts of NC 12 that were predicted vulnerable to storm impacts. Assessment was performed on the predicted future (10-year projection / August 2030) state of the road and topography using a weighted linear function of EOP to Dune Toe and Shore Orientation.

View 4 of 6.

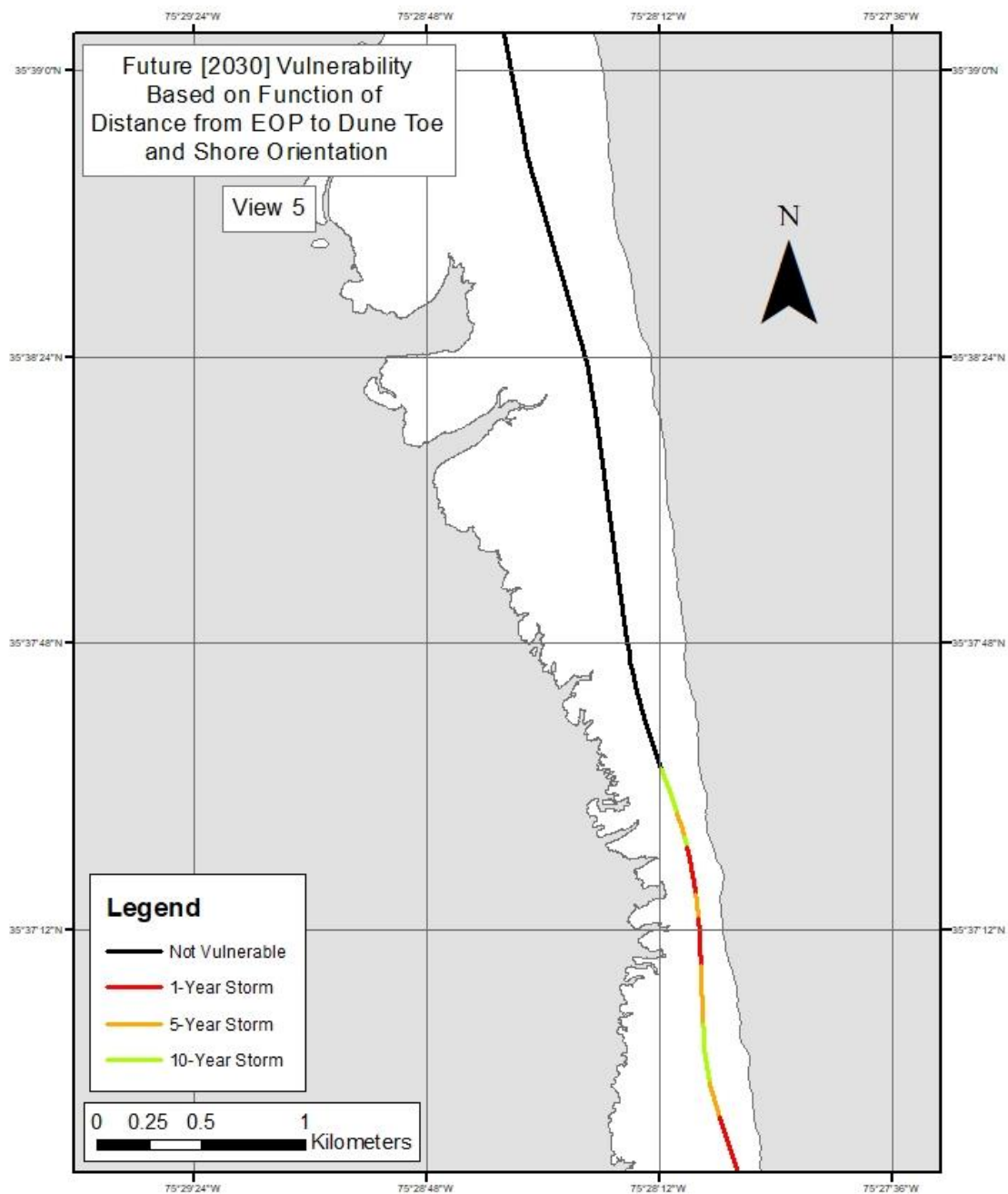


Figure B.5 Map of parts of NC 12 that were predicted vulnerable to storm impacts. Assessment was performed on the predicted future (10-year projection / August 2030) state of the road and topography using a weighted linear function of EOP to Dune Toe and Shore Orientation.

View 5 of 6.

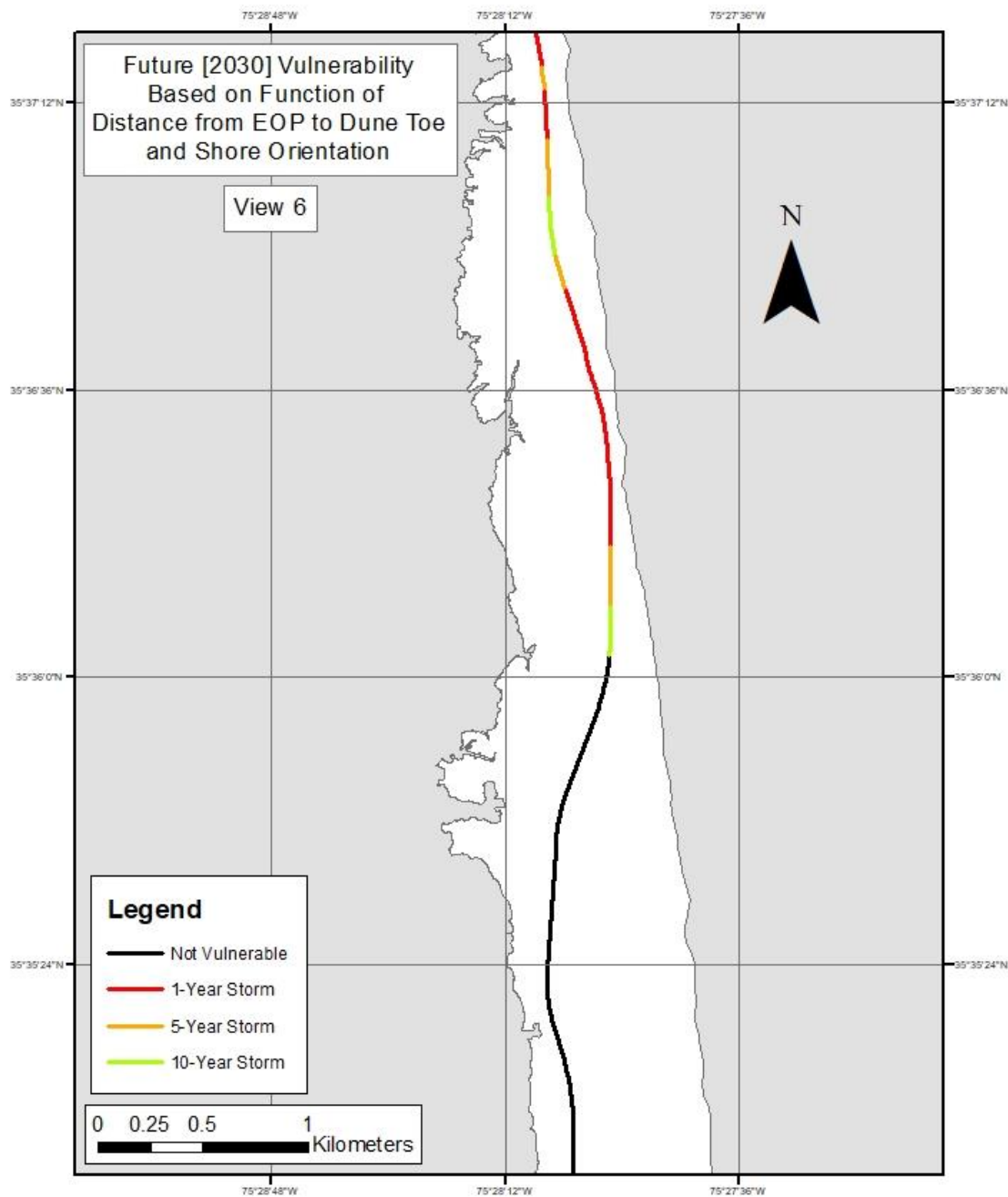


Figure B.6 Map of parts of NC 12 that were predicted vulnerable to storm impacts. Assessment was performed on the predicted future (10-year projection / August 2030) state of the road and topography using a weighted linear function of EOP to Dune Toe and Shore Orientation.

View 6 of 6.

Appendix C: Descriptive Statistical Analysis of Indicator Values

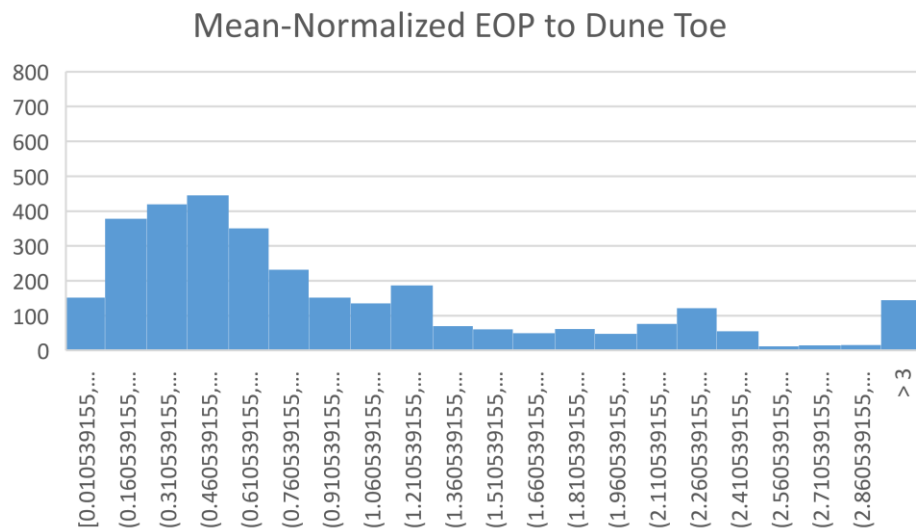


Figure C.1 Histogram of the EOP to Dune Toe indicator's values normalized by their mean to show the distribution of data.

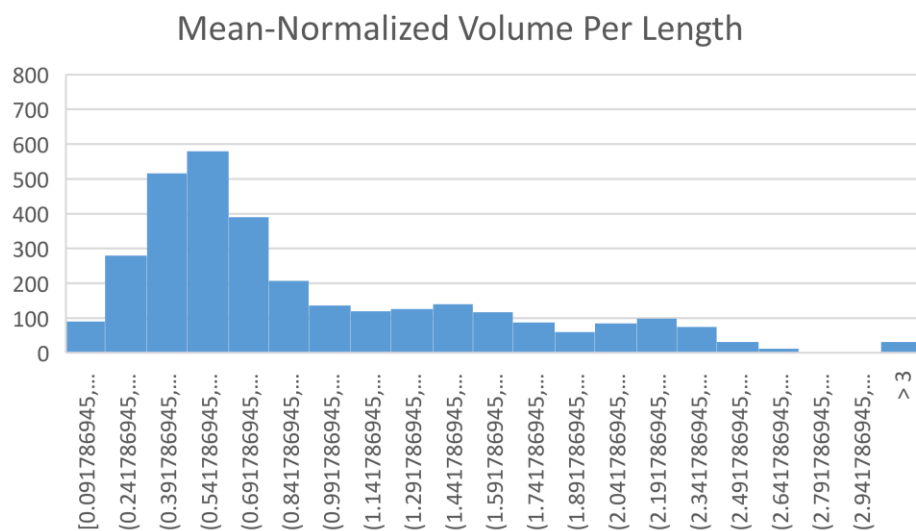


Figure C.2 Histogram of the Volume Per Length indicator's values normalized by their mean to show the distribution of data.

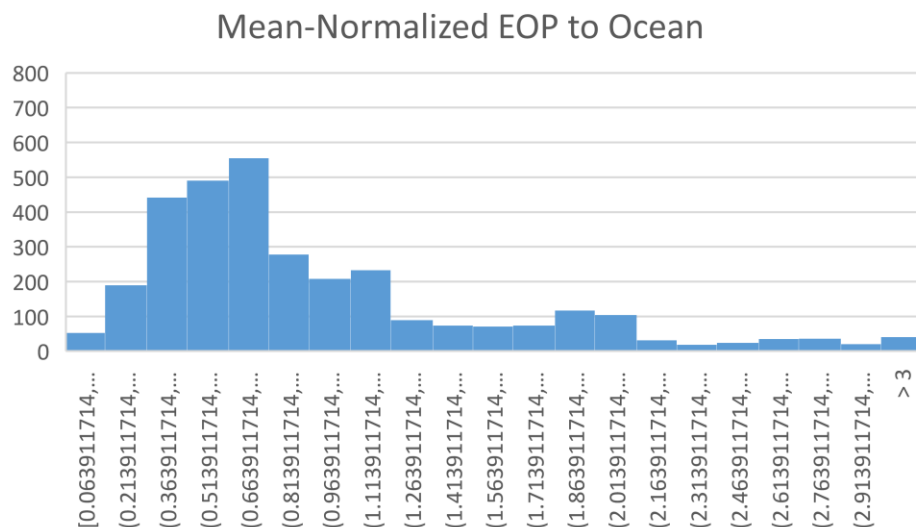


Figure C.3 Histogram of the EOP to Ocean Shore indicator's values normalized by their mean to show the distribution of data.

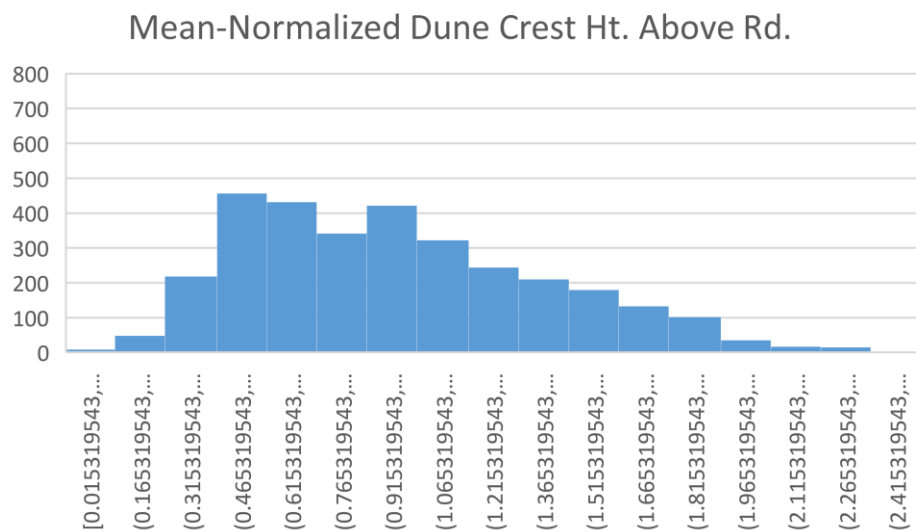


Figure C.4 Histogram of the Dune Crest Height Above the Road indicator's values normalized by their mean to show the distribution of data.

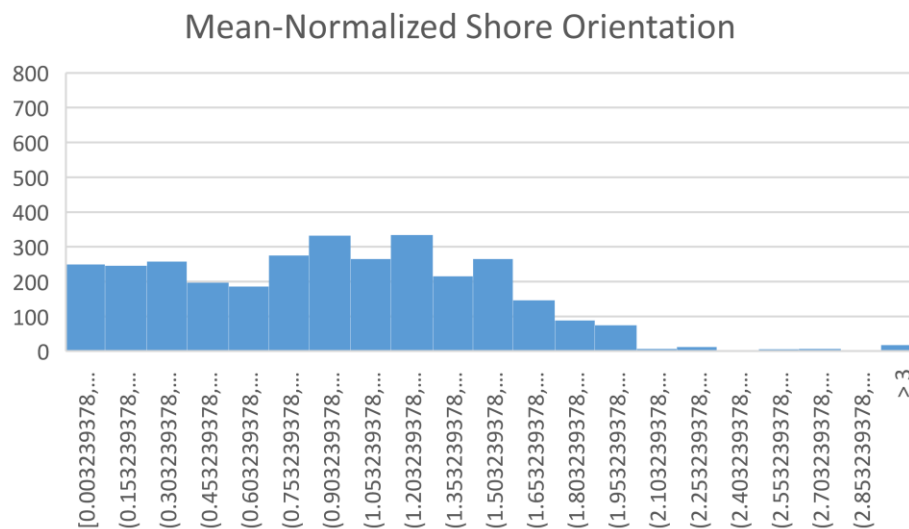


Figure C.5 Histogram of the Shore Orientation indicator's values normalized by their mean to show the distribution of data.

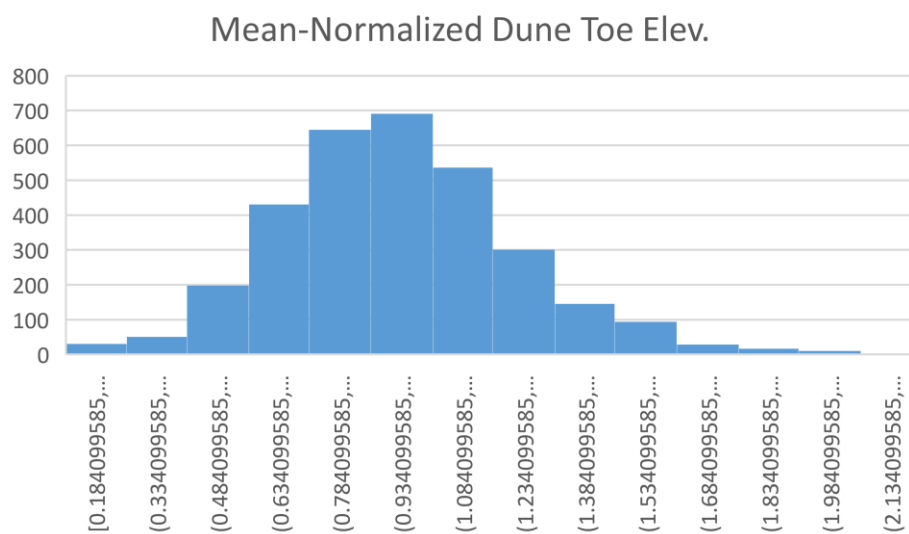


Figure C.6 Histogram of the Dune Toe Elevation indicator's values normalized by their mean to show the distribution of data.

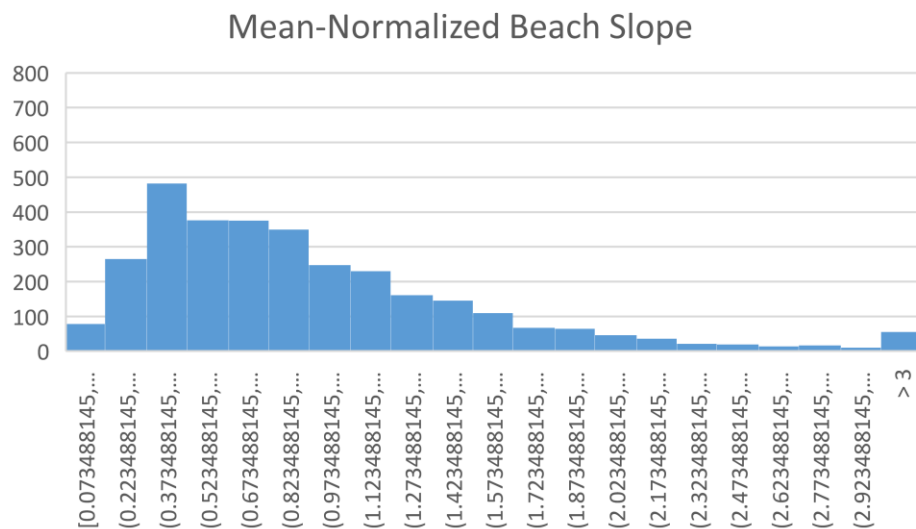


Figure C.7 Histogram of the Beach Slope indicator's values normalized by their mean to show the distribution of data.

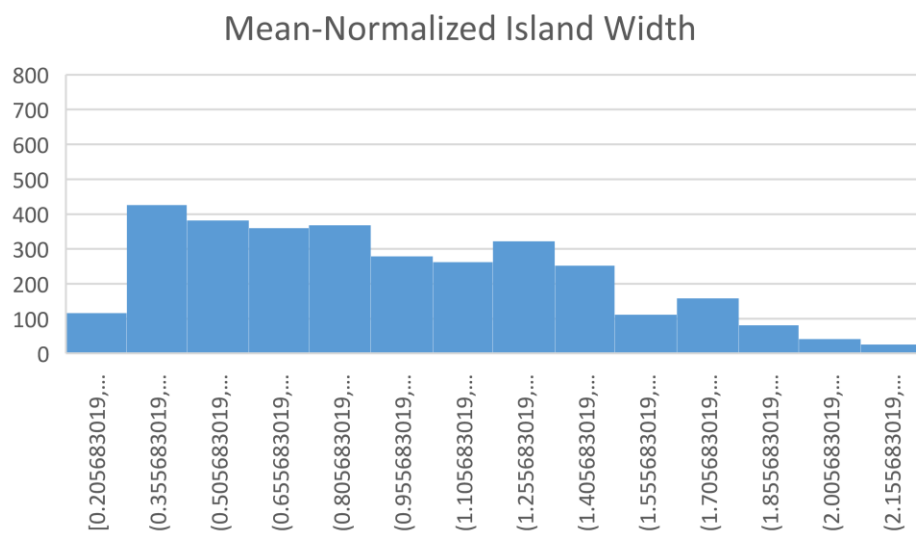


Figure C.8 Histogram of the Island Width indicator's values normalized by their mean to show the distribution of data.

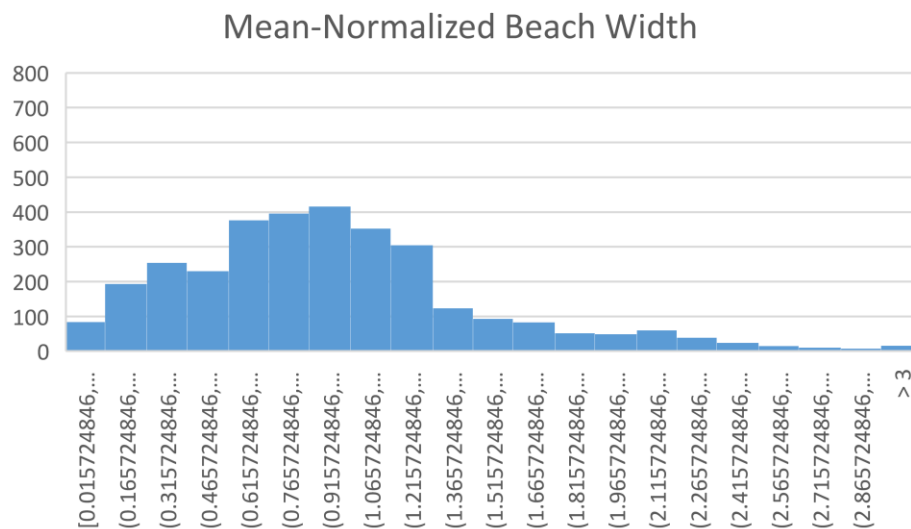


Figure C.9 Histogram of the Beach Width indicator’s values normalized by their mean to show the distribution of data.

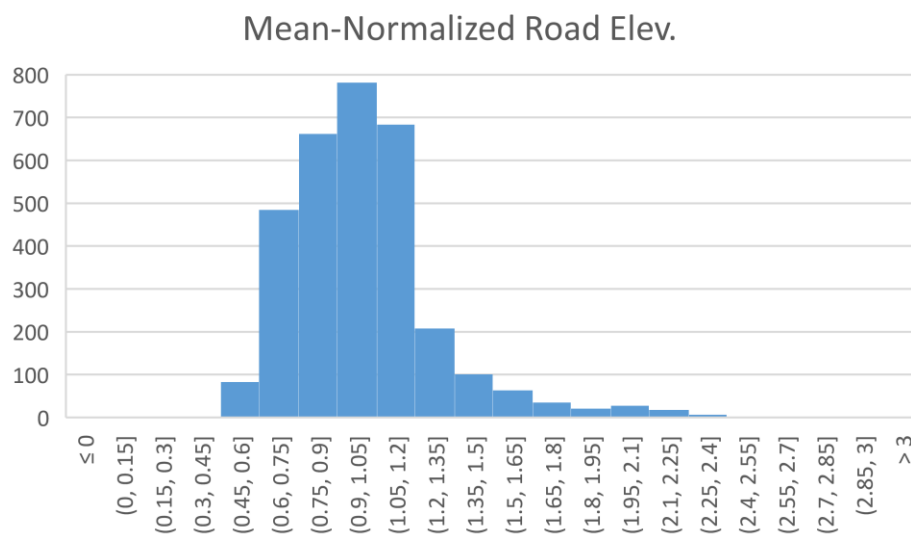


Figure C.10 Histogram of the Road Elevation indicator’s values normalized by their mean to show the distribution of data.

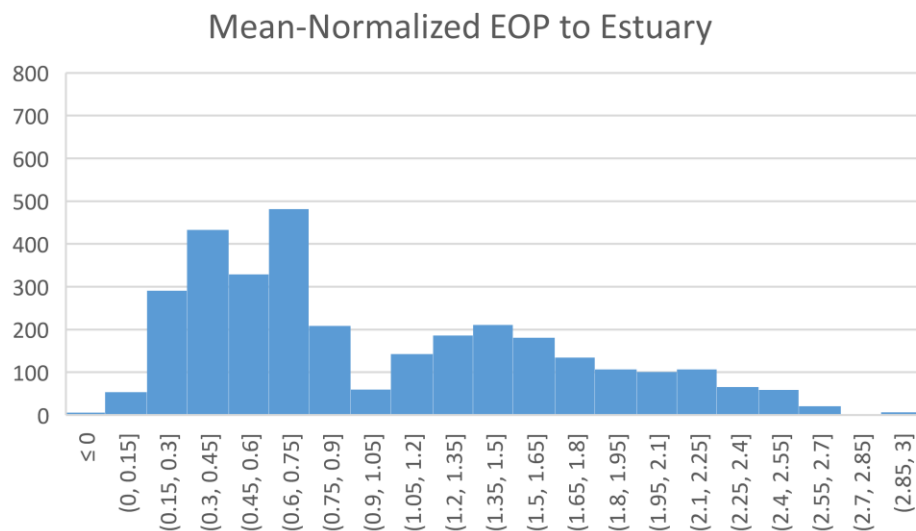


Figure C.11 Histogram of the EOP to Estuary Shore indicator's values normalized by their mean to show the distribution of data.